Numerical Study of Wind Turbine Wakes of Asymmetric Rotor

P. C. Yen

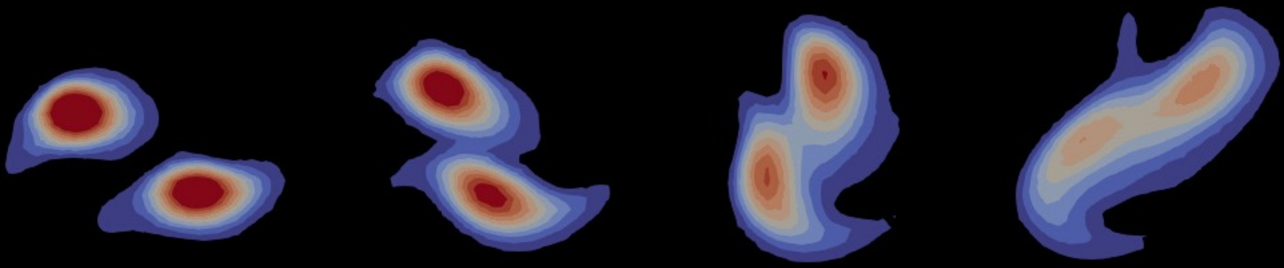

TUDelft

Numerical Study of Wind Turbine Wakes of Asymmetric Rotor

by

P. C. Yen

in fulfillment of the requirements for the degree of

Master of Science in Aerospace Engineering

at the Delft University of Technology

Student number:	5694256		
Project duration:	January 11, 2024 – September 17, 2024		
Defense date:	September 17, 2024 13:30, Delft		
Thesis committee:	Chair	Dr. D. Ragni	TU Delft (LR)
	Examiner	Dr. ir. T. Sinnige	TU Delft (LR)
	Supervisor	Dr. W. Yu	TU Delft (LR)
	Supervisor	Prof. dr. F. Scarano	TU Delft (LR)

An electronic version of this thesis is available at http://repository.tudelft.nl/.

Preface

This thesis marks an end to my master's studies in wind energy aerodynamics at Delft University of Technology. These past two years have been more fruitful than I could have ever imagined. From lectures to internship, and finally, to this thesis work, the journey has been filled with moments of joy and breakdown (as tip vortices). I am deeply grateful for the support and encouragement of the people surrounding me.

I would like to express my gratitude to Prof. Fulvio Scarano and Dr. Wei Yu. Your dedication and insightful guidance have been a constant source of motivation for me to dive deeper into my research. The many inspiring moments during our weekly meetings, or even during a quick drop-by, have truly opened doors for me in this field. I would also like to give thanks to Clem for the technical support and engaging discussions. Your contributions have been very helpful in this work.

To the HSL basement crew—Aurora, Georgia, Haozhe, Marco, Teddy, and Yuxuan—The countless times we have asked each other, "How is your thesis going?" has always been more sarcasm than a true question. Many out-of-the-box discussions with you have been both inspiring and invaluable, and it is because of you that I never felt alone.

To the DB squad, thank you for introducing such a fun sport to me. Climbing with you all has become the most exciting and distressing weekly event during thesis work. A special thanks to Ege and Peng —your invitations during my lowest moments meant more to me than words can express. Also thanks to Charlotte and Yu-Fan for all the spottings.

And to my loved ones. 我的家人以及可耘，謝謝你們無條件支持我追求熱情。

Finally, to myself from two years ago. You will struggle with coursework, you will feel anxious about the next steps, and there may be moments when you feel completely overwhelmed. But this journey will be worth it, as long as you give all you have got.

Delft, September 2024

Summary

Wind turbine wakes are known for their detrimental effects, such as lower wind speed and higher turbulence intensity than the freestream condition. These factors lead to energy loss and fatigue loads on downstream turbines. Bounding the wake, tip vortex helices were found to block the kinetic energy entrainment into the wake from previous work. To deal with this issue, the scientific community has been exploring methods to perturb this helical vortex system, aiming to accelerate wake recovery.

This study numerically explores a passive method to perturb the tip vortex system by introducing rotor asymmetry through blade length difference. By imposing a radial offset between tip vortices, the well-known leapfrogging instability is triggered, which is expected to enhance turbulent mixing at the wake boundary. Large eddy simulation and the actuator line model are applied to a modified NREL 5MW wind turbine across 16 test cases. These cases cover blade length differences of 2.5% to 30% of the rotor radius under different inflow conditions, including laminar, laboratory level, and atmospheric boundary layer level of turbulent intensity. In parallel with this work, a wind tunnel experiment with a different Reynolds number was conducted in the W-tunnel at TU Delft (Mascioli, 2024). Besides, a novel approach based on a simple 2D vortex model is developed to quantify the growth rate of leapfrogging instability.

The numerical results reveal a relationship between the degree of rotor asymmetry and the triggered leapfrogging instability. In specific, as the blade length difference increases, the leapfrogging occurs closer to the upstream, but with a lower instability growth rate. This phenomenon is mainly attributed to two main factors – differences in convection and vortex induction. Besides, the normalized leapfrogging time aligns well with the experimental data, further validating the proposed relevant length and time scale from previous work. However, despite these perturbations, the tip vortex system does not break down solely by rotor asymmetry. Instead, these vortex pairs merge after the first leapfrogging event and formulate a new stable array.

Furthermore, the wake recovery analysis, based on the velocity profiles and mean-flow kinetic energy flux, reveals that the wake recovery is dominated by the inflow turbulence intensity rather than rotor asymmetry. Local tip vortex behaviors have a limited impact on the overall wake characteristics while increasing turbulence intensity significantly accelerates wake recovery. Specifically, under laminar inflow conditions, rotor asymmetry does not contribute to an increased rate of disk-averaged velocity. At an inflow turbulence intensity of 0.5% (laboratory level), rotor asymmetry delays the turbulence mixing process. Under a turbulence intensity of 5% (atmospheric boundary layer level), the impact of rotor asymmetry is mitigated in terms of disk-averaged velocity.

Key words: rotor asymmetry, HAWT, wind turbine, large eddy simulation, actuator line model, leapfrogging instability, helical instability, wake recovery

Contents

List of Figures

List of Tables

Nomenclature

Abbreviations

Abbreviation	Definition
ADM-NR	Actuator disk model - Non rotational
ADM-R	Actuator disk model - Rotational
ALM	Actuator line model
BEM	Blade element momentum theory
CDS	Central differencing scheme
CFD	Computational fluid dynamics
CFL	Courant–Friedrichs–Lewy
CSF	Cumulative sum of mean-flow kinetic-energy flux
DES	Detached Eddy Simulation
DFSEM	Divergence free synthetic eddy method
DNS	Direct Numerical Simulation
DU	Delft University
LES	Large Eddies Simulation
HAWT	Horizontal axis wind turbine
HIT	Homogeneous isotropic turbulence
NACA	National Advisory Committee for Aeronautics
NREL	National Renewable Energy Laboratory
RANS	Reynolds-averaged Navier–Stokes
SGS	Subgrid-scale
URANS	Unsteady Reynolds-averaged Navier–Stokes
UDS	Upwind differencing scheme
TI	Turbulence intensity
TKE	Turbulent kinetic energy
TSR	Tip speed ratio

Symbols

Symbol	Definition	Unit
A_0	Original frontal area	[m^2]
A_e	Effective frontal area	[m^2]
$A_{\Delta r}$	Truncated frontal area	[m^2]
C_D	Drag coefficient	[-]
C_L	Lift coefficient	[-]
C_P	Power coefficient	[-]

Symbol	Definition	Unit
C_T	Thrust coefficient	[-]
C_k	TKE model constant 1	[-]
C_n	Axial force coefficient	[-]
C_s	Smagorinsky constant	[-]
C_t	Azimuthal force coefficient	[-]
C_ϵ	TKE scale model constant 2	[-]
D	Drag force	[N]
D_0	Original rotor diameter	[m]
D_e	Effective rotor diameter	[m]
F	Force	[N]
F_1	Shen's correction factor	[-]
L	Lift force	[N]
N_b	Number of blades	[-]
N_p	Number of inducing vortices	[-]
N_{probes}	Number of probes	[-]
R_0	Original rotor radius	[m]
$R_{\Delta r}$	Truncated blade length	[m]
Re_D	Diameter based Reynolds number	[-]
Re_Γ	Circulation-based Reynolds number	[-]
S_{ij}	Strain rate tensor	[1/s]
T_{avg}	Averaging period	[s]
U_∞	Free stream velocity	[m/s]
U_a	Apparent wind speed	[m/s]
a	Axial induction factor	[-]
a_v	Vortex core radius	[-]
a'	Tangential induction factor	[-]
b	Vortex separation distance	[m]
c	Chord length	[m]
f	Rotor frequency	[1/s]
f_{2D}	Sectional force	[N/m]
h	Tip vortex streamwise separation distance	[m]
h'	Helical pitch	[m]
k_{res}	Resolved TKE	[m^2/s^2]
k_{sgs}	Sub-grid scale TKE	[m^2/s^2]
n	Axial direction	[-]
r	Radial position	[m]
s_1	Shen's coefficient 1	[-]
s_2	Shen's coefficient 2	[-]
t_{LF}	Leapfrogging time	[s]
u_c	Convective velocity	[-]
$< \overline{u} >_{\mathrm{disk}}$	Disk-averaged velocity	[m/s]
x_{LF}	Leapfrogging distance	[m]
x_n	Near wake length	[m]
Δ	Grid size	[m]

Symbol	Definition	Unit
Δ_b	Actuator line element size	[m]
Δr	Blade length difference	[m]
Δt	Time step	[s]
Δx_{tip}	Blade tip displacement	[m]
Γ	Circulation of vortex	[m^2/s]
Γ_{Merg}	Circulation of merged vortex	[m^2/s]
Ω	Rotational frequency	[rad/s]
Φ	Inflow angle	[deg]
δ_{ij}	Kronecker delta	[-]
δh	Vortex separation distance - streamwise projection	[m]
δr	Vortex separation distance - radial projection	[m]
ϵ	ALM Smoothing parameter	[m]
η	Kolmogorov length scale	[-]
η_ϵ	ALM regularization kernel	[1/m^2]
γ	Local pitch angle	[deg]
λ	Tip speed ratio	[-]
ρ	Density	[kg/m^3]
σ_{2D}	Leapfrogging instability growth rate from 2D model	[1/s]
σ_{LES}	Leapfrogging instability growth rate from LES-ALM	[1/s]
ν	Kinematic viscosity	[m^2/s]
ω	Vorticity	[1/s]
ϕ_{ij}	Mean flow kinetic energy flux	[m^3/s^3]
τ	Torque	[Nm]
τ_{ij}	Stress tensor	[N/m^2]
θ	Azimuthal direction	[-]

1

Introduction

A cluster of wind turbines, commonly referred to as a wind farm, encounters a challenge due to the phenomenon known as *wake effect*. When wind turbines extract energy from the wind, they create downstream wakes characterized by reduced kinetic energy and increased turbulence. These wakes affect wind farms by lowering overall energy production and placing additional fatigue loads on downstream turbines (Lundquist et al., 2008). The distance necessary for complete wake recovery often extends several turbine diameters depending on the flow conditions. During this recovery, the slower air in the wake mixes with surrounding flows, gradually replenishing kinetic energy (Burton et al., 2021). From such analysis, the conclusion arises that accelerating wake recovery could shorten the spacing between turbines. This would lead to more efficient spatial utilization within wind farms, potentially allowing for more turbines to be installed in a given space.

The wake structure behind a horizontal axis wind turbine (HAWT) can be generally divided into two distinct parts. The *near-wake* region is primarily influenced by the presence of the rotor, such as axial and radial pressure gradient (Ainslie, 1988; Okulov et al., 2014; Vermeer et al., 2003). As illustrated in Figure 1.1, this region features the periodic helical vortex system, formed by tip and root vortices. The genesis of these tip and root vortices is attributed to the gradient in bound circulation along the blade span, which then concentrates at the blade's tip and root (Ivanell, 2005). In contrast, the *far-wake* typically refers to the downstream region where the development of the streamwise velocity profile exhibits a Gaussian-like shape, resulting from the spreading of the wake (Stevens and Meneveau, 2017). Flow in this region is dominated by diffusion rather than turbine characteristics (J. Sørensen et al., 2015). The transitional area between the near- and far-wake regions, labeled as the *Intermediate wake* in Figure 1.2, is triggered by vortex helix instabilities and results in the breakdown of tip vortices into smaller eddies.

Vortex helical instabilities play a crucial role in the breakdown of the tip vortices. One of the instabilities (see Subsection 1.1.1) is referred to as *Leapfrogging* due to its resemblance to the leaping motion of frogs. This phenomenon acts as an onset of the mixing process since the near-wake tip vortex serves as a shield of the wake region, causing a

Figure 1.1: Flow visualization of a wind turbine wake helix, taken from Hand et al. (2001)

delay in the turbulence mixing process, as pointed out by Medici (2005). Similar outcomes were observed in a wind tunnel experiment conducted by Lignarolo et al. (2015). They discovered that in the near-wake region, fluxes of kinetic energy are dominated by periodic fluctuation, where the transport occurs both into and out of the wake at similar rates. Up until the leapfrogging area, the net entrainment of kinetic energy by random turbulence is not significantly increased. This suggests that moving the leapfrogging process upstream could potentially accelerate the wake recovery process.

In this chapter, the research context is introduced. Section 1.1 discusses the physical background of leapfrogging instability and the state-of-the-art methods used to trigger this phenomenon. Subsection 1.2.1 reviews current numerical methods in wind turbine/wind farm aerodynamics calculations, explaining the rationale behind the selected methodology. Lastly, Section 1.3 and Section 1.4 outline the scope of this research and provide an overview of the thesis structure.

1.1. Leapfrogging instability

Instabilities lead to the breakdown of tip vortex helices, with leapfrogging instability being the most dominant mode. This section will first briefly introduce the physical background of this phenomenon in Subsection 1.1.1. Subsequently, Subsection 1.1.2 will review previous approaches used to intentionally trigger such instability.

1.1.1. Instability of a vortex helix

The instability of a helical vortex system is commonly categorized into three types. In the study by Widnall (1972), a detailed exploration of the inviscid instabilities was undertaken. These instabilities encompass short-wave, long-wave, and mutual inductance modes, which have been proven by Walther et al. (2007) using direct numerical simulation in a viscous setting. The short-wave instability can be understood as the external strain field induced by neighboring vortices, leading to modifications in the vortex core

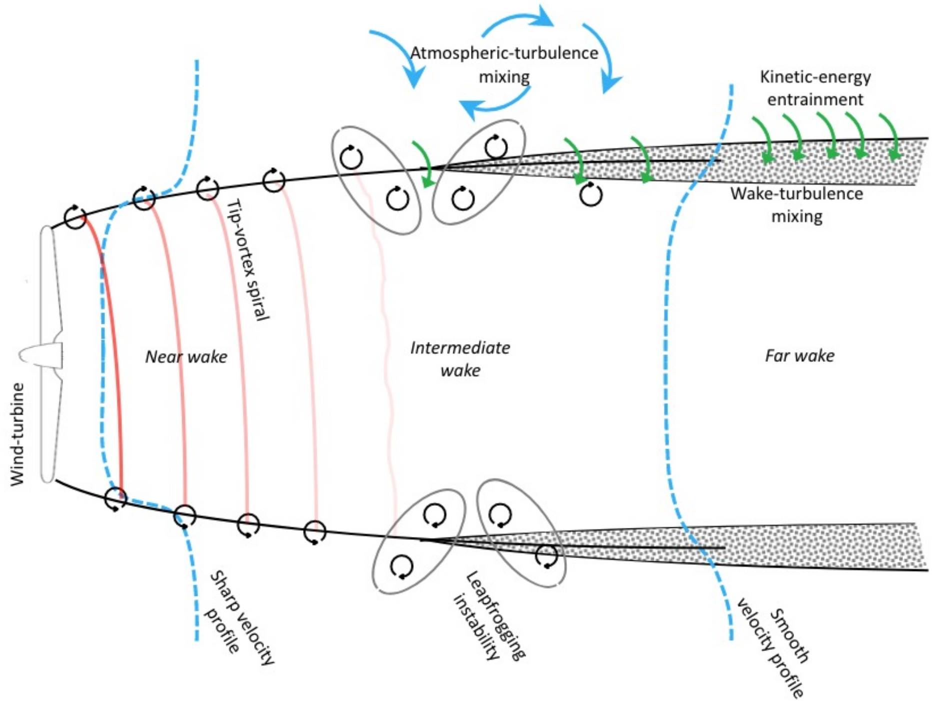

Figure 1.2: Diagram of wind turbine wake with leapfrogging instability, taken from Lignarolo (2016)

structure. Secondly, the long-wave instability involves perturbations that displace the vortices as a whole without altering the core structure. The most unstable displacement of this instability arises from the out-of-phase between adjacent helices, leading to the classic two-dimensional instability: mutual inductance/leapfrogging (Quaranta et al., 2015). This zero-wavenumber instability is characterized by the rolling around motion in the adjacent tip vortices pair, a phenomenon observed and confirmed in the context of rotor wake by Felli et al. (2011). Furthermore, it has been identified as the most dominant mode leading to wake destabilization (Ivanell et al., 2010; Sarmast et al., 2014; J. N. Sørensen, 2011a).

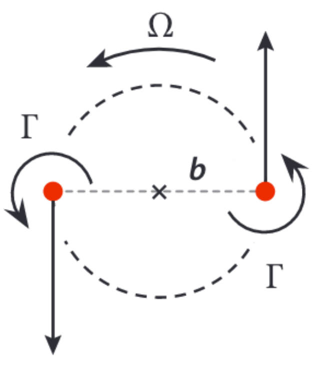

Figure 1.3: Trajectories of two-dimensional co-rotating point vortex pairs, with separation distance b and circulation Γ, taken from Leweke et al. (2016)

The leapfrogging phenomenon can be seen as a two-dimensional vortex merging process. Recent research has focused on this merging process between co-rotating vortex pairs

(See the review by Leweke et al. (2016)). In the absence of diffusivity (or viscosity), a co-rotating vortex pair rotates indefinitely, as described by the Biot-Savart law (see Figure 1.3). However, with the introduction of viscosity, the process progresses to the next stage—vortex merging. Melander et al. (1988) observed in their computational studies that the onset of a merging process is linked to the proximity of vorticity and the streamline. Figure 1.4 presents the process based on experimental data. In the left image of Figure 1.4, the induced saddle point between two vortices is observed, indicating an unstable equilibrium. As vortex cores grow and reach the critical size relative to the separation distance, non-negligible vorticity begins to diffuse across the streamline separatrix. Ultimately, this leads to the destabilization of the saddle points and results in the merger of the vortex pair, a process that can be explained by the Biot-Savart law (Cerretelli and Williamson, 2003; Hopfinger and van Heijst, 1993; Meunier and Leweke, 2001). Furthermore, the presence of an unstable equilibrium implies that small perturbations can accelerate the onset of the merging process and the mutual inductance instability.

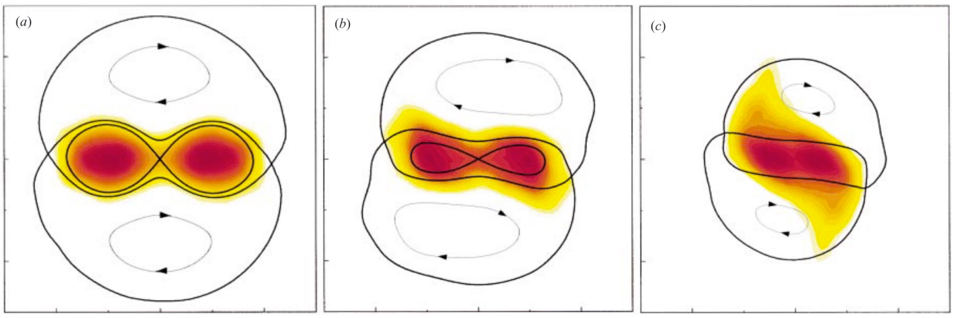

Figure 1.4: Experimental vorticity field and the streamline of a co-rotating vortex pair in a rotating frame, reproduced from Cerretelli and Williamson (2003)

The growth rate for mutual inductance instability has been found to increase with tip speed ratio (TSR), defined as $\lambda = \Omega R_0/U_\infty$, or the number of blades N_b (Felli et al., 2011; Okulov et al., 2014; Selçuk, 2016; Sherry et al., 2013). This increase is partly attributed to the decreased helical pitch h', which implies a smaller vortices separation distance $h = h'/N_b$. It is also partly due to the vortex circulation Γ, which is a result of higher loading conditions (J. N. Sørensen, 2011a). Consequently, by Quaranta et al. (2015), the relevant length and time scales of the growth rate of mutual inductance instability were found to be h and $2h^2/\Gamma$, respectively. One step further, from a simple approximation of helical pitch (see Equation 1.1), and the assumption that tip vortices travel downstream at a constant velocity, Biswas and Buxton (2024) introduced the convective pitch, expressed by $\pi D_0/\lambda$, instead of rotor diameter D as the length scale.

$$h = C_1 \frac{\pi D_0}{\lambda N_b} \tag{1.1}$$

1.1.2. Intentional disturbance to trigger leapfrogging

Previous studies have explored the various methods to impose small disturbances to trigger the leapfrogging phenomenon, thereby accelerating wake recovery. These methods can be categorized into two groups: active and passive. In the active approach, Quaranta et al. (2015) experimentally studied the relationship between instability growth rate and wave number. The control of instabilities with varying wave numbers was achieved by adjusting the rotational speed of a single-bladed rotor. Ivanell et al. (2010) introduced a small sinusoidal perturbation at the tip regions through numerical simulations. Subsequently, Odemark and Fransson (2013) conducted similar experiments by incorporating two pulsed jets behind the nacelle. Both studies revealed the crucial role of perturbation properties such as initial amplitude and frequencies in instability development. Huang et al. (2019) investigated the influences of two oscillating flaps near the tip and at mid-span on the tip vortex growth rate using LES. Additionally, Frederik et al. (2020) proved the concept of dynamic individual pitch control. Brown et al. (2022) advanced further to apply the oscillation on both rotational frequency and blade pitch. Such methods in essence are used to enhance the mixing process by actively adjusting the thrust force, despite the potential risk of structural damage from consequential fatigue loads. In the passive approach, Castellani et al. (2021) studied pitch imbalance through both numerical and experimental methods, despite a lower power coefficient under off-design conditions.

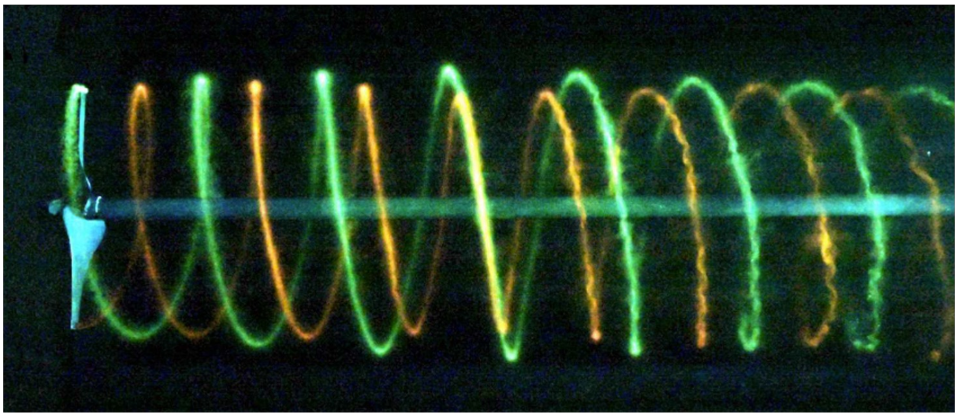

Figure 1.5: Dye visualization for the mutual-inductance instability triggered by radial offsets in a water channel experiment, taken from Quaranta et al. (2019)

Another passive method employed involves creating an asymmetric rotor configuration. Shown in Figure 1.5, Quaranta et al. (2019) conducted experiments in a water channel using a two-bladed rotor, with one blade having a slight radial offset. The resulting instability growth rate based on the displacement of the tip vortex cores aligns with the theoretical predictions by Gupta and Loewy (1974). Furthermore, the leapfrogging location and tip speed ratio relation were fitted to the linear model by Sarmast et al. (2014) under different tip speed ratios. Later on, the results were compared with the numerical studies by Abraham, Castillo-Castellanos, and Leweke (2023). They employed the periodic point vortex method introduced by Aref (1995) and the vortex filament model (Leishman et al., 2002). The sensitivity of radial offset, circulation imbalance, and tip speed ratio were conducted. The conclusion drawn emphasized that the point vortex method, despite its simplicity, effectively captures non-linear dynamics only under certain circumstances.

Similarly, Abraham, Ramos-García, et al. (2023) employed the DTU in-house multi-fidelity vortex method solver (Ramos-García et al., 2016; Ramos-García et al., 2023), to study leapfrogging by rotor asymmetry. The study emphasized the increased turbulence intensity (TI) and mean velocity in the downstream wake. Despite the absence of velocity deficit profiles downstream of a single wind turbine, the research extended its scope to investigate the impact on the entire wind farm. Furthermore, the study qualitatively predicted that introducing turbulence inflow could mitigate the effect of intentional disturbance. Last but not least, Abraham and Leweke (2023); Schröder et al. (2022) introduced blade add-ons, such as winglets or fins, to induce rotor asymmetry in their water channel experiments. The studies did not specifically investigate the modified wake structure's impact on downstream flow but captured the influence on leapfrogging distance or merging process.

1.2. Numerical methods in wind turbine wake

Fully capturing all details in wind turbine aerodynamics is expensive, requiring the use of methods that can effectively reduce costs to some extent. However, the choice of numerical methods involves a trade-off between computational cost and fidelity. This section will introduce various numerical methods and their characteristics. Subsection 1.2.1 discusses the some prevalent flow models, and Subsection 1.2.2 covers the turbine models. After the reasoning and discussion presented in the initial sections, Subsection 1.2.3 reviews the common properties of the methods selected for this work, showing the findings observed in previous studies.

1.2.1. An overview on wind turbine aerodynamics simulation

Numerical methods for studying wind turbine aerodynamics primarily utilize three groups of methods, ordered in ascending fidelity: Blade Element Momentum Theory (BEM), Vortex Methods, and Computational Fluid Dynamics (CFD). Firstly, BEM, developed by Glauert (1935), calculates blade loads and induction factors by applying 2D airfoil data and 1D momentum theory to the local blade elements. It offers the benefit of the lowest computational demand, albeit at the expense of numerous simplifying assumptions. To mitigate the assumptions inherent in BEM, various corrections have been integrated, such as Prandtl's tip loss correction (Betz, 1919). Secondly, the vortex method group simulates the wind turbine aerodynamics by representing the wake through discrete vortices, capturing the flow induced by turbine blades. A fundamental assumption of vortex methods is that flow throughout the domain is incompressible, inviscid, and irrotational (Leishman et al., 2002). Consequently, the Navier-Stokes equations are simplified to the Laplacian form. However, this simplification limits its capability to accurately predict the rotor wake characteristics. Turbulent diffusion and vortex core growth, which are critical in tip vortex region, are not inherently captured and thus require the hybrid methods or empirical corrections (Bhagwat and Leishman, 2002; H. Lee et al., 2022; H. Lee and Lee, 2019; Ramos-García et al., 2023).

The analysis of the near-wake region, however, requires the use of high-fidelity methods due to the presence of complex turbulence structures (Sanderse, 2009). This highlights the importance of CFD, which focuses on the full set of Navier-Stokes equations. As the highest-fidelity approach in CFD, direct numerical simulation (DNS) is capable of resolving eddies of all scales. Nevertheless, the Kolmogorov length scale, which represents the smallest eddies, was found to have a relationship with Reynolds number, expressed as $\eta \sim Re^{-3/4}$ (Westerweel et al., 2016). That is, with Reynolds numbers for large turbines typically on the order of $O(10^6)$, fully resolving the spectrum of eddies presents a substantial computational cost challenge.

Closure models have been developed to represent behaviors at smaller scales to achieve a compromise between computational costs and accuracy. Generally, two approaches are adopted: time filtering, as seen in Reynolds-averaged Navier-Stokes equations (RANS), or space filtering, which leads to large-eddy simulations (LES) (J. N. Sørensen, 2011b). The RANS methods involve Reynolds decomposition, where flow variables are divided into ensemble average and fluctuating components, denoted by the overline and prime, respectively, as shown in Equation 1.2.

$$u = \overline{u} + u' \tag{1.2}$$

Various models, ranging from zero-equation to two-equation types, have been developed to calculate the emerged Reynolds stress tensor in the momentum equation. This approach essentially means that only the average values are computed, while the complete spectrum of turbulence is modeled. Moreover, the use of RANS is more common for wind farm layout optimization instead of individual turbine (Antonini et al., 2020; King et al., 2017). They are also favored in scenarios where mean flow or power yield are of interest (Lin et al., 2023; Malecha and Dsouza, 2023; Plaza et al., 2015). Although the unsteady RANS (URANS) accounts for temporal dynamics, only a limited number of recent studies have applied it on HAWT to resolve the full rotor geometry due to high computational costs (Dai et al., 2017; Maizi et al., 2018).

For a deeper understanding of the physics behind wake evolution, a more sophisticated approach is required (Amiri et al., 2024; Bai and Wang, 2016; Mehta et al., 2014; Sarlak et al., 2016; Stovall et al., 2010). LES methods, which resolve the most energetic large eddies while modeling the smaller ones (Pope, 2000). This approach offers insights into the majority of eddies, providing a more comprehensive understanding of the wake dynamics. However, the accuracy achieved is at the expense of computational power. Hanjalic (2005) indicates that the computational demands for LES are $Re^{1.8}$ times higher than for RANS in the near wall region, and $Re^{0.4}$ times higher in free shear flows. One of the compromises is represented by hybrid LES/RANS approaches, such as detached eddy simulation (DES). The idea is to combine RANS in the boundary layer, and the LES in the separated regions, as implemented in the simulation around a single wind turbine blade in the works of Zhang et al. (2015) and Zhang et al. (2019). Another common compromise involves modeling the turbine through so-called actuator methods. These methods will be reviewed in the following subsection.

1.2.2. Actuator models for wind turbines

In the study of wind turbine wakes utilizing LES, turbines are frequently modeled through actuator methods to reduce computational costs, as mentioned in Subsection 1.2.1. These actuator models do not resolve boundary layers around the blade surface within the simulation. Instead, they implicitly calculate the performance by the tabulated airfoil data and subsequently apply corresponding body forces back to the flow field. There are actuator models including the standard actuator disk model (ADM-NR) (Burton et al., 2021), the rotating actuator disk model (ADM-R) (J. N. Sørensen and Kock, 1995), and the actuator line model (ALM) (J. N. Sørensen and Shen, 2002). Of which, the ADM-NR is valued for its simplicity and cost-effectiveness. This approach models the rotor as a porous disk, applying a thrust force uniformly across it to influence the flow field. Although the wake rotation, azimuthal, and radial invariance are not considered, the ADM-NR has been used in studies focused on the far wake, where the local details are less critical (Jimenez et al., 2007; Jimenez et al., 2009).

The ADM-R employs BEM theory to determine the radial distribution of lift and drag forces. As such, the disk is discretized into annulus, and it accounts for induced rotation to the flow and the non-uniform distribution of thrust. Wu and Porté-Agel (2011) conducted a comparative analysis of the ADM-R and ADM-NR within the LES framework, benchmarking against wind tunnel measurements. The findings indicate that both models provide reasonable predictions in the far-wake region (beyond $5D$ downwind). In the near-wake region, ADM-NR tends to overestimate the mean wind speed at the center of the wake while underestimating the turbulence intensity at the top-tip level.

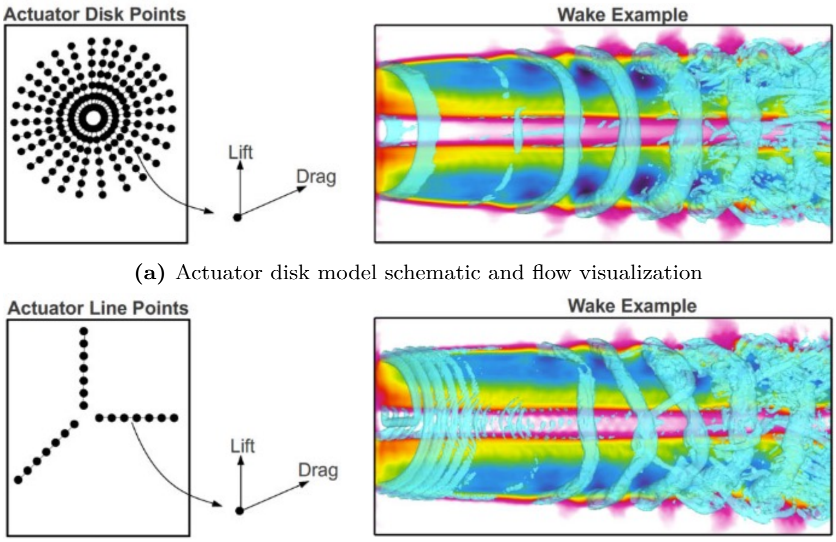

(a) Actuator disk model schematic and flow visualization

(b) Actuator line model schematic and flow visualization

Figure 1.6: A schematic showing turbine modeling of ADM/ALM (left), along with a visualization of the flow created by the ADM/ALM (right). Blue iso-surfaces represent Q criteria and the contours are of streamwise velocity, reproduced from Martínez-Tossas et al. (2015)

On the other hand, the ALM replaces wind turbine blades into line segments, discretized into elements that exert forces on the flow field. This enables the ALM to account for the individual tip and root vortices, providing an advantage over the ADM which averages these effects (Mehta et al., 2014). A comparison by Martínez-Tossas et al. (2015) between the ALM and ADM-R using LES on flow past HAWT shows that both models predict similar power outputs but differ in instantaneous near-wake. This variation arises from differences in their nature. ALM, with its individual line, enables the formation of distinct tip and root vortices that spiral downstream—a capability absent in ADM-R. Consequently, this leads to variations in vortex breakdown, where the interaction between tip and root vortices disrupts the symmetrical breakdown process observed

Table 1.1: Research on HAWT using LES-ALM

Author(s) and Year	Turbine/aerofoil	Software (solver)
Troldborg (2009)	Tjæreborg & NM80	EllipSys3D
Ivanell et al. (2010)	Tjæreborg	EllipSys3D
Churchfield et al. (2012)	NREL 5MW	OpenFOAM
Jha et al. (2014)	NREL 5MW & Phase VI	OpenFOAM
Sarmast et al. (2014)	NREL 5MW & Tjæreborg	EllipSys3D
Xie and Archer (2015)	Siemens SWT-2.3-93	WiTTS
Sarlak et al. (2016)	NREL S826	EllipSys3D & LESGO
Benard et al. (2018)	Tjæreborg	YALES2
Mendoza et al. (2019)	NREL 5MW	OpenFOAM
Onel and Tuncer (2021)	NREL 5MW	OpenFOAM
Xue et al. (2022)	NREL 5MW	Fluent
Arabgolarcheh et al. (2022)	NREL 5MW & Phase VI	OpenFOAM
Li (2023)	NREL 5MW & 1/75 DTU 10MW	OpenFOAM

in ADM-R, as depicted in Figure 1.6. Similarly, Troldborg (2009) pointed out that the ADM is limited to symmetric flow conditions due to even load distribution in the azimuthal direction. These findings suggest that employing ALM is beneficial to studying near-wake flow details, such as tip vortices, while ADM is a less expensive alternative when the far-wake region is of interest.

1.2.3. Actuator line model in Large eddy Simulation

Recently, there have been numerous studies that have combined LES with ALM to investigate the behavior of wind turbine wakes. Table 1.1 presents some of these studies, summarizing their choices of turbine models, software, and LES subgrid-scale models. Among these studies, some common settings and characteristics can be observed:

1. **Reduction of computation costs by ALM**
   The comparison between studies using different models with similar cell numbers and temporal discretization was made by Arabgolarcheh et al. (2022). It demonstrated that LES-ALM requires three orders of magnitude less computational time than blade-resolved LES and two orders of magnitude less than blade-resolved RANS.

2. **Solvers and the subgrid scale model**
   Various solvers have been utilized in these studies, with OpenFOAM being the most frequently used, alongside other LES research codes from the wind energy community. These research solvers differ in their numerical discretization approaches. Martínez-Tossas et al. (2018); Nathan et al. (2017) conducted a comparison of these solvers focusing on wind turbine wakes and rotor performance respectively. The differences in numerical discretization lead to variations in the transition to turbulence but do not affect the quantity along the blades. Furthermore, the Smagorinsky model stands out as the most widely adopted sub-grid scale model in wind turbine wake research, which will be later introduced in Section 2.1.

3. **Validation based on the power and thrust (coefficients)**
   Among these simulations, and broadly within the wind energy community, the most commonly used metrics are the power and thrust coefficients. While some studies (Jha et al., 2014; Troldborg, 2009), delve into the sensitivity of local parameters on the blade region, specifically investigating the induction factor along the blade, the majority of research focuses on comparing these two principal turbine performance metrics in validations and convergence tests. They compare their results with either the experimental data or the numerical results from the literature. Obviously, access to a more extensive set of reference data can enhance researchers' confidence in validation. This could serve as a reason for the low variation in the tested turbine.

4. **The investigation of tip vortices without the nacelle geometry**
   This absence can result in inaccuracies in predicting the breakdown of hub vortices and the meandering of the far wake (Kang et al., 2014; Xie and Archer, 2015). While the ALM features strong predictive capabilities for tip vortices, the lack of consideration for the nacelle isolates the tip vortex when studying its stability (Ivanell et al., 2010; Sarmast et al., 2014).

1.3. Research scope

The scope of this research is presented here in the form of the research gap, a research objective, and research questions.

1.3.1. Research gap

This subsection identifies research gaps in the literature. As reviewed in Subsection 1.1.2, earlier work (Abraham, Castillo-Castellanos, and Leweke, 2023; Abraham and Leweke, 2023; Abraham, Ramos-García, et al., 2023; Quaranta et al., 2019), has shown that minor radial offsets can accelerate the development of leapfrogging instability. While these findings provide an understanding of rotor asymmetry's influence on turbine wake behavior, they also motivate the need for further exploration.

A critical gap remains in understanding whether this asymmetry impacts wake recovery. Previous efforts have primarily addressed the early stages of tip vortex instability, leaving the relationship between this phenomenon and momentum entrainment underexplored. The actual gain on wake recovery, such as an analysis of downstream velocity profiles, was not documented in the literature. Moreover, only a minor asymmetry has been applied on the rotor since the focus was the growth rate of leapfrogging. Namely, no study until now has explored the aerodynamic impact of introducing a larger radial offset—a more developed form of leapfrogging motion—directly to the rotor. Additionally, the numerical studies mentioned utilize Vortex Methods, which are essentially inviscid as outlined in Subsection 1.2.1. While these methods can predict the onset of mutual inductance instability, they do not accurately capture the subsequent vortex merging process where the diffusion takes place (Walther et al., 2007). This suggests that higher-fidelity models are necessary for a comprehensive understanding of wake recovery. Furthermore, the effect of turbulent inflow conditions, specifically in the context of radial offsets, remains an underexplored area. With ambient turbulence known for its mixing capabilities, it is expected that momentum entrainment could be more pronounced compared to laminar inflow conditions. However, the impact of turbulence on enhancing or mitigating the effects of radial offsets on wake recovery has yet to be determined (Abraham, Ramos-García, et al., 2023).

1.3.2. Research objective

The research gaps point the current study towards the following research objectives:

1. Investigate the effect of asymmetric rotor on turbine tip vortices behavior
2. Examine the impact of blade length differences on turbine tip vortices behavior
3. Determine potential benefits in terms of wake recovery

1.3.3. Research questions

The research questions below are formulated with the aim of achieving the objective:

1. **Impact of rotor asymmetry on tip vortices behavior:**
   (a) How does rotor asymmetry in terms of blade length difference affect tip vortex behavior?
   (b) What correlation exists between the degree of blade length difference and its impact on leapfrogging instability?
2. **Rotor asymmetry's influence on wake recovery:**
   (a) In what way does rotor asymmetry in terms of blade length difference influence wake recovery?
   (b) Does the influence of rotor asymmetry on wake recovery alter with the inflow turbulence level?

1.4. Thesis outline

Chapter 1. Introduction

This chapter introduces the research background on leapfrogging instability and numerical methods, reviews the state-of-the-art studies, and defines the research scope.

Chapter 2. Methodology

This chapter describes the methodology used in the current result. First, the theory behind LES, ALM, and the solver used for implementation will be introduced. Then, physical properties in the research context and proposed methods will be defined.

Chapter 3. Simulation setup and validation

This chapter details the simulation settings and validation on them, including a convergence study and benchmarking against prior work.

Chapter 4. Result: Tip vortex behaviors

This chapter presents the local tip vortex behaviors induced by blade length differences, based on LES-ALM results. The primary focus of the analysis is on the vortex pair trajectory up to the leapfrogging distance.

Chapter 5. Result: Wake characteristics

This chapter investigates global wake characteristics and the impact on wake recovery based on LES-ALM results.

Chapter 6. Conclusion and recommendation

This chapter presents concluding remarks by discussing the proposed research questions, followed by the recommendation for future work.

2

Methodology

This chapter presents the methodologies used in the current study. Section 2.1 to Section 2.3 introduce the methods used to simulate the wind turbine wake. Then, the following sections define the quantification and normalization.

2.1. Large Eddy Simulation

In Large Eddy Simulation (LES), certain eddies are modeled, while the rest are resolved using the filtered Navier-Stokes equations. This approach situates the fidelity of LES between that of DNS and RANS methods, leveraging a balance of accuracy and computational cost. The filtered process of a physical property ζ is shown in Equation 2.1 and Equation 2.2. Furthermore, the governing sets of filtered equations are denoted by Equation 2.3 for the continuity equation and Equation 2.4 for the Navier-Stokes equations. The tilde symbol in these equations denotes filtered properties, while the double prime symbol represents the residual properties. Similar to the additional Reynolds stress tensor in RANS modeling, the filtered non-linear term in LES cannot be directly computed. Instead, it is represented by τ_{ij}, known as the residual-stress tensor or subgrid-scale (SGS) stress tensor, shown in Equation 2.5 and Equation 2.6. It should be noted that the naming of the tensor is based on the dependency on filtering and grid employment (Pope, 2000).

$$\zeta(x) \xrightarrow[\text{Fourier transform}]{\mathcal{F}} \hat{\zeta}(k) \xrightarrow[\text{Filter kernel}]{G(k)} G(k)\hat{\zeta}(k) \xrightarrow[\text{Inverse Fourier transform}]{\mathcal{F}^{-1}} \widetilde{\zeta}(x) \tag{2.1}$$

$$\zeta(x) = \widetilde{\zeta(x)} + \zeta(x)'' \tag{2.2}$$

$$\frac{\partial \widetilde{u}_i}{\partial x_i} = 0 \tag{2.3}$$

$$\frac{\partial \widetilde{u}_i}{\partial t} + \frac{\partial \widetilde{u_i u_j}}{\partial x_j} + \frac{1}{\rho}\frac{\partial \widetilde{p}}{\partial x_i} - \nu \frac{\partial^2 \widetilde{u}_i}{\partial x_j \partial x_j} - \frac{\widetilde{F_{\text{body},i}}}{\rho} = 0 \tag{2.4}$$

$$\frac{\partial \widetilde{u}_i}{\partial t} + \frac{\partial \widetilde{u}_i \widetilde{u}_j}{\partial x_i} + \frac{1}{\rho}\frac{\partial \widetilde{p}}{\partial x_i} - \nu \frac{\partial^2 \widetilde{u}_i}{\partial x_j \partial x_j} - \frac{\widetilde{F_{\text{body},i}}}{\rho} = \frac{\partial \tau_{ij}}{\partial x_j} \tag{2.5}$$

$$\frac{\partial \tau_{ij}}{\partial x_j} = \frac{\partial \widetilde{u_i u_j}}{\partial x_j} - \frac{\partial \widetilde{u}_i \widetilde{u}_j}{\partial x_j} \tag{2.6}$$

The introduction of the subgrid-scale (SGS) tensor as an additional unknown complicates the system of equations, giving rise to the *closure problem*. To close the equation, this study employs the Smagorinsky model (Smagorinsky, 1963), the simplest and most widely used approach within the LES-ALM context. The model distinguishes itself through two primary characteristics. Firstly, it models the deviatoric part of the SGS stress tensor using a linear viscosity model, as illustrated in Equation 2.7. This approach not only establishes a relationship between the filtered properties— the shear strain rate tensor (S_{ij}, Equation 2.8)—and the modeled scale behavior but also presents an artificial viscous force that is exerted back onto the filtered flow. Besides, the diagonal terms of the SGS tensor can be further expressed through SGS kinetic energy, by analogy to the turbulence kinetic energy in RANS.

$$\begin{aligned} \tau_{ij} &= \frac{1}{3}\tau_{kk}\delta_{ij} + (\tau_{ij} - \frac{1}{3}\tau_{kk}\delta_{ij}) \\ &\approx \frac{1}{3}\tau_{kk}\delta_{ij} - 2\nu_{\text{sgs}} dev(S_{ij}) \\ &= \frac{2}{3}k_{\text{sgs}}\delta_{ij} - 2\nu_{\text{sgs}} dev(S_{ij}) \end{aligned} \tag{2.7}$$

$$S_{ij} = \frac{1}{2}(\frac{\partial \widetilde{u}_i}{\partial x_j} + \frac{\widetilde{u}_j}{\partial x_i}) \tag{2.8}$$

Secondly, similar to the mixing length hypothesis, the SGS viscosity is modeled as Equation 2.9. The Smagorinsky length scale, ($C_s\Delta$), is intended to correspond to the characteristic length scale of the modeled eddies. Consequently, given that Δ denotes the filter size, the Smagorinsky constant, C_s is expected to be less than 1. For homogeneous isotropic turbulence, C_s is approximately 0.17, as estimated by (Lilly, 1967). It should be noted that $|\mathbf{S}|$ stands for the magnitude of the shear strain rate tensor, as shown by Equation 2.10, where ':' denotes the double inner product operation.

$$\nu_{\text{sgs}} = (C_s\Delta)^2|\mathbf{S}| \tag{2.9}$$

$$|\mathbf{S}| = \sqrt{2S_{ij} : S_{ij}} \tag{2.10}$$

One limitation of the basic Smagorinsky model lies in its use of a constant value for C_s, which implies an assumption of Homogeneous Isotropic Turbulence (HIT) and fails to account for spatial variations in turbulence characteristics (Mehta et al., 2014). Specifically, in regions close to walls, the characteristic length scale is not constant but rather depends on the distance to it. This limitation has motivated the development of near-wall corrections, such as the van Driest damping function (Van Driest, 1956). However, the importance of selecting an appropriate wall-damping function diminishes when employing the actuator line model and ignoring the ground. Thus, no direct "surface" interaction occurs within the domain.

Dynamic models such as Germano identity (Germano, 1992) provide a methodology to adaptively determine the local value for C_s, account for the backscatter and over-predicted dissipation. However, the impact of these differences becomes less pronounced at higher resolutions of the actuator line (exceeding 30 mesh points per actuator line) (Sarlak et al., 2015). Furthermore, in the near-wake region and in the presence of turbulent inflow, variations resulting from the Smagorinsky constant are minimal (Martínez-Tossas et al., 2015). Therefore, this research applies the simplest form of the Smagorinsky model, employing grid size as a filter.

2.2. Actuator Line Model

In this section, the turbine model - actuator line - will be introduced. Subsection 2.2.1 describes the modeling approach, followed by Subsection 2.2.2 and Subsection 2.2.3, which depicts a parameter that controls the projection manner and the required correction due to tip-loss effect respectively.

2.2.1. Model description

The Actuator Line Model (ALM), developed by J. N. Sørensen and Shen (2002), offers a methodology to represent a rotating turbine. This approach simplifies turbine blades into lines that rotate in space, projecting resultant forces onto the flow field as body forces. These forces are determined from 2D tabulated airfoil data at each discretized element, depending on the local inflow condition. In other words, this method is considered inviscid concerning the turbine's presence, as the viscous effects from boundary layers are implicitly captured within the tabulated airfoil data obtained from prior experiments. By adopting such an approach, computational costs and meshing complexity are significantly reduced, as the solver is not required to resolve boundary layer details. Consequently, computational resources can be more effectively applied to analyzing wake behavior.

The body force exerted on the flow field is determined using blade element theory, where actuator lines are discretized into individual blade elements. Figure 2.1 illustrates the force and velocity vector diagram for a 2D airfoil section. The local force on each blade element is calculated using Equation 2.11 to Equation 2.13. First, the streamwise and velocity components, U_n and $-\Omega r + U_\theta$ are obtained from the flow solver and the prescribed rotational frequency. Then, the local apparent wind velocity U_a at a radial position r on the centroid of a blade element can be determined as follows:

$$U_a = \sqrt{U_n^2 + [-\Omega r + U_\theta]^2} \tag{2.11}$$

Subsequently, the inflow angle, Φ, is derived from the velocity geometry, and the angle of attack is calculated considering the local pitch angle γ.

$$\Phi = \tan(\frac{U_n}{-\Omega r + U_\theta}), \qquad \alpha = \Phi - \gamma \tag{2.12}$$

Utilizing the angle of attack, lift and drag coefficients are obtained from tabulated polar data. Finally, the sectional normal force and the azimuthal force ($n-$and $\theta-$ direction in Figure 2.1) can be obtained by lift and drag force vector projection.

$$\boldsymbol{f}_{2D} = \frac{1}{2}\rho U_a^2 c\,(C_L(\alpha)\boldsymbol{e}_L, C_D(\alpha)\boldsymbol{e}_D) \tag{2.13}$$

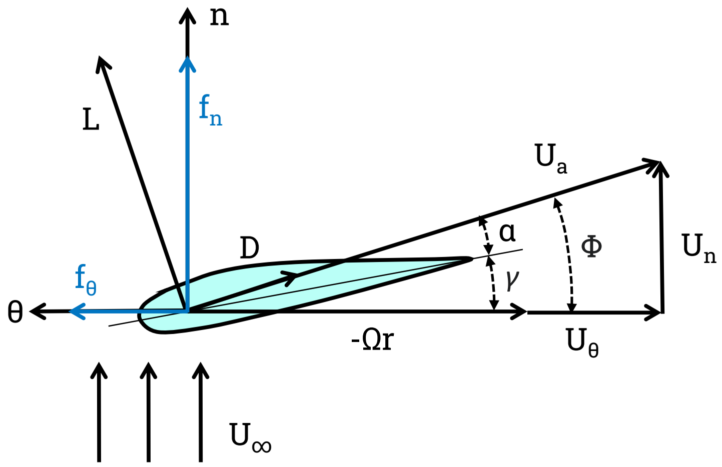

Figure 2.1: Diagram of force and velocity vectors on a cross-sectional blade element

The calculated sectional force $\boldsymbol{f}_{2\text{D}}$ is corrected by tip-loss factor $F_1(r)$, then being projected onto the cells in the CFD domain as body forces using Equation 2.14 and Equation 2.15. This projection applies convolution of sectional forces with the regularization kernel η_ϵ, which distributes the force in a Gaussian manner to prevent spatial singularity. In both equations, $|\boldsymbol{x} - r\boldsymbol{e}_i|$ denotes the distance between the cell centroids and points on the ith actuator line, with ϵ acting as the smoothing parameter to adjust the distribution of the regularized load (J. N. Sørensen and Shen, 2002).

$$\boldsymbol{f}_{\text{body}} = \boldsymbol{f}_{2\text{D}} \otimes \eta_\epsilon, \qquad \eta_\epsilon(|\boldsymbol{x} - r\boldsymbol{e}_i|) = \frac{1}{\epsilon^2 \pi^{3/2}} \exp[-(\frac{|\boldsymbol{x} - r\boldsymbol{e}_i|}{\epsilon})^2] \tag{2.14}$$

$$\boldsymbol{f}_{\text{body}}(\boldsymbol{x}) = \sum_{i=1}^{N_b} \int_0^R F_1(r) \boldsymbol{f}_{2\text{D}}(r) \eta_\epsilon(|\boldsymbol{x} - r\boldsymbol{e}_i|) dr \tag{2.15}$$

Pointed out by Jha et al. (2014), the most important ALM parameters are smoothing parameters ϵ, grid spacing Δ along the actuator line, and the discretization of the actuator line Δ_b. The discussion on the smoothing parameter is presented in Subsection 2.2.2. The settings of them will be documented in Chapter 3.

2.2.2. Smoothing parameter ϵ

Smoothing parameter ϵ controls the manner of body force projection to the mesh (J. N. Sørensen et al., 1998). A small ϵ concentrates the force at a point and induces singularity, whereas a large ϵ spreads body force throughout the domain as a background offset.

The choice of smoothing parameter has been studied in a prior effort. First, Troldborg (2009) performed a sensitivity analysis varying ϵ in proportion to the resolution of the actuator line, Δ_b. It was identified that the $\epsilon = 2\Delta_b$ is a compromise that mitigates numerical oscillation while preserving the tip-root vortex structures. Secondly, Martínez-Tossas et al. (2015) conducted a similar test but scale ϵ with the grid size Δ. The result shows that $\epsilon < 2\Delta$ oscillation occurs and that a small value of ϵ causes the early wake transition.

2.2.3. End effect correction

The Shen correction (Shen et al., 2005) was used to account for the tip-loss (end) effect in the current study. The tip loss correction was first developed by Glauert (1935) for BEM, dealing with the continuity of pressure around the blade tip due to the finite number of blades. In ALM, this ad hoc correction seems unnecessary since the performance is computed on each blade locally. However, the over-prediction of loading at blade tips was always observed using ALM. This over-prediction, stemming from the imprecision of chord-wise loading distribution in actuator lines, suggests the need for a correction to ensure the loading converges to zero at the tip (Sarlak et al., 2016; J. N. Sørensen et al., 2016).

On the foundation of Glauert's, Shen's model introduces modification to the loads at each radial position. Equation 2.16 shows the modified resultant force coefficient (C_n,C_θ) by the correction factor F_1 from the 2D tabulated airfoil data. The following Equation 2.17 and Equation 2.18 show the expression of F_1 and its empirical constant obtained from the experiments, where $s_1 = 0.125$ and $s_2 = 21$.

$$C'_n = F_1 C_n, \quad C'_\theta = F_1 C_\theta \tag{2.16}$$

$$F_1(r) = \frac{2}{\pi}\cos^{-1}[\exp(-g\frac{N_b(R-r)}{2R\sin\phi})] \tag{2.17}$$

$$g = \exp[-s_1(N_b\lambda - s_2)] + 0.1 \tag{2.18}$$

2.3. Flow solver - OpenFOAM v2106

In this research, `OpenFOAM v2106` (OpenFOAM Foundation, 2021) was employed as the simulation solver. This software is an open-source C++ toolbox designed for the simulation of continuum mechanics, mostly in the field of CFD. It offers a high degree of flexibility, allowing users to compile custom libraries to solve the specific problem. In this section, the implementation of the Smagorinsky model and actuator line model in OpenFOAM will be introduced.

2.3.1. Smagorinsky model in OpenFOAM

In OpenFOAM, the Smagorinsky model is implemented based on the turbulent kinetic energy (TKE) equations developed by Deardorff (1980) and Moeng (1984). Therefore, the specification of the Smagorinsky constant C_s is achieved indirectly via its model constants, C_k and C_ϵ. These constants are defined as follows:

$$\nu_{\text{sgs}} = C_k \Delta k_{\text{sgs}}^{0.5} \tag{2.19}$$

$$S_{ij} : \tau_{ij} + C_\epsilon \frac{k_{\text{sgs}}^{1.5}}{\Delta} = 0 \tag{2.20}$$

It should be noted that Equation 2.20 represents the assumption of the local equilibrium of production and dissipation in the subgrid-scale. Moreover, combining Equation 2.19

and Equation 2.20 with Equation 2.7 and assuming incompressible flow, the subgrid-scale TKE k_{sgs} and eddy viscosity ν_{sgs} can be expressed as follows:

$$k_{\text{sgs}} = \frac{C_k \Delta^2 |S_{ij}|^2}{C_\epsilon} \tag{2.21}$$

$$\nu_{\text{sgs}} = C_k \sqrt{\frac{C_k}{C_\epsilon}} \Delta^2 |S_{ij}| \tag{2.22}$$

By equating Equation 2.9 and Equation 2.22, the relation between the model constants and the Smagorinsky constant can be obtained as Equation 2.23.

$$C_s^2 = C_k \sqrt{\frac{C_k}{C_\epsilon}} \tag{2.23}$$

The current research sets the model constants as follows, $C_k = 0.094$ & $C_\epsilon = 1.048$, resulting in $C_s = 0.1677$.

2.3.2. TurbineFoam - An OpenFOAM library of ALM

The actuator line model is employed by the `turbineFoam` library, an open-source extension for OpenFOAM (Bachant et al., 2019). This library not only simplifies the procedure of setting up a turbine in the simulation domain but also preserves flexibility. The characteristics of the turbine, such as the radius and tip speed ratio, are parameterized and can be defined in `fvOptions`, where the body forces are specified in the OpenFOAM code architecture. Moreover, blade properties are allowed to be modified on individual actuator lines. Additionally, the library features modules for not only dynamic stall and added mass to capture unsteady phenomena but also end effects. This provides the convenience of having an implementation of the asymmetric rotor.

2.4. Definition of blade length difference

With the research objective in mind, this study aims to study the influence of rotor asymmetry. Subsection 2.4.1 presents the methodology to create the difference in blade length, while Subsection 2.4.2 introduces new parameters to account for the loss of thrust due to the decrease in blade length.

2.4.1. Blade truncation

Rotor asymmetry is carried out by directly truncating one of the blades while leaving the other(s) unmodified. The rationale behind this off-design choice is that the focus of this study is wake behavior instead of iterative blade profile design. Given that no actual rotors are manufactured at this stage, blade truncation serves as a practical solution due to its simplicity. In this context, neither rotational imbalance nor counterweight is considered inside the scope, as actuator lines do not have ”mass” in the flow domain and no shaft was employed.

Two things should be noted in terms of implementation. First, the spacing of actuator line elements Δ_b remains the same on all blades as shown in Figure 2.2. That is, a truncated blade is defined by fewer actuator line elements. Second, the unchanged blade length is denoted by R_0, and the truncated is denoted by $R_{\Delta r}$.

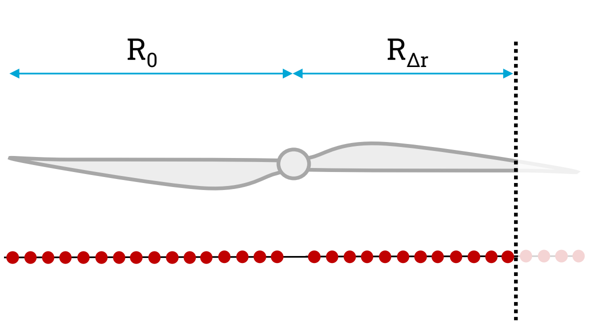

Figure 2.2: Diagram of blade truncation and corresponding blade elements

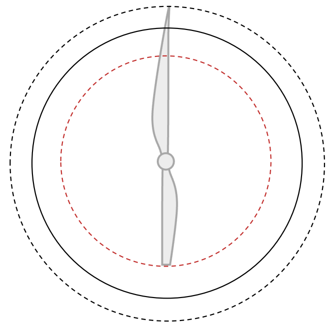

Figure 2.3: Effective swept area A_e (by black solid line), the original blade swept area A_0 (by black dotted Line), and the truncated blade swept area $A_{\Delta r}$ (by red dotted line). Not to scale.

2.4.2. Effective Swept area and diameter

The effective swept area and diameter are defined to reflect the thrust loss resulting from rotor asymmetry. While the frontal area of the modified turbine remains unchanged, the total thrust decreases due to the truncation of one blade. The rotor diameter D_0, traditionally used as the characteristic length scale, is not representative in the wake study. Thus, an effective diameter is required to describe the modified rotor.

In this study, the effective diameter is proposed to be area-based. Given that performance coefficients in wind energy fields are usually normalized by area, the effective swept area A_e is defined as the average of the original swept area and the swept area by the truncated blade, as shown in Figure 2.3 and Equation 2.24.

$$A_e \equiv \frac{A_0 + A_{\Delta r}}{2} = \pi[R_0^2 - R_0\Delta r + \frac{\Delta r^2}{2}] \tag{2.24}$$

where

$$A_0 = \pi R_0^2\,, \qquad A_{\Delta r} = \pi(R_0 - \Delta r)^2 \tag{2.25}$$

The effective diameter D_e is then determined by taking the square root of the effective swept area, shown by Equation 2.26.

$$D_e = D_0 * \sqrt{1 - \frac{\Delta r}{R_0} + \frac{\Delta r^2}{2R_0^2}} \tag{2.26}$$

The motivation behind this definition is to consider the thrust loss resulting from rotor asymmetry. An advantage of normalizing by area over by thrusts is the simplicity of post-processing, no iterative process is needed. The verification of the power and thrust coefficients based on the effective swept area will be demonstrated in Subsection 3.3.4.

2.5. Definition of leapfrogging distance and time

Figure 2.4 depicts a series of vortex pairs undergoing the leapfrogging and merging phenomenon as they convect in the x-direction. As discussed in Subsection 1.1.1, leapfrogging occurs when a pair of tip vortices start to roll up with each other. The leapfrogging distance, x_{LF}, quantifies where the leapfrogging event takes place. Following Quaranta et al. (2019), x_{LF} is measured from the generation of the tip vortices (rotor plane) to the position where the vortex cores are aligned at a 90° relative to the x-direction, indicating they swap their streamwise position.

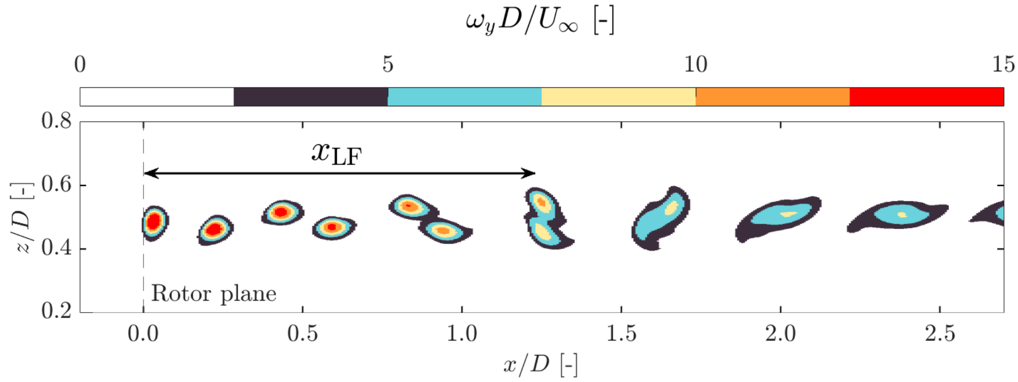

Figure 2.4: Leapfrogging and merging of vortex pairs, with x_{LF} marking the distance from the origin to the onset of leapfrogging

In addition, the leapfrogging time is defined to generalize the vortex pair evolution without convection. Following the work of Abraham, Castillo-Castellanos, and Leweke (2023), this involves transforming the leapfrogging distance by the convective speed of the tip vortex, which is approximated by the helical pitch h' and the rotational frequency of the rotor f. The definition is expressed in Equation 2.27. In addition, the relevant time scale for long wave instability development has been proposed as Equation 2.28. Quaranta et al. (2015) proposed this time scale by approximating the helix convection speed and the helical pitch, while Selçuk (2016) derived it starting from the growth rate in a two-dimensional vortex model. This time scale will be further used to normalize the leapfrogging time and its growth rate.

$$t_{\mathrm{LF}} = x_{\mathrm{LF}} \frac{1}{u_c} = x_{\mathrm{LF}} \frac{1}{h' f} \tag{2.27}$$

$$t^* = t \frac{\Gamma}{2h^2} \tag{2.28}$$

2.6. The growth of leapfrogging instability

In the literature, there are several approaches to define the growth of leapfrogging instability. Widnall (1972), Gupta and Loewy (1974), Ivanell et al. (2010) and Sarmast et al. (2014) analyze the relevant modes in the frequency domain, while in Bolnot (2012) and Quaranta et al. (2019) conduct their studies in the time domain. In the current study, the growth rate is also investigated in the time domain, however, with a different definition.

In Bolnot (2012) and Quaranta et al. (2019), the growth rate of the instability is defined based on the difference in the separation distance between a vortex and its two neighboring ones. Although this method calculates a growth rate of $\pi/2$ following findings in the literature (Sarmast et al., 2014; Selçuk, 2016), this definition in essence only considers the streamwise separation between a pair of vortices. Furthermore, existing theoretical growth rates derived from the linearized model, such as those of Gupta and Loewy (1974), are obtained through the eigenvalue problem, which involves linearization around the equilibrium point. However, the main variable ($\Delta r/R_0$) tested in this study does not permit such a condition. The system with an imposed radial offset of the two-vortex array is inherently unstable. Namely, when blade length difference cannot be considered a small number, the initial points are far from the equilibrium point perturbation.

Hence, an alternative definition is proposed to consider two degrees of freedom, both streamwise and radial vortex separation. This method is on the basis of a general point vortex row model introduced by Aref (1995), but specializes in a zero-wavenumber perturbation and focuses on the temporal variation of separation distance between vortex pairs. Moreover, this definition only requires the information from vortex pairs rather than trios compared to Quaranta et al. (2019), simplifying post-processing and expanding the available data field. To further explain this model, Subsection 2.6.1 proposes the 2D point vortex model. On this basis, Subsection 2.6.2 presents the methodology to determine the growth rate of the leapfrogging instability. The convergence study and the validity of linearization will be presented in the next chapter.

2.6.1. 2D point vortex model

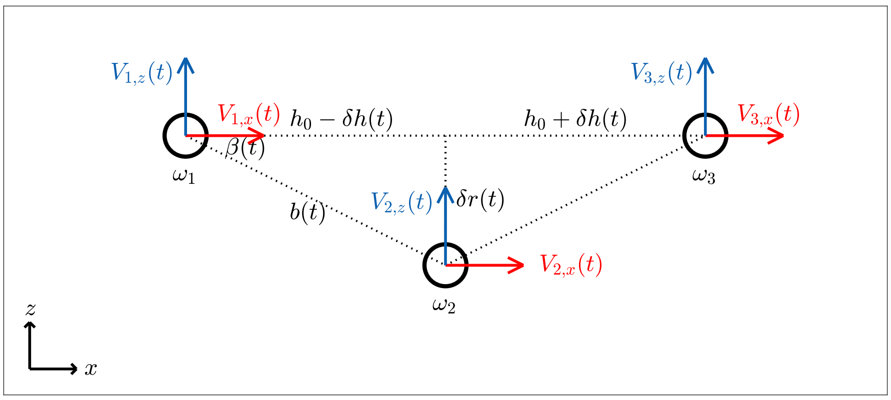

Figure 2.5: Diagram of 2D point vortex model

A classic two infinite arrays of co-rotating vortices are used to represent the tip vortices shed from two blades of different lengths in this study. Unlike the approach proposed by Abraham, Castillo-Castellanos, and Leweke (2023), which considers helical effects, this model neglects such influences, treating the vortices as purely two-dimensional (or as three-dimensional with straight filaments oriented perpendicular to the plane of the paper). Figure 2.5 illustrates the smallest unit within these infinite vortex arrays. The model starts by considering the displacement of individual vortices in the x(streamwise) and z(radial) directions. Subsequently, the variation of distance between these individual vortices is defined for the degrees of freedom in the system.

To begin with, three main assumptions are made in this model:

1. A point vortex is displaced solely by the induction velocity from other inducing point vortices on both sides of the $\pm x$ direction.
2. The initial vortex separation h_0 and the variation δh and δr are uniform along these infinite vortex array.
3. Circulation is constant for all vortices.

Based on the first assumption, a state space describing the displacement of ith vortex is formulated in Equation 2.29. According to Figure 2.5, the index i distinguishes the positioning within the array, where even i corresponds to vortices in the upper row and odd i to those in the lower row.

$$\frac{d}{dt}\begin{bmatrix}\delta x_i \\ \delta z_i\end{bmatrix} = \begin{bmatrix}V_{i,x} \\ V_{i,z}\end{bmatrix} \tag{2.29}$$

The induction velocity $V_{i,x}$ and $V_{i,z}$ can be further written as the resulting induction from other vortices in Equation 2.30 and Equation 2.31 by the Biot Savart law. Here, V_{ji} represents the induced velocity by the jth vortex on the ith vortex. The index j ranges from 1 to $2N_p$, where N_p denotes the number of inducing vortices surrounding the ith vortex on both $\pm x$ sides.

$$V_{i,x} = \sum_{j=1}^{2N_p} V_{ji,x} = \sum_{j=1}^{2N_p} \frac{\Gamma}{2\pi} \frac{z_j - z_i}{(x_j - x_i)^2 + (z_j - z_i)^2} \tag{2.30}$$

$$V_{i,z} = \sum_{j=1}^{2N_p} V_{ji,z} = \sum_{j=1}^{2N_p} \frac{\Gamma}{2\pi} \frac{x_j - x_i}{(x_j - x_i)^2 + (z_j - z_i)^2} \tag{2.31}$$

where

$$x_j - x_i = \begin{cases} 0 & i = j \\ (-1)^i (jh_0 + \delta h) & i \neq j;\ j \ is \ odd \\ (-1)^i [(1-j)h_0 + \delta h)] & otherwise \end{cases} \tag{2.32}$$

$$z_j - z_i = (-1)^i \delta r \tag{2.33}$$

Based on the second and third assumptions, the magnitude of induction is identical for both arrays and uniform across all vortex pairs, i.e., $V_x = |V_{i,x}|$ and $V_z = |V_{i,z}|$, although their directions are opposite between the arrays. This indicates that the vortex pair rotates around each other on a symmetric trajectory (ω_1 and ω_2 in Figure 2.5 with a positive Γ). More specifically, they travel with $\pm V_x$ and $\pm V_z$ in x and z direction, namely, the variation of horizontal δh and vertical δr separations between the vortex pair change at rates of twice V_x and V_z, as described in Equation 2.34.

$$\frac{d}{dt}\begin{bmatrix}\delta h\\ \delta r\end{bmatrix} = \begin{bmatrix}2V_x(\delta h, \delta r)\\ 2V_z(\delta h, \delta r)\end{bmatrix} \tag{2.34}$$

This formation offers several advantages. First, the assumptions employed allow for only the information from a vortex pair to be needed as initial inputs even though the derivation involves an infinite vortex array. Second, since displacement within the infinite vortex array is uniform, the temporal evolution is identical for any pair in the array. Consequently, studies on growth rates of vortex pairing phenomena need only focus on a single pair.

2.6.2. Definition of growth rate

As derived in the previous subsection, a non-linear system Equation 2.34 describes the motion of vortex pairing due to a radial offset on an array. By applying a Taylor expansion for linearization, this approach leads to an eigenvalue problem, as detailed in Equation 2.35, where $\mathbf{J}$ denotes the Jacobian matrix.

$$\frac{d}{dt}\begin{bmatrix}\delta h\\ \delta r\end{bmatrix} = \mathbf{J}\begin{bmatrix}\delta h\\ \delta r\end{bmatrix} \tag{2.35}$$

By solving the eigenvalue problem, as shown in Equation 2.36, a linearized solution is obtained featuring two modes with real eigenvalues of opposite signs, where $\lambda_1 = -\lambda_2 > 0$. This eigenvalue set indicates that the first mode is unstable and expected to grow exponentially over time, while the second mode decays. Here, λ_1 is served as the growth rate of the unstable mode. Besides, the normalized growth rate (by the relevant time scale) converges to $\pi/2$, consistent with the literature. This convergence occurs with N_p and remains independent of h_0 and Γ. The convergence study on N_p will be presented in Subsection 3.4.1. Furthermore, the resulting eigenvectors are $\boldsymbol{v_1} = [1; 1]$ and $\boldsymbol{v_2} = [1; -1]$. This suggests that the unstable mode grows along 45° between δh and δr.

$$\begin{bmatrix}\delta h\\ \delta r\end{bmatrix} = c_1 e^{\lambda_1 t}\boldsymbol{v_1} + c_2 e^{\lambda_2 t}\boldsymbol{v_2} = c_1 e^{\lambda_1 t}\begin{bmatrix}1\\ 1\end{bmatrix} + c_2 e^{\lambda_2 t}\begin{bmatrix}1\\ -1\end{bmatrix} \tag{2.36}$$

$$\frac{\delta h + \delta r}{\Delta r} = e^{\lambda_1 t} \tag{2.37}$$

Given the obtained eigenvector pair, the L1 norm of δh and δr can be useful in isolating the unstable mode in a system. Normalized by the initial condition Δr, the L1 norm is expected to grow exponentially in time from unity, as shown in Equation 2.37. This theoretical basis will then be used to define the growth of leapfrogging instability from LES-ALM.

2.7. Mean-flow kinetic energy flux

In the current study, the wake kinetic entrainment is quantified by the mean-flow kinetic energy flux ϕ_{ij}. The mean-flow kinetic energy flux represents the redistribution or transport of kinetic energy. According to Westerweel et al. (2016), the transport equation for the kinetic energy of the mean flow is derived by taking inner product of the momentum equation with mean velocity $\overline{u}_i$, resulting in Equation 2.38. Note that viscous effects are neglected here, as the macroscopic phenomenon dominates in the mean flow.

$$\frac{D(\overline{u}_i^2)}{Dt} = -\frac{1}{\rho}\overline{u}_i\frac{\partial \overline{p}}{\partial x_i} + \frac{\partial}{\partial x_j}(-\overline{u}_i\overline{u_i'u_j'}) + \overline{u_i'u_j'}\frac{\partial \overline{u}_i}{\partial x_j} \tag{2.38}$$

The left-hand side describes the rate of change of kinetic energy at a point moving at an velocity of $\overline{u}_i$. The first term on the right-hand side is known as the production term, which represents the work done by the mean pressure gradient. The third term is referred to as the deformation term, which is always negative and represents the loss to turbulence. The second term is the product of mean velocity and Reynolds stress. Due to its form of divergence, this term can be interpreted as the flux of mean flow kinetic energy using the divergence theorem by Equation 2.39 and Equation 2.40. Considering the analysis in this study remains in 2D, an enclosed surface is used rather than a volume.

$$\iint_S \frac{\partial}{\partial x_j}(-\overline{u_i}\overline{u_i'u_j'})dS = \oint_C \phi_{ij}\cdot \mathbf{n}_j dl \tag{2.39}$$

where

$$\phi_{ij} = -\overline{u}_i\overline{u_i'u_j'} \tag{2.40}$$

Furthermore, the main terms contributing to the wind turbine wake recovery are the fluxes of kinetic energy relative to the mean axial velocity directed towards the wake centerline (Lignarolo et al., 2015). Given that the analysis is conducted only in the xz plane, the term of interest is $\phi_{xz} = -\overline{u}\overline{u'w'}$ and $\mathbf{n}_j = \mp z$.

2.8. Definition of performance coefficients

In the wind energy field, power and thrust coefficients are important metrics for assessing a wind turbine's overall performance. These coefficients represent the normalized power and thrust, as illustrated by Equation 2.41. According to the well-known Betz's limit, the theoretical maximum power coefficient is approximately 0.593. To date, no wind turbine is capable to exceed the limit. Furthermore, in the simulation, the power is computed by the product of the generated torque and rotational speed since the extracted power is relatively complicated to determine.

$$C_P = \frac{\tau\Omega}{\frac{1}{2}\rho U_\infty^3 A}, \quad C_T = \frac{T}{\frac{1}{2}\rho U_\infty^2 A} \tag{2.41}$$

3

Simulation setup and validation

The chapter documents the LES-ALM settings and followed by the verification and validation of them. At the end of this chapter, the convergence study of the 2D vortex model will be reported.

3.1. Simulation settings

This section presents the simulation settings. The main framework is based on numerical study of Li (2023), with minor modifications to accommodate the specific interest. Yet, for clarity and completeness, the general settings will be fully documented.

3.1.1. Flow properties, tested turbine and operation condition

The tested turbine in the current study takes the 5MW turbine from the National Renewable Energy Laboratory (NREL) as a reference. The NREL 5-MW turbine is a hypothetical HAWT that is not based on a specific real-world turbine. It features a three-bladed rotor with a diameter of 126 meters, mounted on a tower with a hub height of 90 meters. The blade's profile transitions from a cylindrical shape (without lift) at the hub, extending to 14% of the blade length, then shifts to DU (Delft University) and NACA (National Advisory Committee for Aeronautics) airfoils. For comprehensive details on the blade configuration, refer to Jonkman et al. (2009).

A modification was implemented to narrow down the focus of the study specifically on *vortex pairing*. The blade configuration is maintained, but the number of blades has been reduced to two, positioned as opposed to each other. Although this change affects the induction and overall performance due to the deviation from the designed condition, it provides insightful results concerning the study interest. Furthermore, the relevant properties on leapfrogging distance, vortices streamwise distance h, and circulation strength Γ, consequently change. However, controlling these values requires complex iteration. Therefore, as long as these relevant properties are carefully measured and documented, one can ensure the reliability of the modification.

The rotor is set to operate at the rated condition, and no controller is applied for simplicity. The air is considered to be incompressible and Newtonian where Table 3.1

shows the values of the corresponding flow properties and the turbine operating condition. It should be noted that this rate condition is optimized for the unmodified NREL 5MW, and the tip speed ratio is based on the original blade length throughout this work. Besides, the tower, nacelle, tilt angle, precone, thermal effect, and the ground are not considered. This assumption ensures the only asymmetry in the domain is the rotor. While a two-bladed rotor configuration was employed for the investigation of this study, model validation was conducted using the original turbine design. This approach allows for a direct comparison with existing studies, as detailed in Subsection 3.3.3.

Table 3.1: Flow and turbine operational properties

ρ	$1.225\ kg/m^3$
ν	$1.5 \times 10^{-5}\ m^2/s$
U_∞	$11.4\ m/s$
λ	7.0
Re_D	1.0×10^8

3.1.2. Mesh layout

The computational mesh configuration is based on the methodology described by Li (2023) and has been tested for convergence. The use of the actuator line model eliminates the need for boundary layer refinement, allowing the refinement efforts to concentrate on the area surrounding the turbine and its downstream wake region. The semi-structured mesh was generated using the `snappyHexMesh` function in OpenFOAM.

The subsequent two parts detail the mesh configurations for both laminar and turbulent inflow conditions, respectively. The last part in this subsection describes the verification on mesh for LES, done by Li (2023).

Mesh for laminar inflow condition

Figure 3.1 and Figure 3.2 illustrate the mesh layouts for laminar inflow condition. The overall domain dimensions are set to be $12.5D_0 \times 5D_0 \times 5D_0$ by the Cartesian coordinates definition. Within this domain, areas of refined mesh are shaped cylindrically, with diameters set at $3D_0$, $2D_0$, and $1.44D_0$ for different levels.

The rotor is placed at $x/D_0 = 0$ in the streamwise direction and centered in the yz plane. The finest mesh begins $2.5D_0$ upstream and extends to $8D_0$ downstream. A small number of unstructured cells is employed within the domain to ensure a smooth transition between varying levels of refinement. Specifically, the mesh comprises a total of 10.6 million cells, including 10.4 million hexahedrons and 0.2 million polyhedrons. Refinement levels are adjusted approximately by a factor of two at each step. The average cell size corresponding to each level of refinement is reported in Table 3.2, where the cell size at the finest level lies within the range specified by $\Delta/R_0 = [1/30, 1/60]$ from Jha et al. (2014).

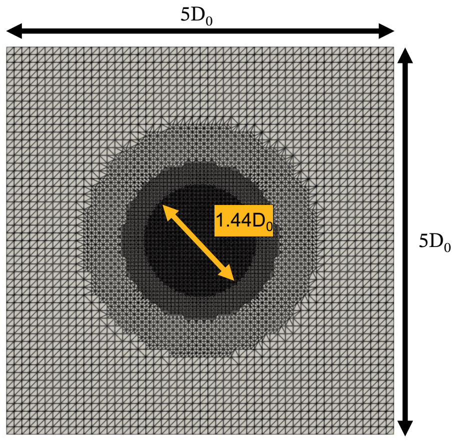

Figure 3.1: Mesh for laminar inflow condition (yz plane)

Refinement	$\overline{\Delta}$
Level1	$D_0/10.0$
Level2	$D_0/19.9$
Level3	$D_0/40.7$
Level4	$D_0/75.8$

Table 3.2: Averaged cell size for laminar inflow condition

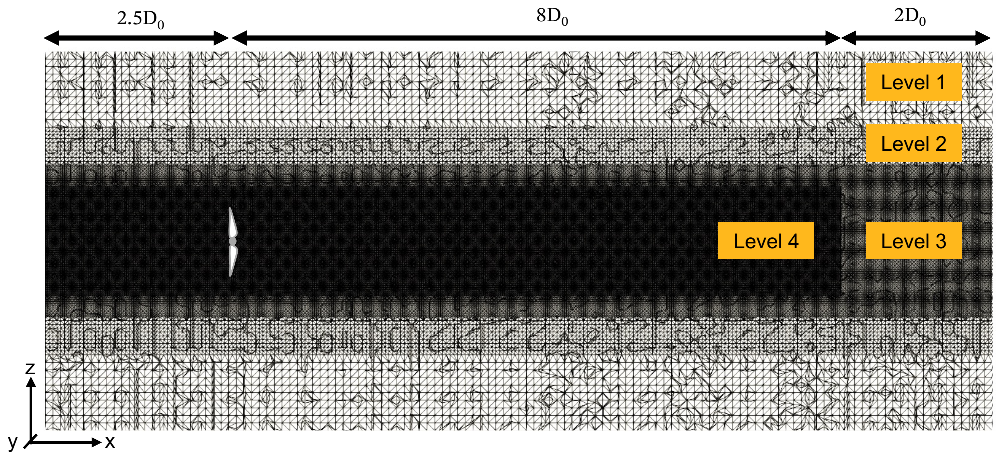

Figure 3.2: Mesh for laminar inflow condition (xz plane)

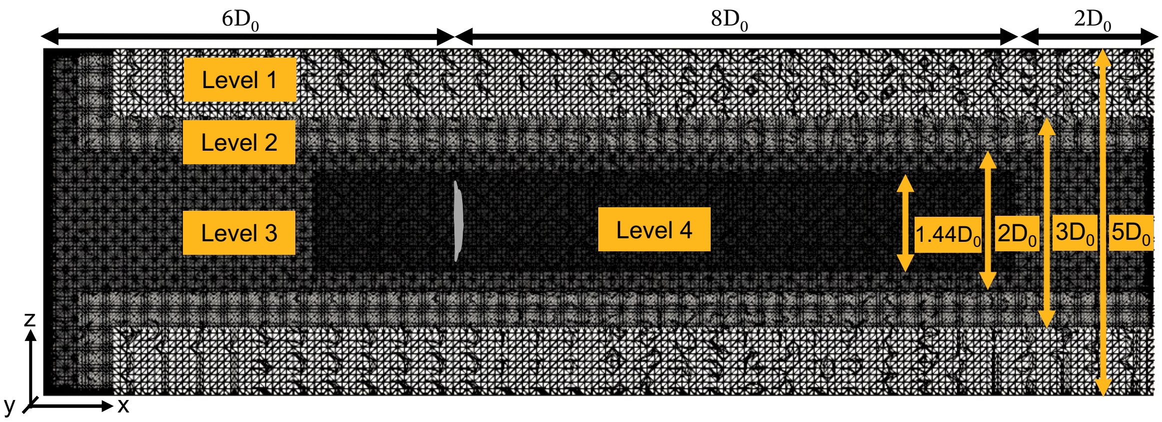

Figure 3.3: Mesh for turbulent inflow conditions (xz plane)

Mesh for turbulent inflow condition

Figure 3.3 shows the adjusted mesh layout used in the turbulent inflow cases. Compared to the setup for the laminar cases, the domain extends to $6D_0$ upstream with a refined region at the inflow. This modification accounts for the development of the flow and helps mitigate undesired pressure fluctuations caused by the synthetic turbulent inlet (Li, 2023). The total mesh comprises 12 million cells, including 11.9 million hexahedrons and 0.18 million polyhedrons. The cell size is similar to the laminar case with $\overline{\Delta} = D_0/70$ in the finest level.

Ratio of resolved turbulent kinetic energy

Both meshes were verified by Li (2023) through the ratio of resolved TKE k_{res}. This paragraph describes the methodology. As introduced in Section 2.1, the LES approach resolves only the Large eddies and models the smaller scales using the subgrid-scale (SGS) model. The grid serves as the filter, at least in this work, meaning that the grid size determines the ratio of resolved to modeled eddies. One widely-used criterion for this ratio is shown in Equation 3.1 (Pope, 2004), which requires that more than 80% of the total turbulence must be resolved. This ratio can only be computed using a precursor case. As shown by Equation 3.2, k_{res} is calculated from the diagonal term of the Reynolds stress tensor, specifically the `uPrime2Mean` in OpenFOAM. Meanwhile, the subgrid-scale TKE, k_{sgs}, can be reconstructed according to Equation 3.3. This is derived from both Equation 2.21 and Equation 2.22.

$$\frac{k_{\mathrm{res}}}{k_{\mathrm{res}} + k_{\mathrm{sgs}}} > 80\% \tag{3.1}$$

$$k_{\mathrm{res}} = 0.5(\overline{u'u'} + \overline{v'v'} + \overline{w'w'}) \tag{3.2}$$

$$k_{\mathrm{sgs}} = (\frac{\nu_{\mathrm{sgs}}}{C_k \Delta})^2 \tag{3.3}$$

The ratio has been found to be larger than the requirement except in regions where the total TKE is close to zero. This indicates that under the current framework, the grid resolution is sufficient to resolve most of the turbulence in the field of interest. Considering that Re_D and the mesh are the same in both studies, the turbulent energy spectrum should be similar. Consequently, no additional verification was conducted in this work; instead, it builds on the findings from Li (2023).

3.1.3. Boundary condition

For the cases with laminar inflow, the boundary conditions are set as follows:

- **Inlet:** A uniform Dirichlet condition was applied to specify the inflow velocity, setting $\boldsymbol{U} = (U_\infty, 0, 0)$.
- **Lateral boundaries:** In the absence of ground, all four lateral boundaries were assigned slip wall conditions, maintaining $\boldsymbol{U} = (U_\infty, 0, 0)$.
- **Outlet:** The convective outflow condition $\frac{D}{Dt} = 0$ was implemented to ensure mass conservation and to avoid disturbance evolving upstream associated with the Neumann condition, as advised by Troldborg (2009).

For the cases with turbulent inflow, the inlet boundary condition is modified. The turbulence is produced by the divergence-free synthetic eddy method (`DFSEM`), developed by Poletto et al. (2013). This method has been modularized in OpenFOAM as `turbulentDFSEMInlet`. The mean velocities are set to be $\boldsymbol{U} = (U_\infty, 0, 0)$, while the turbulence strength was parameterized and obtained through the post-processing approach proposed by Li (2023). The examination of turbulence intensity will be demonstrated in Subsection 3.1.4.

3.1.4. Turbulence inflow properties

To better approximate a realistic scenario, two inflow turbulent intensities have been set around 0.5% and 5% besides the laminar inflow condition.

First, turbulence intensity around 5% is set to represent the typical inflow condition for offshore wind farms (Hansen et al., 2012; Troldborg et al., 2011). Secondly, the lowest turbulence intensity of 0.5% aligns with the wind tunnel experiment settings (<1%) and introduces a minor perturbation, facilitating the breakdown of the wake helix. This setup is informed by the linear stability analysis in J. Sørensen et al. (2015), which defines the near-wake length x_n at which the linear amplification reaches its maximum. Equation 3.4 shows this relationship, depicting the normalized near-wake length where I_∞ denotes the incoming streamwise turbulence intensity. Mathematically, the breakdown of the tip vortex helix is predicted to occur at an infinite distance downstream under laminar inflow conditions ($I_\infty = 0$). Due to the logarithmic characteristics of the process, even a small introduction of turbulence intensity can make the breakdown phenomenon significantly more observable.

$$\frac{x_n}{D_0} = -\frac{1}{2}[\frac{16\overline{u}_c^3}{N_b \lambda C_T U_\infty^3} \ln(0.3 I_\infty) + 5.5 \ln(I_\infty))] \tag{3.4}$$

The turbulent inflow condition was implemented using `DFSEM`, as mentioned in Subsection 3.1.3. Specifically, the same magnitude was imposed on the diagonal terms of the Reynolds stress tensor, while non-diagonal terms were left empty, consistent with the HIT nature of the Smagorinsky model. Although the Reynolds stress tensor enables the deduction of turbulence intensity, grid dissipation tends to diminish the turbulence. Hence, The turbulence intensities are post-measured when the simulation was finished, which will be presented in Subsection 3.3.2.

3.1.5. Actuator line model specification

The actuator line model is implemented using the `TurbineFoam` library within OpenFOAM, as mentioned in Subsection 2.3.2. Following the recommendation of Troldborg (2009), the smoothing parameter is set to be $\epsilon = 2\Delta$. The actuator line is discretized into 40 elements with uniform spacing, ensuring each blade element length Δ_b is slightly smaller than the grid spacing Δ. This is motivated by Martínez-Tossas et al. (2015), who suggests that such configuration allows the spherical projection of body forces to sufficiently overlap, ensuring continuous force distribution along the blade. Additionally, two elements with $C_D = 0.3$ are introduced to model the hub (Li, 2023). Furthermore, the Shen correction is applied to account for the end effect, while the dynamic stall module, tower, and nacelle are not considered.

3.1.6. Temporal discretization, marching scheme, and solver

Generally, the time step is restricted by the spatial discretization in CFD. The metric is the famous Courant–Friedrichs–Lewy (CFL) condition, where the CFL number should not exceed the unity to ensure convergence. However, Troldborg (2009) points out that in the ALM implementations, the maximum permissible time step is determined by the tip speed ratio. This tighter restriction stems from the principle that the displacement of a blade tip should not exceed one grid spacing in each time step. That is, the time step requirement should follow Equation 3.5.

$$\Delta x_{\text{tip}} < \Delta, \quad \Delta x_{\text{tip}} = U_\infty \lambda \Delta t \tag{3.5}$$

Consequently, according to Equation 3.6, the CFL number in this specific scenario should not be greater than 0.14.

$$\text{CFL} = \frac{U_\infty \Delta t}{\Delta} < \frac{1}{\lambda} \tag{3.6}$$

A single time step Δt is set to be 0.013779 seconds, corresponding to the rotor completing a 1-degree rotation. This setup results in a CFL number approximately equal to 0.09.

The time marching, solver, and tolerance are specified as follows. A blending method is employed as the time marching scheme to ensure both accuracy and robustness. This scheme blends the 90% of `Crank-Nicolson` (implicit) and 10% of `Euler` (explicit). At each time step, the Navier Stokes equations are iteratively solved by `pimpleFoam` in OpenFOAM. This application merges the control of PISO (Pressure Implicit with Splitting of Operators) and SIMPLE (Semi-Implicit Method for Pressure Linked Equations) algorithm, and it is designed for the transient and incompressible flow regime. The tolerance is set to be 10^{-6} for both pressure and velocity fields.

3.1.7. Spatial differencing scheme

The selection of the spatial differencing scheme for the convective term influences energy dissipation levels during computation. The energy dissipation primarily arises from the SGS model and numerical diffusion, particularly when the smallest resolvable scales fall within the inertial range where molecular viscosity is not predominant. To minimize numerical diffusion, it should avoid employing pure Upwind Difference Schemes (UDS), which introduce an artificial viscosity despite the higher stability. On the other hand, Central Difference Schemes (CDS) exhibit lower numerical diffusion but suffer from dispersion errors, leading to undesirable oscillations. To strike a balance between preserving wake structures and mitigating numerical oscillations, a blended scheme has been employed (Ivanell et al., 2010; Jha et al., 2014; Troldborg, 2009). The blended scheme was in the end carried out by the `Gauss fixedBlended` in OpenFOAM, and 95% `cubic` and 5% `upwind` were blended.

Figure 3.4 presents the normalized instantaneous vorticity-y field direction with different spacial differencing schemes on the same case. Figure 3.4(a) demonstrates the effects of numerical diffusion when using the `upwind` scheme (1st order UDS). Vortex structures are smeared out making it impossible to distinguish a clear vortex core or the leapfrogging phenomenon. Figure 3.4(b) illustrates the dispersion error using the `linear` scheme (2nd order CDS). Despite the preservation of clear tip vortex structures and the shed vortices, the undesired wiggles emerge between tip vortices. The leapfrogging phenomenon and the merging process can be captured. Figure 3.4(c) shows even more nonphysical oscillation using `cubic` scheme (4th order CDS). Analysis on the vortices behavior is challenging under such condition. Figure 3.4(d) displays the results using blended scheme by cubic and upwind, the vortex edges are maintained and wiggles are removed, despite the greater diffusion of shed vortices. Moreover, Figure 3.4(e) and (f) apply the `linearUpwind` scheme (2nd order); the pure version produces clean results but with more diffusion than Figure 3.4(d), while the blended version does not entirely eliminate oscillations at the current blending ratio.

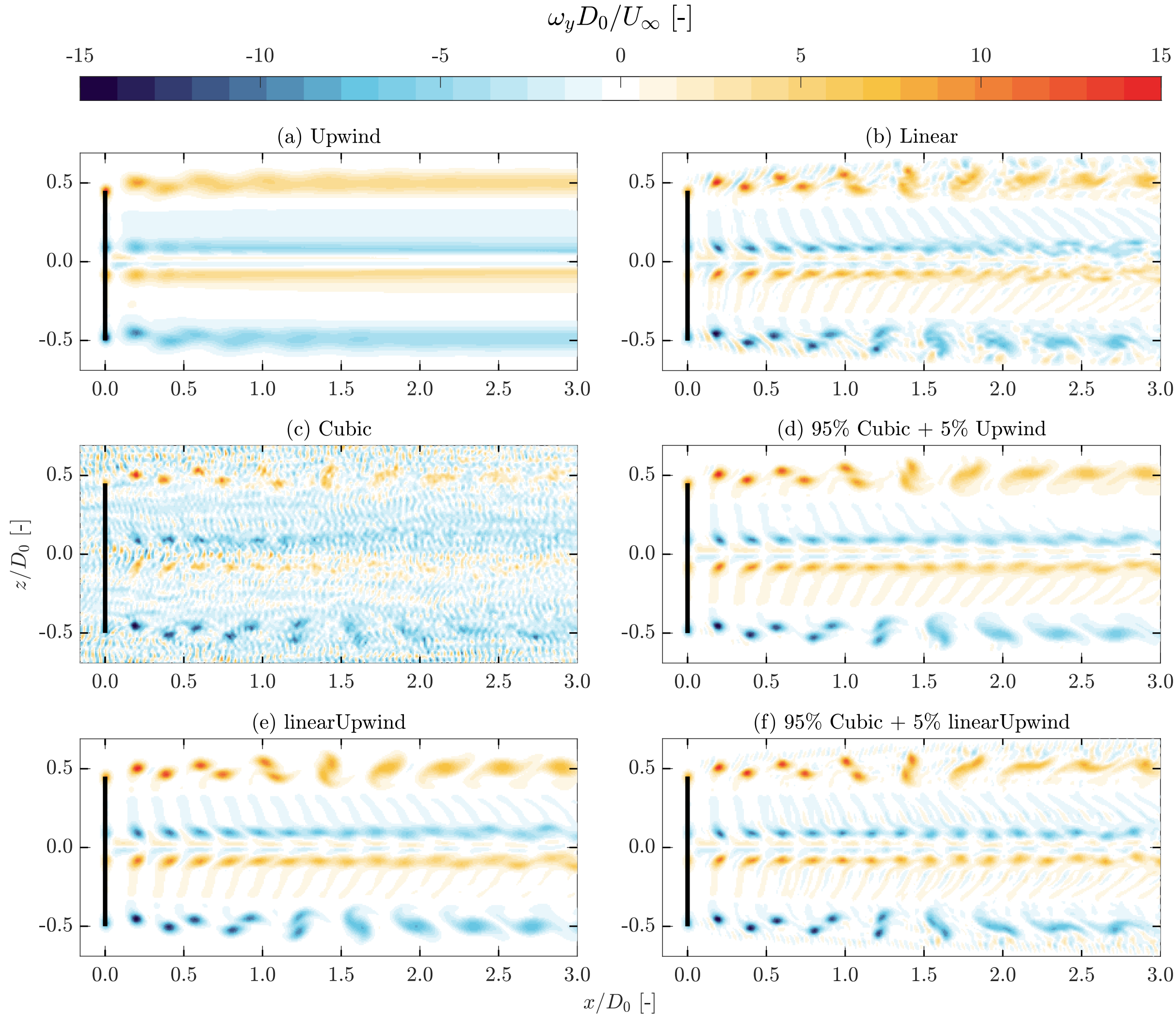

Figure 3.4: Normalized instantaneous vorticity-y field with different spatial schemes

Regarding turbine performance and computational cost, the differences among various spatial schemes are negligible. Figure 3.5 illustrates the C_L distribution along the truncated blade. The upwind scheme shows a slight deviation from others at approximately $r/R_{\Delta r} = 0.4$. However, these deviations near the tip and root are smaller due to the mitigation by end-effect correction. Considering that the CPU hours vary within 0.1% across with different schemes and that the RAM of 6GB multiplied by 96 cores is more than sufficient for all scenarios, the blended scheme with cubic and upwind was selected for higher-order accuracy.

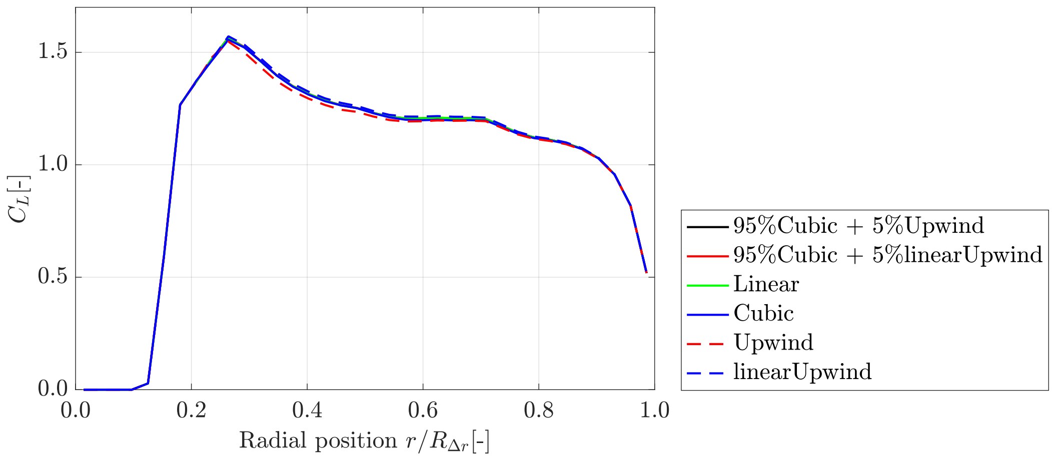

Figure 3.5: C_L along the radial position with different spatial schemes

3.2. Test matrix

Table 3.3: Overview of Cases with Different BLD and TI Levels

$\Delta r/R_0$ [%]	TI [%]		
	Laminar	0.5	5
0	baseline	case10	case13
2.5	case1	-	-
5	case2	-	-
7.5	case3	-	-
10	case4	case11	case14
12.2	case5	-	-
14.6	case6	-	-
17.1	case7	-	-
19.5	case8	case12	case15
29.3	case9	-	-

Table 3.3 presents the test matrix for the current study. Initially, the effect of blade length difference is studied under laminar conditions to isolate the impact of rotor asymmetry. Additionally, minimal and atmospheric boundary layer level turbulence intensities are applied to the inflow for two $\Delta r/R_0$ cases. These cases were chosen to align

with the settings of ongoing wind tunnel experiments. Consequently, 16 simulations were conducted, including the baseline case and the benchmarking case discussed in Subsection 3.3.3, were performed.

3.3. Validation and verification of LES-ALM settings

This section presents the validation and verification. As mentioned in Subsection 3.1.2, convergence tests on the grid and ratio of resolved TKE have been done by Li (2023). Considering the Reynolds number and flow regime in both works are similar, no additional test on the grid was made specifically. Instead, the convergence test on time steps is performed in Subsection 3.3.1. Then, the turbine performance is benchmarked to prior work in Subsection 3.3.3. Lastly, Subsection 3.3.4 validates the newly introduced parameter, effective diameter D_e, by performances.

3.3.1. Convergence test on time steps

A convergence test on the time step was conducted to determine the optimal averaging period necessary for accurate data analysis. The focus of this test was the properties of the flow at the plane of $8D_0$ downstream of the turbine, denoted as $x/D_0 = 8$. This location was chosen because it is located at the end of the most refined mesh region. In other words, this test establishes confidence in using the data until this plane. The test varied the start time, beginning from the 30th revolution and extending to the 90th while maintaining a constant averaging length of 60 revolutions. This setup involves a time series profile with 21,600 steps. Given that the helical pitch $h' \approx 0.4D_0$, this averaging length captures the flow in the tip region as it convects from the turbine to $x/D_0 = 8$ plane three times.

Figure 3.6a and Figure 3.6b display the streamwise disk-averaged mean velocities and the distribution of these velocities at $x/D_0 = 8$ across different averaging periods. Streamwise mean velocity $\overline{u}$, especially in the tip and root regions, tends to converge to lower values as the averaging period progresses, as observed in both plots. In the end, the averaging period was chosen to span from 60th to 120th revolutions. The determining metric for evaluating wake recovery, $< \overline{u} >_{\text{disk}}$, shows a deviation of $\pm$ 0.0001m/s from the converging value, which is equivalent to 0.03% relative to the velocity difference across the wake boundary layer. The simulation was consequently set to run for 120 revolutions, which corresponds to approximately 600 seconds based on the tip speed ratio. They were performed on DelftBlue (DHPC, 2022), the high-performance computing cluster at TU Delft, for 4900 CPU hours with 96 cores in each case.

3.3.2. Turbulence intensity measurement

As mentioned in Subsection 3.1.4, turbulence intensity is measured post-process. This measurement is conducted using probes distribution in Li (2023), illustrated in Figure 3.7. Equation 3.7 shows the determination of the turbulent intensity where N_{probe} denotes the number of probes. With time-resolved data, the turbulence intensity can be calculated by finding the standard deviations of velocities in the three directions for each probe. The overall turbulence intensity is then obtained by averaging the turbulence intensity values from all the probes.

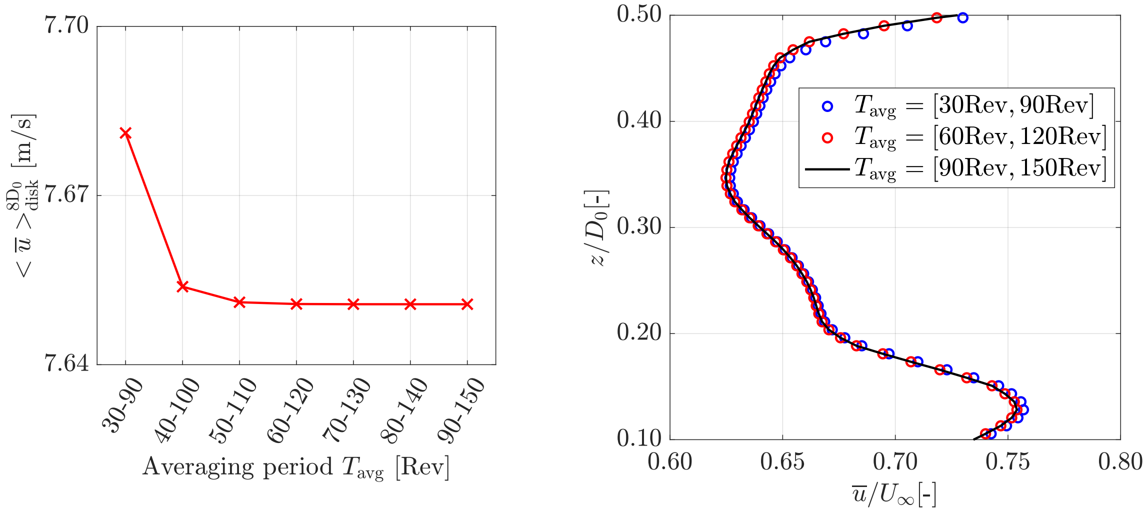

(a) Disk-averaged $\overline{u}$ at $x/D_0 = 8$

(b) Radial profile of normalized $\overline{u}$ at $x/D_0 = 8$

Figure 3.6: Comparison of streamwise mean velocity across averaging periods

$$\text{TI} = \frac{\sum_{i=1}^{N_{\text{probe}}} \sqrt{\frac{1}{3}(\sigma_{u,i}^2 + \sigma_{v,i}^2 + \sigma_{w,i}^2)}}{N_{\text{probe}} \cdot U_\infty} \times 100\% \tag{3.7}$$

Furthermore, given that the eddies are only introduced at the inlet boundary where $x/D_0 = -6$ the turbulence level is expected to decrease as they travel downstream due to grid dissipation. To record the decay of turbulence intensity, measurements were taken at four streamwise locations: $x/D_0 = [-2, 0, 2, 4]$.

Figure 3.8 displays the measurement results for three different settings aimed at creating flows with initial TIs of approximately 10%, 5%, and 0.5% for settings A, B, and C, respectively. It is evident that as the flow progresses downstream, there is a notable variation in TI. Specifically, setting A shows a significant decrease in TI, dropping from approximately 10.5% to 6.5% as it moves from $x/D_0 = -2$ to $x/D_0 = 4$. On the other hand, setting B exhibits a moderate decrease of about 1%, and setting C remains relatively constant, demonstrating a trivial change in TI. Considering that this interval is relevant to wake development and of interest, the variation in setting A is too high, deviating from the homogeneous assumption in Smagorinsky's model. Therefore, settings B and C were ultimately chosen as the turbulence inflow settings for this study.

Two important points need to be noted. First, the fact that `DFSEM` uses the same seed every run ensures the consistency of the synthesized eddies. This repeatability enhances the validation of the turbulence intensity. Second, no turbines are placed in the domain for these tests, allowing the measurement of turbulence intensity to reflect only the inflow conditions.

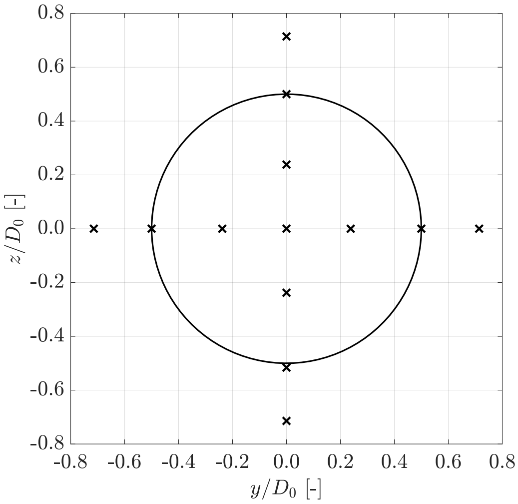

Figure 3.7: Positions of the probes characterizing inflow properties from Li (2023)

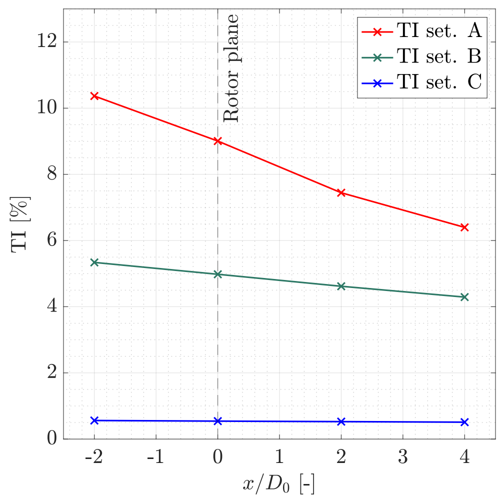

Figure 3.8: Turbulence intensities at streamwise locations

3.3.3. Turbine performance validation

In this subsection, the computed turbine performance is benchmarked against existing literature. It is important to note that there is no experimental or field data available for performance assessment since the NREL 5MW turbine has not been manufactured. Therefore, the power and thrust coefficients at the rated condition were compared with those from other numerical simulations. Note that the actual test cases involve off-design conditions with variations in blade configuration, while the rated condition with the original design serves as a basis for validating the simulation settings.

Table 3.4 provides a comparison of the computed results alongside those from other studies. The results from this study fall within the range of those obtained in recent studies, despite showing some deviations from the originally designed document (Jonkman et al., 2009). Apart from that, two observations have been made. First, the turbulence intensity in the inflow does not significantly affect performance under the same spatial and temporal discretization. Furthermore, the simulation settings in the current study are similar to those used by Li (2023), except for the spatial differencing scheme employed for the convection term. However, the overall turbine performances were similar, suggesting that the spatial discretization scheme is not a determining factor in turbine performance under current settings.

3.3.4. Effective turbine performance

As introduced in Subsection 2.4.2, the effective diameter is designed to normalize rotor size by its performance; however, it is defined by area for simplicity. Hence, the effective diameter is required to be validated against the effective performance. The effective performance is based on the effective diameter, shown by Equation 3.8.

$$C_{P,e} = \frac{\tau\Omega}{\frac{1}{2}\rho U_\infty^3 A_e}, \quad C_{T,e} = \frac{T}{\frac{1}{2}\rho U_\infty^2 A_e} \tag{3.8}$$

Table 3.4: Comparison on NREL 5MW turbine rated performance with literature

Work	Models	Inflow TI [%]	$\overline{C}_T$	$\overline{C}_P$
Current Work	**LES-ALM**	**Laminar**	**0.730**	**0.514**
Current Work	**LES-ALM**	**5.3**	**0.727**	**0.513**
Li (2023)	LES-ALM	Laminar	0.72	0.51
Li (2023)	LES-ALM	5.3	0.73	0.52
Xu et al. (2023)	LES-ALM	4.7	0.83	0.41
Xue et al. (2022)	LES-ALM	Laminar	0.80	0.47
Lin et al. (2023)	RANS	Laminar	0.74	0.48
Tang and Cao (2023)	RANS	5	-	0.50
Rezaeiha and Micallef (2021)	RANS-ADM	5	0.71	0.57
Jonkman et al. (2009)	FAST	-	0.81	0.47

Table 3.5 presents the effective diameter and performance for various blade length differences in a 2-bladed NREL 5MW turbine, operating under laminar inflow conditions with $U_\infty = 11.4m/s$ and $\lambda = 7$. An evident decrease in performance is observed as the blade length difference increases, which aligns with expectations: a greater blade length difference results in a smaller effective rotor size relative to the baseline. Moreover, despite these variations, the effective thrust and power coefficients closely match those of the baseline configuration. This suggests that the effective diameter, even though defined by the averaged area, successfully captures the normalization of performance.

Table 3.5: (Effective) performance with blade length differences

$\Delta r/R_0[\%]$	D_e/D_0	Performance		Effective Performance	
		C_T	C_P	$C_{T,e}$	$C_{P,e}$
0.0	1.00	0.543	0.426	0.543	0.426
2.5	0.99	0.532	0.417	0.546	0.427
5.0	0.98	0.520	0.407	0.546	0.427
7.5	0.96	0.508	0.397	0.546	0.427
10	0.95	0.494	0.387	0.545	0.427
12.2	0.94	0.482	0.377	0.544	0.426
14.6	0.93	0.470	0.368	0.544	0.426
17.1	0.92	0.458	0.360	0.543	0.425
19.5	0.91	0.447	0.351	0.543	0.426
29.3	0.87	0.405	0.321	0.540	0.428

3.4. Convergence study on 2D vortex model

Subsection 2.6.1 introduces a 2D point vortex model to predict the vortex pairing motion. This section will present a convergence study on the variables required for setting up the model. Subsection 3.4.1 shows the influence of N_p, while Subsection 3.4.2 discusses the validity of system linearization.

3.4.1. Number of inducing vortex pairs N_p

This subsection presents a convergence study on N_p for the growth rate. Ideally, the vortex row would be infinite; however, this is impractical for implementation and would consume unnecessary computational resources. Given that the induction velocity is inversely proportional to distance, the influence of vortices located infinitely far from the ith vortex is negligible. Therefore, this convergence study aims to determine the sufficient number of inducing vortex pairs that should be periodically added on both sides of the ith vortex for accurate modeling.

In this analysis, the first mode normalized eigenvalue λ_1^* from Equation 2.36 is taken as the growth rate. Figure 3.9 shows the dependence of the λ_1^* on N_p with an small initial radial perturbation. As expected, the growth rate converges to $\pi/2$ as N_p increases, reaching 99.9% of $\pi/2$ for $N_p = 52$. Consequently, 52 pairs of inducing vortex pairs are chosen for the following studies.

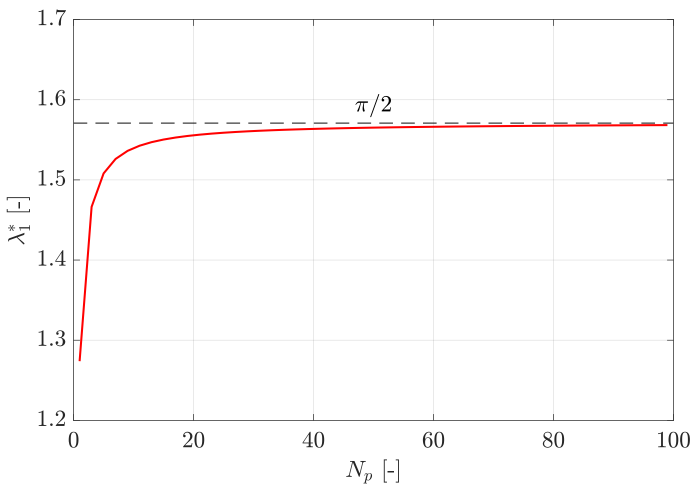

Figure 3.9: Convergence of growth rate from 2D model on N_p

3.4.2. Validity of linearization

As discussed in Section 2.6, the linearized model is not applicable with a large $\Delta r/R_0$ due to deviation from the equilibrium point. Therefore, an alternative approach involves performing numerical integration on the nonlinear system (Equation 2.34). In specific, the system is integrated using `ode45` function in MATLAB®, which employs the explicit Runge-Kutta (4,5) method. As predicted by Equation 2.37, the L1 norm of δh and δr is expected to grow exponentially. This exponential growth is evident from the linear region in Figure 3.10b, which demonstrates an example of the L1 norm and its components on a semi-log scale versus the normalized time t^*. The slope of its linear region determines the growth rate, denoted as $\sigma_{2\mathrm{D}}^*$. Furthermore, the integrated results also predict the leapfrogging time when $\delta h = h_0$, indicated by the dashed lines.

Figure 3.11 compares the normalized growth rates against blade length difference. The normalized eigenvalues from the linearized model are denoted by λ_1^*, while the slopes derived from the L1 norm of the nonlinear system are marked as $\sigma_{2\mathrm{D}}^*$. In the region

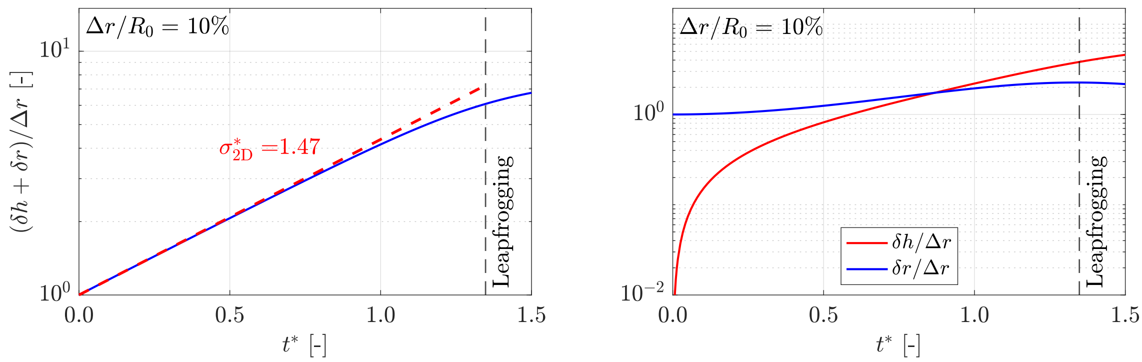

(a) Normalizsed L1 norm

(b) Streamwise and radial components

Figure 3.10: Result from numerical integration of the nonlinear Equation 2.34 in an example of $\Delta r/R_0 = 2.5\%$

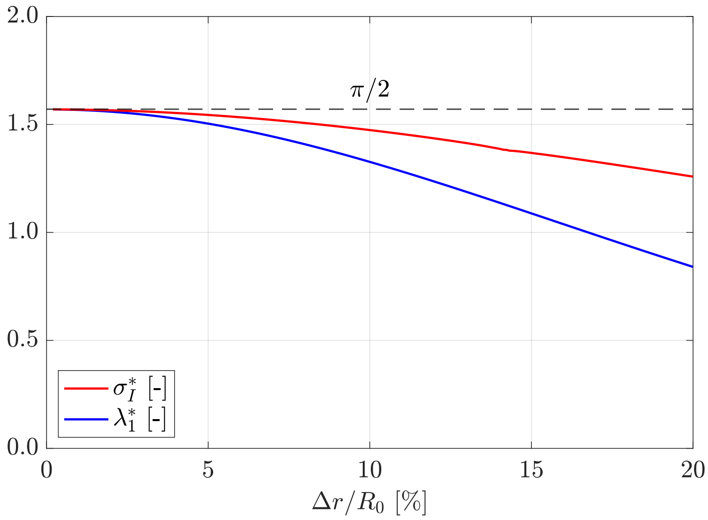

Figure 3.11: Growth rates from the linearized (Equation 2.36) and nonlinear (Equation 2.34) model

where $\Delta r/R_0$ close to zero, the values of λ^*_1 and σ^*_{2D} coincide. On the other hand, λ^*_1 and σ^*_{2D} decrease with increasing $\Delta r/R_0$, with λ^*_1 diverging from σ^*_{2D}. This observation aligns with the discussion in the previous paragraph, which notes that linearization is only valid in regions with small perturbations around the equilibrium point. In the current study, $\Delta r/R_0$ reaches up to 30%, and given that such a large $\Delta r/R_0$ results in deviations between σ^*_{2D} and λ^*_1 exceeding 30%. Hence, only σ^*_{2D} will be employed in Chapter 4 to compare with the LES-ALM results.

4

Results: Tip vortex behaviors

This chapter presents results extracted from LES-ALM regarding the first research question: the impact of rotor asymmetry on tip vortex behaviors. The main focus is on the blade length difference-triggered leapfrogging phenomenon and the influence of turbulence intensity. Section 4.1 and Section 4.2 provide overviews of tip vortex behaviors with varying degrees of rotor asymmetry under different inflow conditions. Section 4.3 presents the measured vortex trajectories and dives into a deeper analysis. Additionally, Section 4.4 quantifies the growth rates of leapfrogging instability using a methodology derived from the 2D vortex model. Lastly, Section 4.5 compares the leapfrogging distance and time across different cases, as well as with the 2D vortex model and wind tunnel experiments.

Note that the analysis in this chapter remains in the 2D xz plane based on two reasons. Firstly, the vortex cores are relatively small compared to the curvature of the helix, as demonstrated in Subsection 4.3.1. Secondly, due to helical geometry and symmetry of the simulation settings, the time variation of vortices in the streamwise direction is equivalent to their spatial evolution in the azimuthal direction.

4.1. Overview of tip vortex behavior - laminar inflow

Figure 4.1 and Figure 4.2 show the instantaneous vorticity and velocity fields, respectively, for $\Delta r/R_0 = [0\%, 2.5\%, 10\%, 30\%]$ under laminar inflow conditions. These instantaneous fields were taken from the last time step of the simulation. They are normalized by the bulk length and velocity scales, which are the effective diameter and inflow wind speed. The black line in these figures, and in other field plots in this report, represents the rotor.

In all cases, vortices released from the blade tips, hubs, and shed vortices can be observed. For the baseline case, the tip vortices at the upper and lower tips are symmetric in terms of strength and location. As for the cases with an asymmetric rotor, tip vortices are released with a radial offset alternately due to blade length difference. Additionally, as the vortices convect downstream, the local maximum of vorticity, which represents the vortex cores, appears to be diffused.

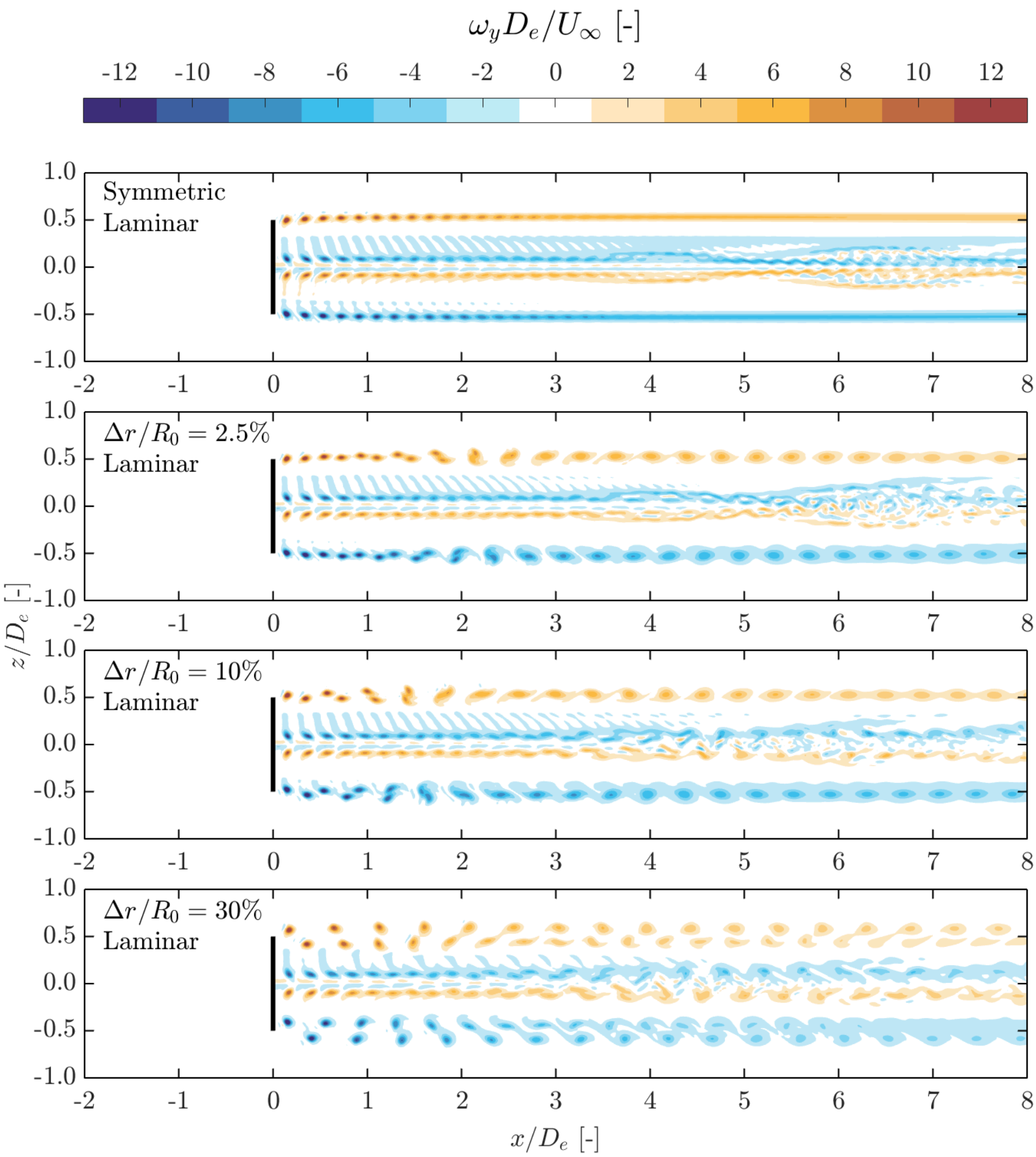

Figure 4.1: Instantaneous vorticity field-y with different $\Delta r/R_0$ under laminar inflow condition

In the baseline case, the tip vortices are released and then march downstream stably. Around $x/D_e = 4$, the independent vortex becomes indistinct under the current colormap arrangement. Furthermore, as described by Equation 3.4, the tip vortex helix is expected to break down infinitely downstream due to the laminar inflow condition.

When asymmetry is introduced to the rotor, it triggers the leapfrogging instability. With a slight (2.5%) radial offset of the tip vortex, the vortex can be observed to pair up and roll up with each other around $x/D_e = 1$. As expected according to vorticity direction

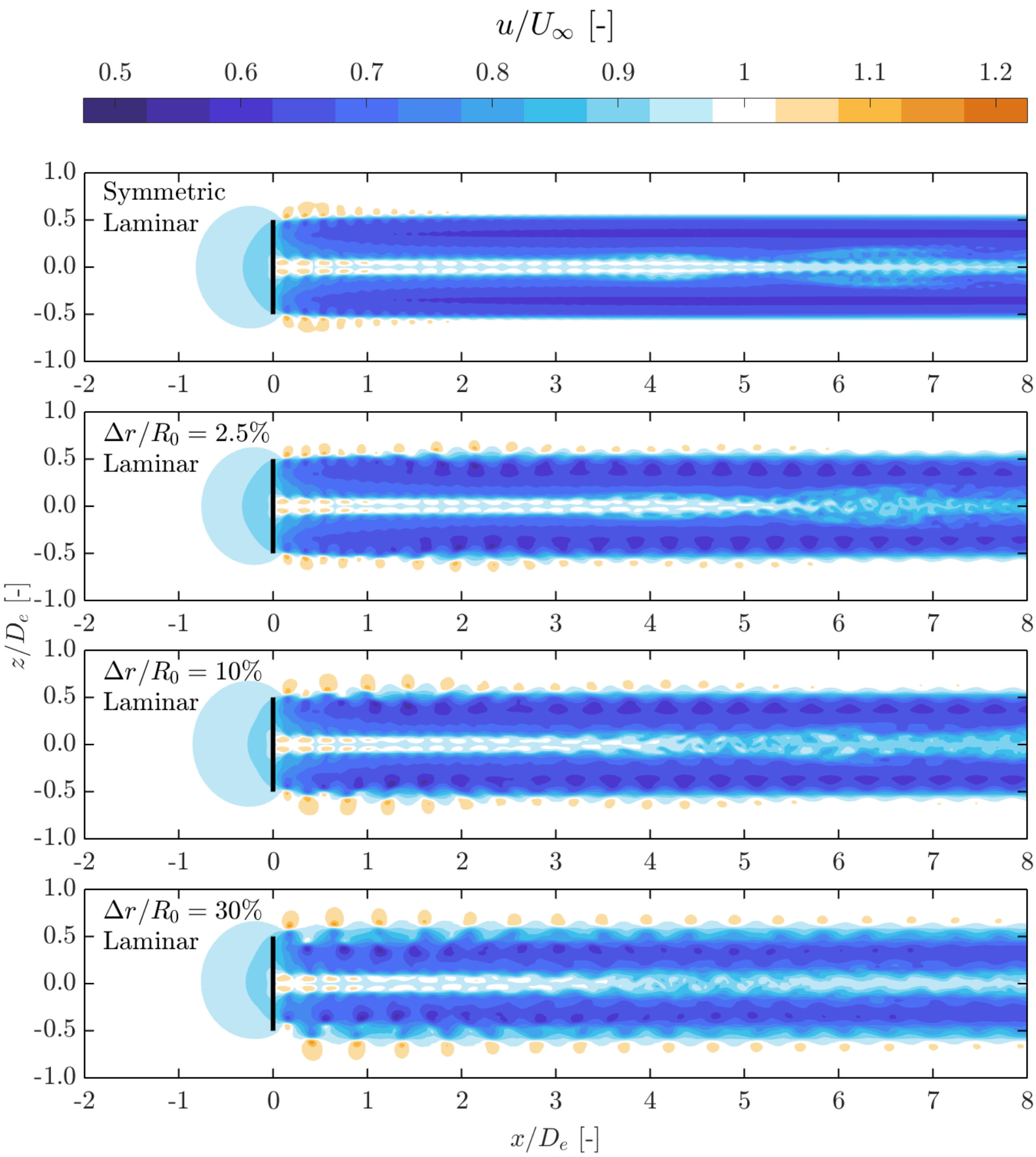

Figure 4.2: Instantaneous streamwise velocity with different $\Delta r/R_0$ under laminar inflow condition

and the Biot Savart law, outer vortices travel faster than inner ones. Then, around $x/D_e = 2$, outer vortices surpass inner ones, swapping their streamwise locations. This point defines the leapfrogging distance as mentioned in Section 2.5.

When the blade length difference increases to $\Delta r/R_0 = 10\%$, the pairing motion occurs earlier, with the leapfrogging event taking place around $x/D_e = 1.5$. The merging event also occurs sooner compared to the case with a smaller blade length difference.

With a blade length difference of up to 30%, the vortices do not pair up due to the larger separation distance between them and significant convective velocity. This pronounced velocity difference is evident between the heights where the two array vortices are released ($z/D_e = 0.35$ and 0.5) in Figure 4.2. Consequently, the outer and inner vortices travel at different speeds, as if they are on two separate lanes of a highway. Although the surpassing motion of the vortices can still be observed, it is predominantly driven by velocity shear rather than mutual induction.

Overall, the mutual inductance instability triggered by the blade length difference appears to be a local event despite the initial interaction between them. As mentioned above, the tip vortex pair merges into a large vortex. These larger vortices convect downstream stably with a separation distance approximately twice the initial one. Due to the laminarity of the flow, no external disturbance disrupts this vortex street. Consequently, no tip vortex breakdown can be observed in the current field of view.

4.2. Overview of tip vortex behavior - turbulent inflow

Figure 4.3 and Figure 4.4 show the instantaneous vorticity and velocity fields, respectively, for $\Delta r/R_0 = [0\%, 10\%]$ under turbulent inflow conditions. The most notable difference compared to laminar inflow conditions is the breakdown of the tip vortex helix. This breakdown is observable at both low and high inflow turbulence intensities (0.5% and 5%), regardless of whether a symmetric or asymmetric rotor is used.

As shown in Figure 4.3, a similar pairing pattern to that observed under laminar conditions can be seen at a 0.5% inflow TI. However, due to ambient turbulence, some vortices experience slight displacement, causing instability to grow significantly around $x/D_0 = 4$. Hence, the helical structure breaks into a smaller turbulence structure. This, again, can be qualitatively explained by Equation 3.4. Particularly with the asymmetric rotor, mutual inductance still drives the leapfrogging phenomenon followed by vortex merging, as in the laminar case. However, the merged vortex appears to pair up and undergo a secondary leapfrogging event.

With an atmospheric boundary layer turbulence intensity of 5%, the vorticity field exhibits increased noise. Higher vorticity levels can be spotted upstream of the rotor. The tip vortex core becomes less distinct, obscured by smaller structures within the wake. Furthermore, the resemblance of pattern upstream in cases with a TI of 5% demonstrates that `DFSEM` uses the same seed to synthesize turbulence.

Evidence of helix breakdown is also apparent in Figure 4.4, where the wavy structures indicate that the deficit streamtube behind the wind turbine is no longer confined by the tip vortex helix. Notably, there is a difference between the two TIs; with a higher TI, the helix breaks down earlier.

Last but not least, while the rotor configuration influences the near-wake tip vortex behavior, the overall wake structure remains governed by the turbulence intensity. This is evident from both the velocity and vorticity fields. Hence, one can deduce that although the intended disturbance caused by blade length differences triggers leapfrogging instability, its effect on wake recovery can be overshadowed by inflow turbulence. To further

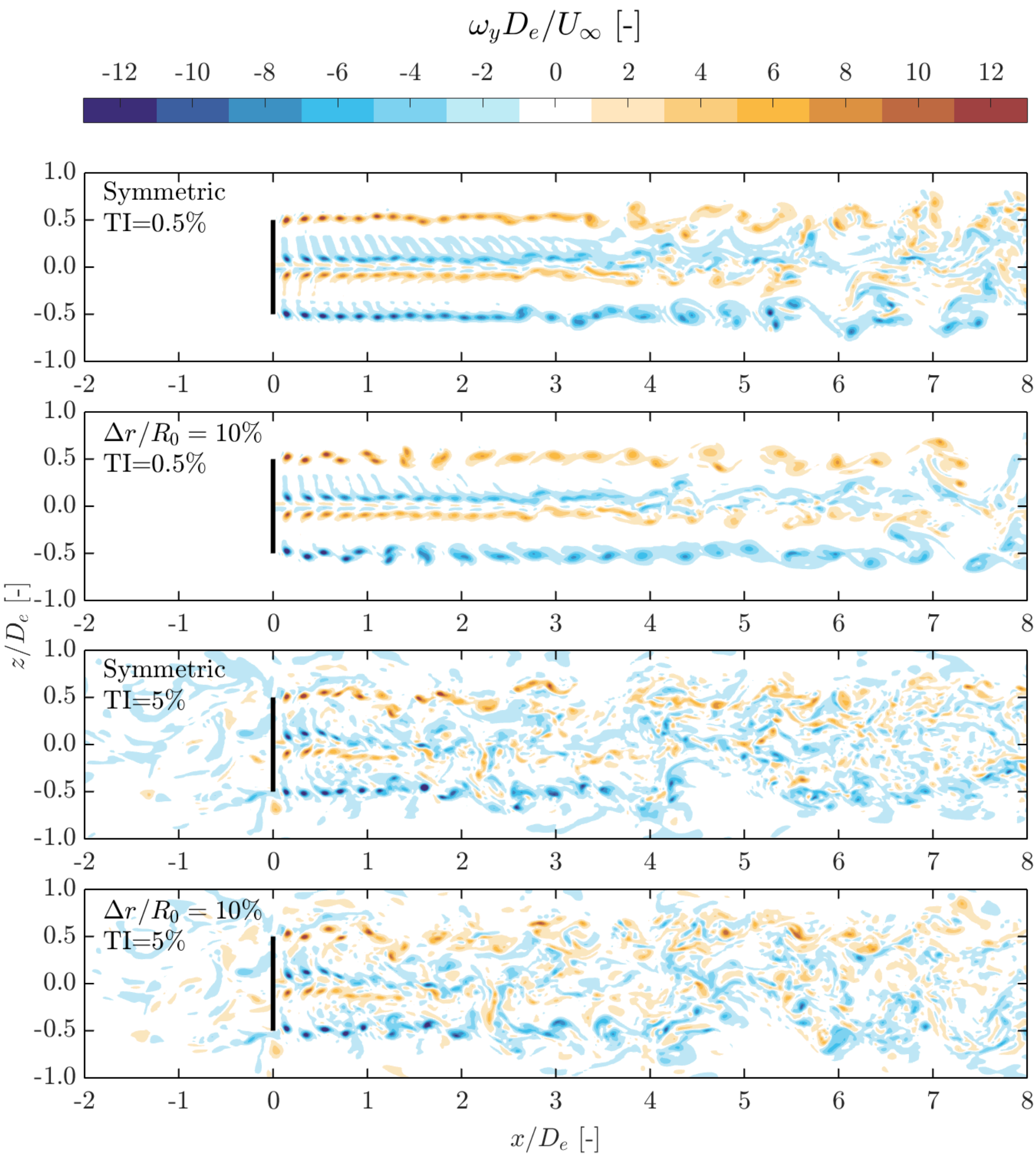

Figure 4.3: Instantaneous vorticity field-y with different $\Delta r/R_0$ under turbulent inflow condition

verify this, the subsequent sections of this chapter will focus on tip vortex behavior, and the wake recovery in both inflow conditions will be explored in the next chapter.

4.3. Vortex pair evolution

The leapfrogging phenomenon describes the pairing motion of vortices. Therefore, the vortex pair is considered a fundamental unit for studying the growth of this instability. As illustrated in Figure 4.5, vortices are identified by the local maxima of vorticity

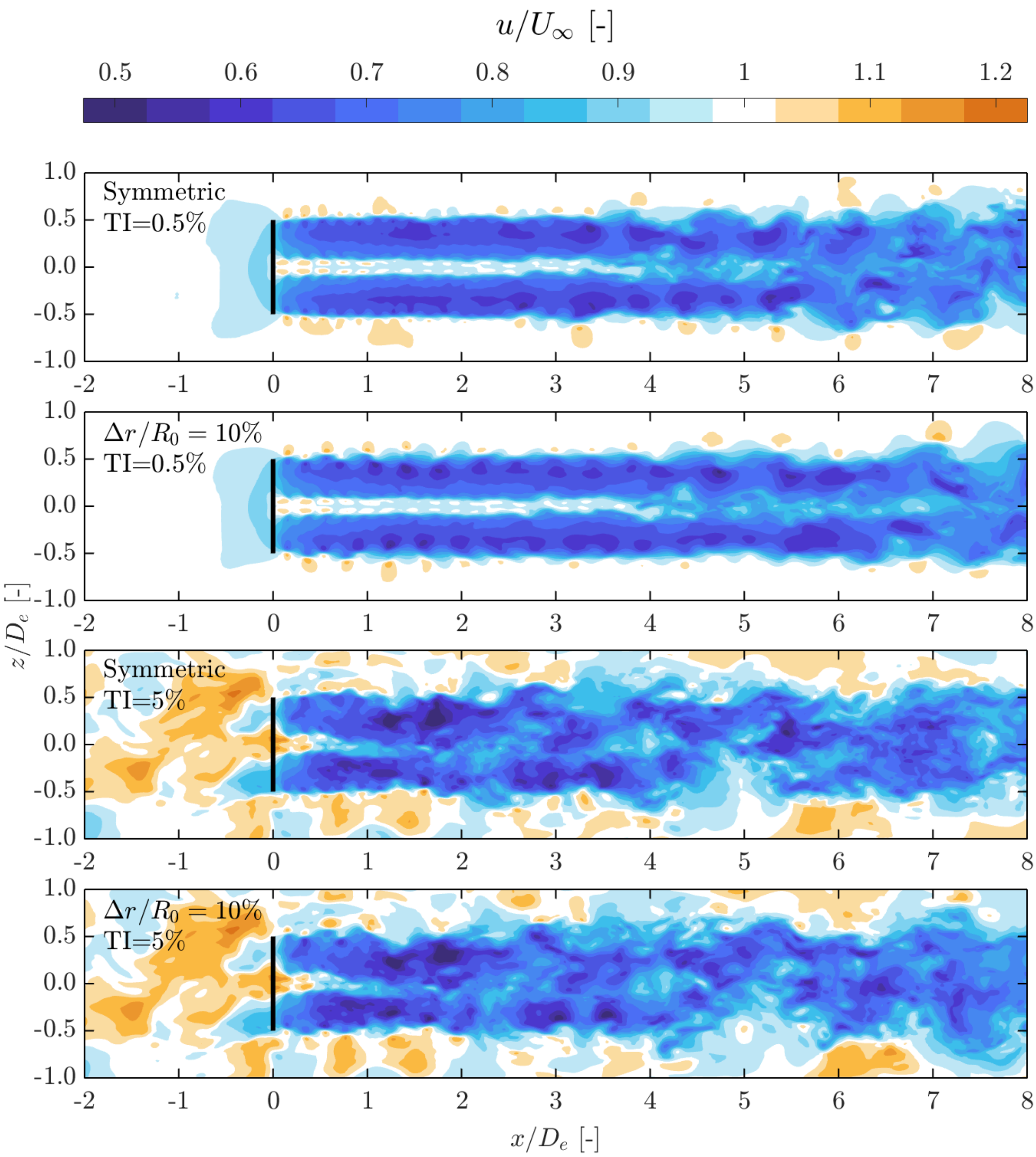

Figure 4.4: Instantaneous streamwise velocity with different $\Delta r/R_0$ under turbulent inflow conditions

(Troldborg, 2009). Measurements of their initial properties, including circulation and core size, are documented in Subsection 4.3.1. Subsequently, Subsection 4.3.3 introduces the method used to trace the vortex pairs and analyzes the evolution of their relative positions. Lastly, Subsection 4.3.3 discusses the influence of convective velocity shear on the tip vortex pair evolution.

For clarity, unless otherwise specified, the plots and data presented in this section are based on the case with laminar inflow conditions. Besides, the behavior of vortex pairs is a local phenomenon with minimal impact on overall rotor performance. Therefore, the original rotor diameter is used for normalization in this and the following two sections, rather than the effective diameter.

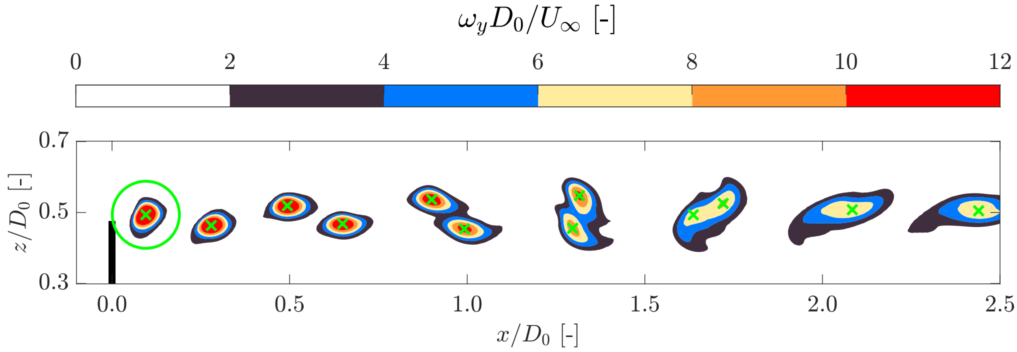

Figure 4.5: Identification of vortices in an example of $\Delta r/R_0 = 10\%$. Green crosses mark the vortex core locations, and the green circle shows the integral surface for circulation calculation.

4.3.1. Initial vortex properties and circulation strength

Table 4.1: Initial vortex properties

a_{v0} from R_0	$(4.80 \pm 0.02)\ m$
a_{v0} from $R_{\Delta r}$	$(4.83 \pm 0.05)\ m$
Γ_0 from R_0	$(100.48 \pm 0.98)\ m^2/s$
Γ_0 from $R_{\Delta r}$	$(99.46 \pm 0.44)\ m^2/s$
h_0	$23.80\ m$
h_0/D_0	0.1889
a_{v0}/h_0	0.20
Re_D	4.8×10^7
Re_Γ	6.7×10^6

The properties of the initial vortex are detailed in this subsection. The motivations for examining these properties include the following: Firstly, the relevant length and time scale of the leapfrogging phenomenon are h and $2h^2/\Gamma$. Measurement of these properties is necessary for normalization of growth rates. Second, the blade length differences are generated by blade truncation as mentioned in Subsection 2.4.1. Data from the initial tip vortex serves to confirm this method. The analysis reveals that the properties of tip vortices from both the original and truncated blades vary by less than 1%.

$$\Gamma = \int_S \omega_y dS \tag{4.1}$$

$$a_v^2 = \frac{1}{\Gamma}\int_S |\boldsymbol{X} - \boldsymbol{X^c}|^2 \omega dS \quad \text{and} \quad \boldsymbol{X^c} = \frac{1}{\Gamma}\int_S \boldsymbol{X}\omega dS \tag{4.2}$$

Table 4.1 presents the properties measured from the initial vortex, including the vortex core radius a_v, streamwise vortex separation distance h_0, and circulation strength Γ, where the subscript 0 denotes the initial vortex. Firstly, the circulation of the tip vortex is computed using the surface integral of the vorticity, as depicted in Equation 4.1. The circular integration surface is centered at the vortex center, with a diameter of h_0, following Quaranta et al. (2019). This selection prevents the overlap of another integral surface, as illustrated in Figure 4.5. Secondly, Equation 4.2 details the calculation of the vortex core radius, which is defined by the second-order moment of vorticity (Leweke et al., 2016). Third, the streamwise vortex separation distance was measured by the helical pitch h' divided by N_b. Additionally, it is important to note that the initial vortex is identified as the earliest vortex whose integral surface does not overlap with $x = 0$.

Figure 4.6a and Figure 4.6b show the initial vortex core radius and circulation with different $\Delta r/R_0$. Both plots suggest that these properties remain relatively constant, within 1%, regardless of $\Delta r/R_0$ or the blades from which they are shed.

The initial core radius is approximately $4.8m$ for all cases. The core size lies in a range that does not affect the stability of multiple-helix configurations as noted by Gupta and Loewy (1974). Besides, this information reinforces the assumption that leapfrogging phenomena can primarily be understood as a 2D process. The core radius accounts for a small ratio, about 8%, of curvature of the helix. In terms of induction, the tip vortex is treated as a straight vortex filament interaction, where the induced velocity is mainly determined by neighboring vortices rather than from those on the opposite side of the rotor axis.

The initial circulation remains at around $100m^2/s$ for all cases. This consistency, along with the uniform core size, indicates that the methodology of creating blade length differences through blade truncation does not impact the properties of the individual shed tip vortices. Furthermore, the helical pitch $h' = N_b h_0$, which is determined mainly by λ (Equation 1.1), remains constant. Consequently, the relevant time scale is set as $\Gamma_0/2h_0^2$ for across all scenarios.

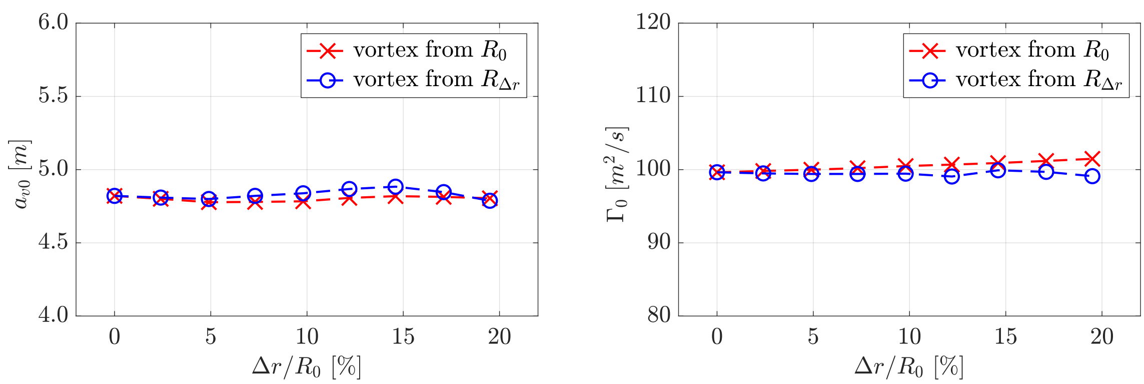

(a) Vortex core radius a_{v0} **(b)** Circulation Γ_0

Figure 4.6: Initial vortex properties with different $\Delta r/R_0$

The evolution of circulation along the streamwise direction is measured in the baseline case in Figure 4.7., providing supporting evidence for the third assumption of the 2D vortex model. Additionally, to compare the stable convection of tip vortices in the baseline case with the merged vortices from asymmetric rotor cases under laminar inflow conditions, the circulations of merged vortex Γ_{Merg}, from $\Delta r/R_0 = 10\%$ are also documented. Note that the integral surface is twice when calculating Γ_{Merg} than Γ. Both arrays demonstrate constant circulation, indicating the conservation of vortex strength within the selected integral surface. Besides, Γ_{Merg} is observed to be twice that of Γ, showing the conservation also in the merging process.

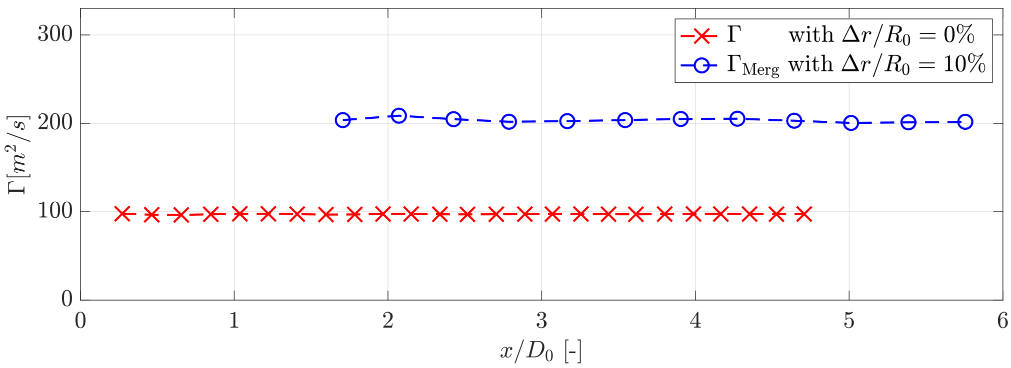

Figure 4.7: Evolution of circulation strength along streamwise direction

4.3.2. Vortex pair trajectory

To map the vortex trajectory, the classic particle tracking velocimetry technique is applied, assuming that the vortex travels based on the position of its center. With prescribing the initial vortex, their trajectory is spotted by the nearest neighbor within the defined search radius in the next time frame. By repeating this procedure for the tip vortices shed from both blades, the trajectory of the vortex pair can be obtained, as shown in Figure 4.8.

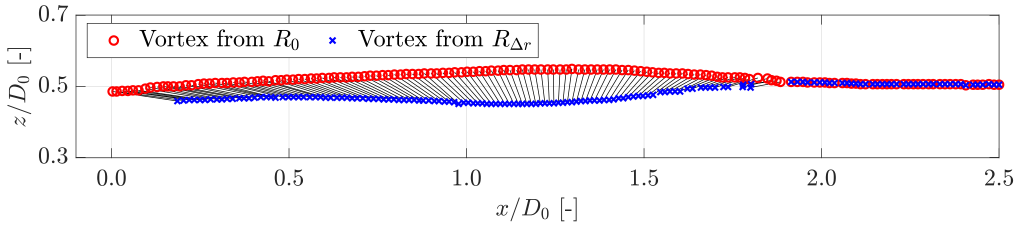

Figure 4.8: Vortex trajectory in an example of $\Delta r/R_0 = 10\%$ by particle tracking technique

The vortex pair's relative position at each time step is recorded. Figure 4.9 shows an example of the evolution of the separation of a vortex pair. The angle between the vortex pair relative to the streamwise direction β, separation distance b, and its streamwise $h_0 - \delta h$ and radial δr projection are plotted against the normalized x_c, the streamwise location of the vortex pair's centroid. This shows how their relative position changes as the vortex pair convects downstream.

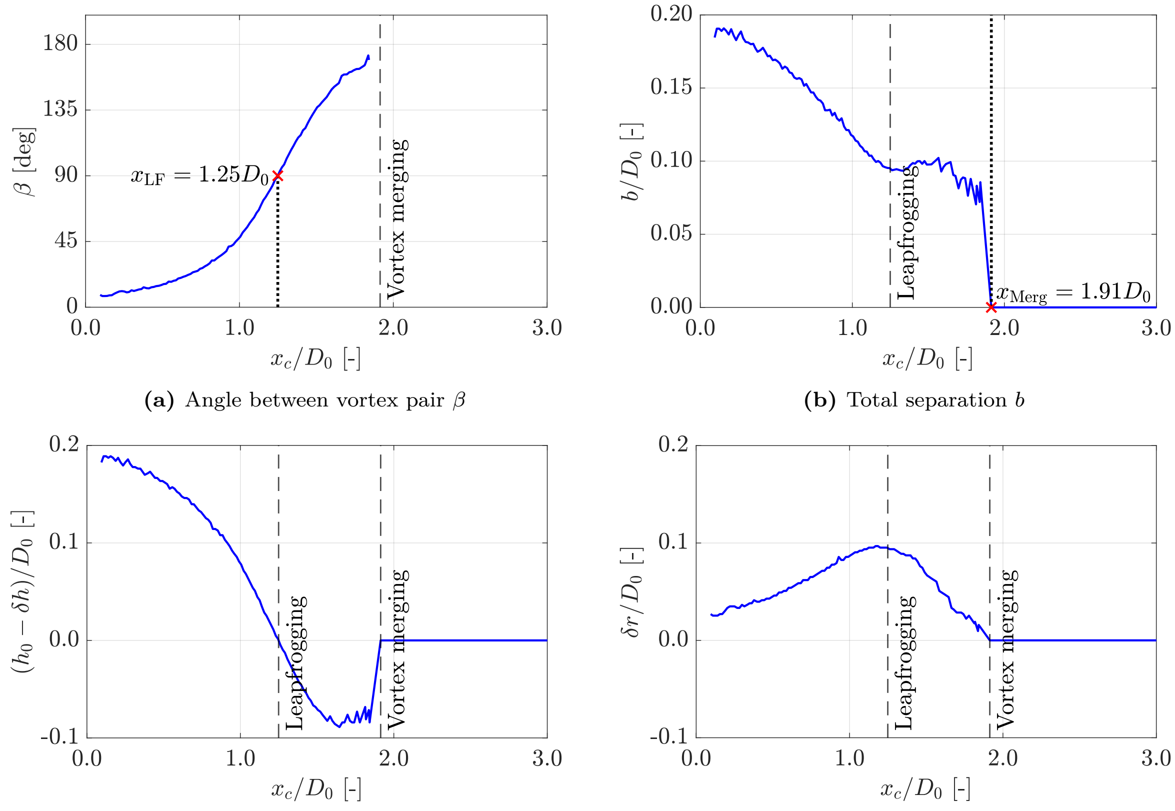

(a) Angle between vortex pair β

(b) Total separation b

(c) Streamwise separation $h_0 - \delta h$

(d) Radial separation δr

Figure 4.9: Evolution of Vortex pair relative position in an example of $\Delta r/R_0 = 10\%$

Figure 4.9a and Figure 4.9b present the evolution of β and b, from which the leapfrogging and merging distances can be determined. First, a monotonically increasing β suggests that the outer vortex gradually surpasses the inner one. When β reaches 90 degrees, indicating the vortex pair is swapping their streamwise positions, this location is identified as the leapfrogging distance, x_{LF}. Secondly, b decreases while the vortices convect downstream. This decrease reflects that vortex pairing behavior is not only dominated by the mutual inductance within them but also by other factors. Possible contributions may include induction from other vortices, velocity shear, or viscous effects. In addition, the merging distance x_{Merg} is defined when b drops to zero, although this measurement is related to the resolution in the identification of vortices.

Figure 4.9c and Figure 4.9d presents the evolution of δh and δr. In Figure 4.9c, streamwise separation decreases from h_0 and switches sign. The sign switching indicates the leapfrogging point and only one leapfrogging event can be spotted before the merging process begins. As for Figure 4.9d, the radial separation is observed to increase from around $0.03D_0$ and reaches maximum at around x_{LF}. There is a discrepancy between the initial δr and the blade length difference Δr around $0.02D_0$. This is attributed to the wake expansion. In specific, when the later vortex is shed from the original blade, the preceding vortex from the truncated blade has already traveled outward, decreasing the radial separation between them.

Furthermore, the evolution of δh and δr implies the leapfrogging mechanism besides vortex induction. In the case with only vortex induction within a vortex pair, they rotate around their centroid. and the motion of δh and δr should be symmetric $\beta = 45°$ axis. In terms of magnitude, variations in $h_0 - \delta h$ and δr are expected to be similar at least up to the leapfrogging distance where inviscid phenomena dominate. However, from the LES results the magnitude of the variation in δr before reaching the leapfrogging distance is approximately half of $h_0 - \delta h$. This observation can be attributed to two factors: 1. Influence of neighboring vortex besides pairing one is also significant; and 2. An additional mechanism is accelerating streamwise separation. Combined with the results observed from Section 4.1, convective velocity shear is also deduced to be important in leapfrogging motion under current settings. Thus, the next subsection will discuss the influence of convective velocity shear.

4.3.3. Impact on the wake profile

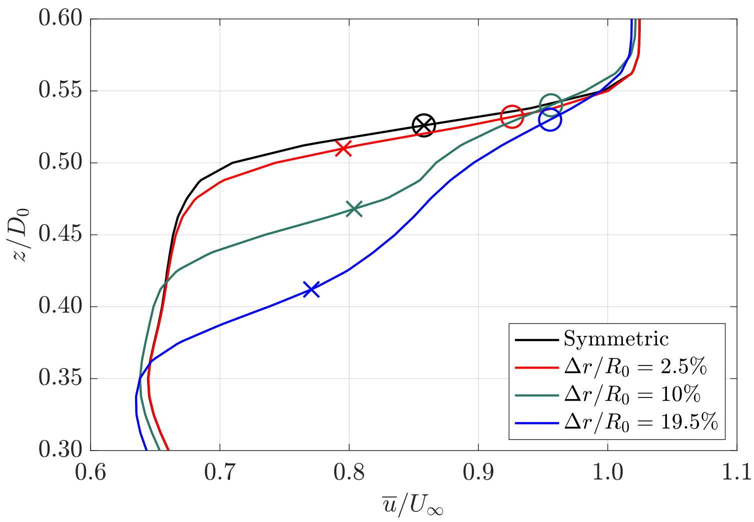

Figure 4.10: Mean velocity profile at $x = 1D$ for different $\Delta r/R_0$. Crosses indicate the positions of inner vortex cores at $x = 1D$, while circles mark the positions of outer vortex cores.

Figure 4.10 shows the velocity profiles at radial positions around the tip vortices. First, an evident velocity difference $\Delta\overline{u}$ between the outer and inner vortices can be observed. Due to the large velocity gradient at the wake boundary, even a small radial offset of $2.5\%R_0$ between the tip vortices results in a pronounced convective velocity difference between a vortex pair of approximately $0.12U_\infty$. As $\Delta r/R_0$ increases from 2.5% to 10%, $\Delta\overline{u}$ increases 15%.

Take the case with $\Delta r/R_0 = 10\%$ as an example. Considering the inflow velocity, helix properties, and the streamwise relative displacement due to the vortex pair, which is approximately $\Delta\overline{u} \cdot t$, the vortex pair will approach each other in the streamwise direction by $0.16D_0$ when convecting downstream by $1D_0$. This value approximately matches the difference in the variation of δh and δr shown in Figure 4.9. This provides evidence that the leapfrogging motion is influenced not only by induction but also by convection velocity, with velocity accounting for half of the contribution based on the observed values.

Second, a lower a by the asymmetric rotor can be identified. This is observed by the lower velocity deficit and the resulting gentler velocity gradient, highlighting the importance of considering the effective diameter when analyzing wake properties.

With information on the evolution of the relative positions of a vortex pair, the growth rate in time of the leapfrogging instability will be presented in Section 4.4. Besides, the resulting leapfrogging distances for all cases will be detailed in Section 4.5.

4.4. Growth of the leapfrogging instability

The growth rate was determined using the proposed method (Equation 2.37), based on data shown in Figure 4.9. The streamwise position of vortex pair centroid x_c is converted into dimensionless time t^* following Equation 2.27 and Equation 2.28.

Figure 4.11 shows the semi-log plots of the L1 norm of vortex pair relative positions with varying levels of rotor asymmetry. Across all cases, two common observations can be made. First, a linear region can be identified, indicating that the L1 norm methodology effectively captures the exponential growth of the leapfrogging instability. Similar to (Quaranta et al., 2019), the slope of this linear region is defined as the dimensionless instability growth rate from LES results, denoted as σ^*_{LES}. Second, at $t^* = 0$ the values of the L1 norm deviate from unity. According to the 2D vortex model, Δr should be the initial condition of $\delta h + \delta r$. However, due to wake expansion discussed in Subsection 4.3.2, the initial L1 norm is smaller than the blade length difference.

The growth rate σ^*_{LES} is observed to decrease with the blade length difference. As discussed in the previous sections, the leapfrogging motion under the current study is driven not only by mutual induction but also by the velocity shear between tip vortices. With a larger imposed Δr, the velocity difference increases, while the induction decreases due to the increased vortex pair separation distance. The decrease in growth rate suggests that the increase in velocity difference is less than the decrease in induction.

Furthermore, the initial value of the L1 norm approaches unity with a larger blade length difference. This can be attributed to two main reasons. Firstly, a larger Δr results in a smaller axial induction factor a, as shown in Table 3.4. A smaller a causes a less significant wake expansion according to the model proposed by Wilson (1986). Secondly, under a large Δr, the ratio between the wake expansion Δr decreases.

The growth rates obtained from the laminar inflow condition are subsequently compared to those from the turbulent inflow case and the 2D vortex model, as shown in Figure 4.12. It can be observed that the growth rates decrease with the blade length difference in accordance with the discussion in previous paragraphs. Besides, with a 5% TI, the growth rates are slightly larger than those obtained with laminar data, although more scattered. Moreover, σ^*_{LES} appears to be higher compared to σ^*_{2D}. This difference is attributed to the lack of consideration of 3D helical effects, velocity shear, and the viscous effect in the 2D vortex model. The difference between them decreases with increasing blade length difference. Specifically, σ^*_{LES} deviates from σ^*_{2D} by 17% for $\Delta r/R_0 = 2.5\%$ and decreases to 5% for $\Delta r/R_0 = 19.5\%$.

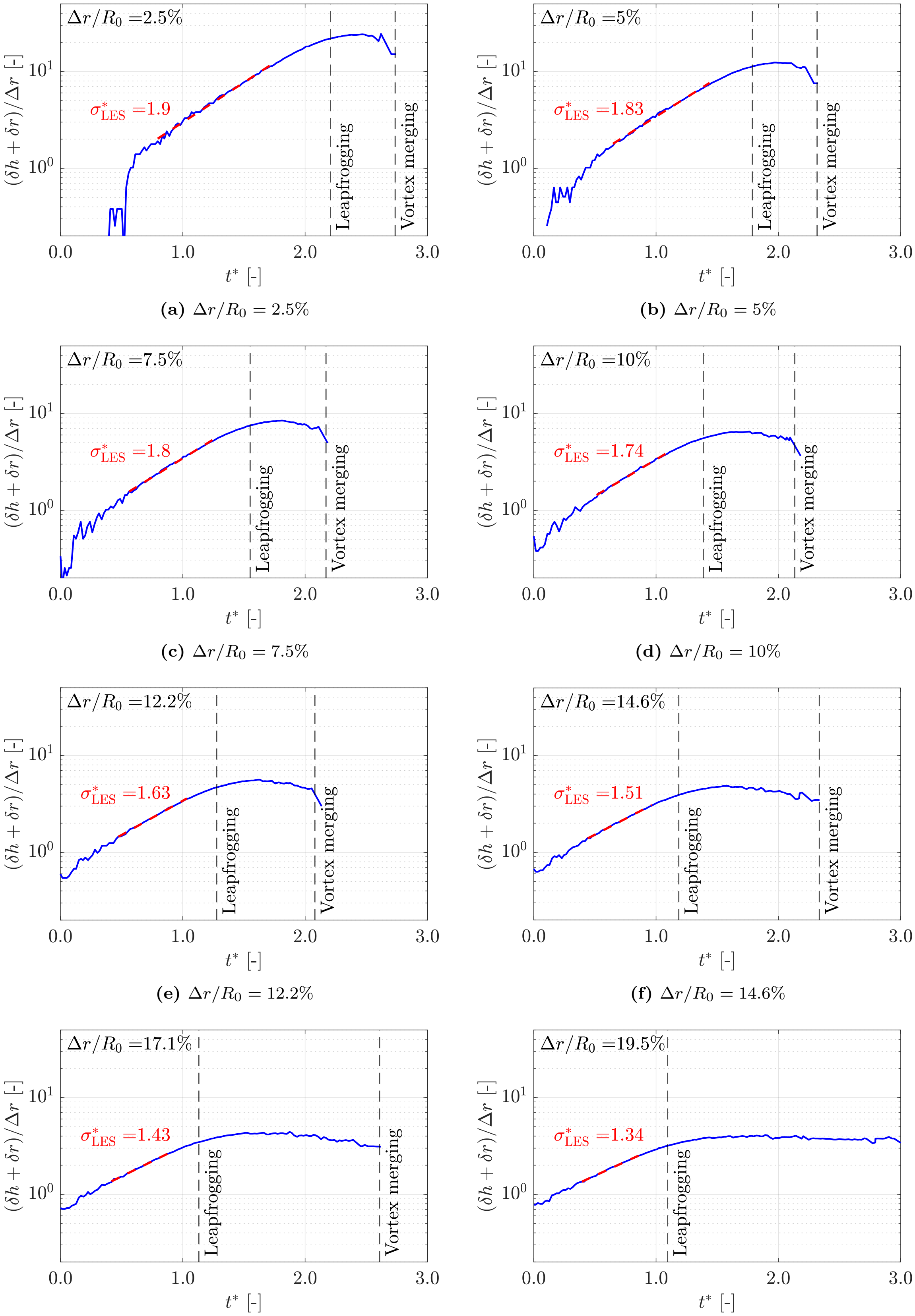

(a) $\Delta r/R_0 = 2.5\%$

(b) $\Delta r/R_0 = 5\%$

(c) $\Delta r/R_0 = 7.5\%$

(d) $\Delta r/R_0 = 10\%$

(e) $\Delta r/R_0 = 12.2\%$

(f) $\Delta r/R_0 = 14.6\%$

(g) $\Delta r/R_0 = 17.1\%$

(h) $\Delta r/R_0 = 19.5\%$

Figure 4.11: Time evolution of L1 norm with different $\Delta r/R_0$ from LES-ALM results

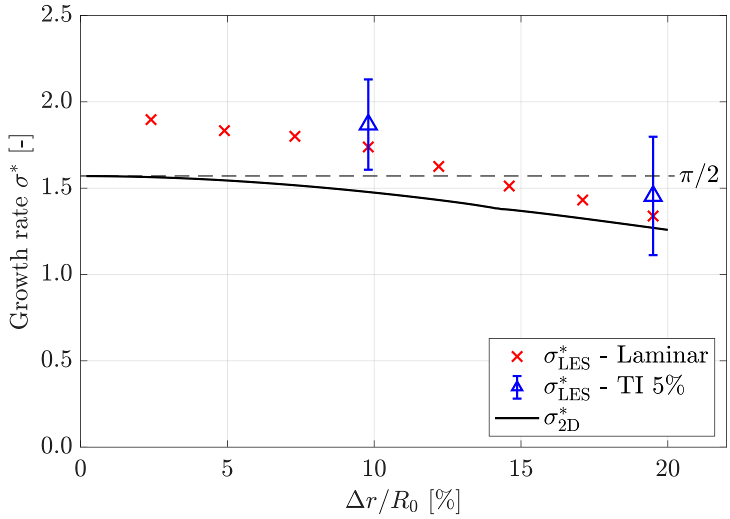

Figure 4.12: Normalized growth rate against blade length difference

4.5. Leapfrogging distance and time

The resulting leapfrogging distance and time are presented in this section. Figure 4.13 reports the leapfrogging distance against $\Delta r/R_0$ under different inflow conditions and blade length difference settings. Figure 4.14 demonstrates the normalized leapfrogging time t^*_{LF} against the $\Delta r/h_0$, offering a more general scale for comparison with the wind tunnel experiment (Mascioli, 2024) and 2D vortex model.

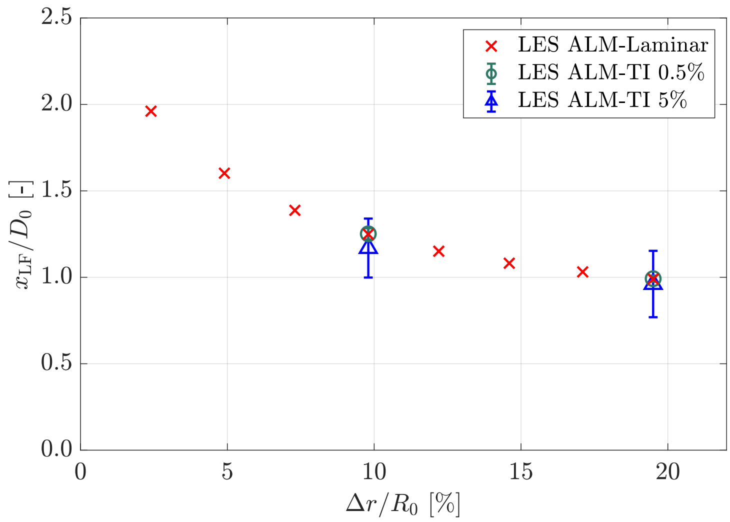

Figure 4.13: Normalized leapfrogging distance against blade length difference

Defined in Section 2.5, x_{LF} quantifies the leapfrogging events and is determined by the streamwise relative position of vortex pairs. Measurements were done for 20 pairs of vortices in each case for statistics. Plotted in Figure 4.13, the leapfrogging distance x_{LF} appears to decrease with $\Delta r/R_0$. This indicates that the leapfrogging phenomenon takes place earlier with a larger rotor asymmetry. Despite a smaller growth rate, a larger

$\Delta r/R_0$ imposes a more developed instability on the vortex pair, causing the leapfrogging to occur sooner. Moreover, x_{LF} is observed to be more sensitive with a smaller $\Delta r/R_0$ and tend to saturate in regions with a larger $\Delta r/R_0$. This indicates that, in terms of triggering the leapfrogging phenomenon, even a small perturbation can significantly affect the leapfrogging distance.

Turbulence intensity is found not to have a determining effect on the leapfrogging distance. The leapfrogging distances under 0.5% TI are similar to those under laminar inflow. However, 5% TI results in more scattered data, with the standard deviation shown as error bars. Overall, the mean values of x_{LF} are at most 6% lower than those under laminar inflow.

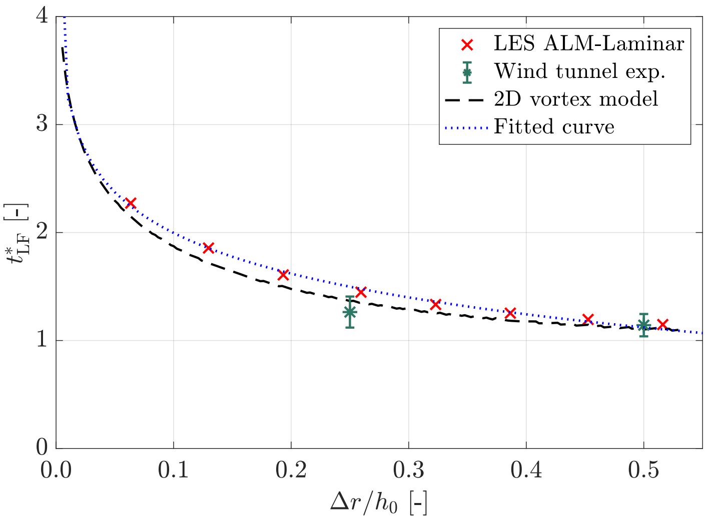

Figure 4.14: Normalized leapfrogging time against blade length difference

The obtained leapfrogging distances are subsequently converted into t^*_{LF} using Equation 2.27 and Equation 2.28. The blade length difference is then normalized by the initial streamwise distance, as in Abraham, Castillo-Castellanos, and Leweke (2023), and plotted in Figure 4.14 alongside experimental data and the 2D vortex model. The normalized leapfrogging time t^*_{LF} from all three sources shows agreement.

A logarithmic function is first fitted to LES ALM-Laminar data by Equation 4.3. The logarithmic function allows the infinity at $\Delta r = 0$ and saturate with a large Δr, and the coefficients c_1 and c_2 are found to be 0.544 and 0.744.

$$t^*_{\mathrm{LF}} = -c_1 \ln\left(\frac{\Delta r}{h_0}\right) + c_2 \tag{4.3}$$

In addition, the LES ALM-Laminar data points align well with the curve from the 2D vortex model. Such a consistency might seem contradictory given the differences between σ^*_{LES} and σ^*_{2D}. This contradiction stems from how the growth rates are determined. The growth rate takes into account both δh and δr, whereas the leapfrogging distance/time is defined solely by δh. Furthermore, σ^*_{LES} is calculated based on the slopes of linear sections of L1 norms, excluding the transient parts. In specific, the difference in δh

between Figure 4.9c and Figure 3.10b helps explain these observations. Namely, the difference in growth rates compensates for the initial effects of the tip vortex helix, resulting in a closely matched t^*_{LF} between the 2D vortex model and LES results.

The wind tunnel experiment data also aligns with the same curve observed in the simulations. The experiment was performed in the W-tunnel at TU Delft, using a 0.3m diameter, four-bladed rotor with an inflow velocity of approximately 5.4m/s. The tip speed ratio was set at 3.5, leading to a similar helix geometry h_0/R_0. The consistency observed between the simulation and wind tunnel experiments suggests that both diameter- and circulation-based Reynolds numbers are not a determining factor in the leapfrogging phenomenon.

5

Results: Wake characteristic

One of the main research questions regards the influence of blade length difference on wake recovery. In this study, wake recovery is quantified by the profile of streamwise mean velocity and mean-flow kinetic energy flux, in Section 5.1 and Section 5.2 respectively. In each section, the study mainly focuses on the effect of blade length difference, followed by the influence of inflow turbulence intensity.

Eight cases are selected for display. Under a laminar inflow condition, 0%, 2.5%, 5%, 10% $\Delta r/R_0$ are chosen. In this relatively small blade length difference region, the differences in leapfrogging distances are more apparent, making the effects on wake recovery distinguishable. Additionally, cases with $\Delta r/R_0 = 0\%$ and 10% are used to study the influence of inflow turbulence intensity at levels of 0.5% and 5%.

The figures and discussions are based on the effective diameter introduced in Subsection 2.4.2, as it represents the length scale normalized by performance. Additionally, based on the convergence study presented in Subsection 3.3.1, the time-averaged data is expected to be axis-symmetric, with phase differences averaging out as the helix travels downstream. Therefore, similar to the previous chapter, the analysis in this chapter remains in the 2D xz plane.

5.1. Streamwise mean velocity

This section presents the streamwise mean velocity information, where mean velocity refers to the time-averaged velocity, denoted as $\overline{u}$. First, Subsection 5.1.1 displays the mean velocity contour, an overview of the influence of rotor asymmetry and TI. Secondly, Subsection 5.1.2 indicates disk-averaged velocities and radial profiles along the streamwise direction, offering a first-level quantification of wake recovery. Lastly, Subsection 5.1.3 documents the growth of wake boundary based on $\overline{u}$ profile.

5.1.1. Mean velocity fields

Figure 5.1 shows the contours of the mean velocity under a laminar condition. As observed, the wake remains stable, with a minimal radial expansion or recovery in any case, despite the evident velocity shear at the tip boundary. As discussed in the previous

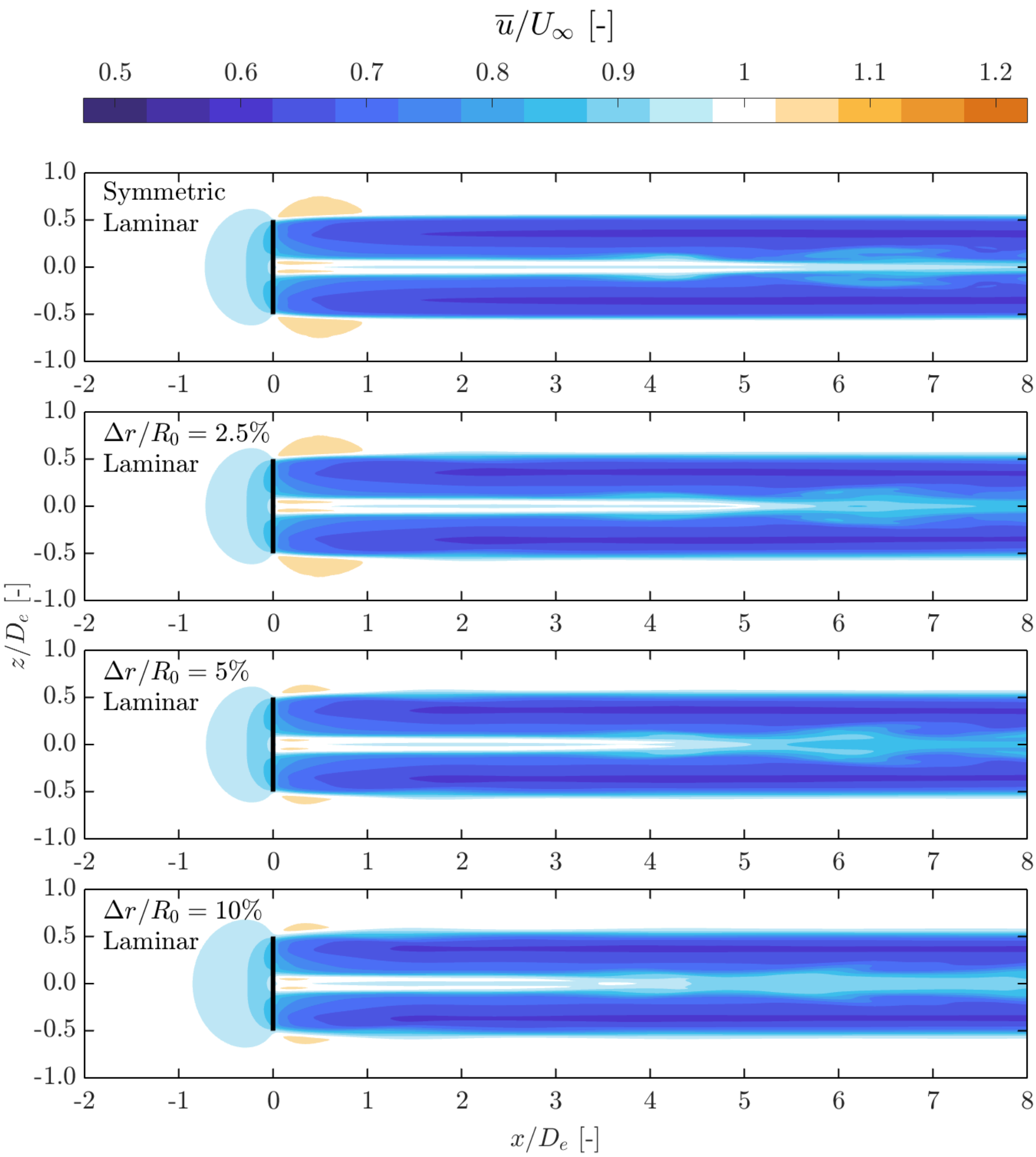

Figure 5.1: Mean velocity field with different $\Delta r/R_0$ under laminar inflow condition

chapter, perturbed tip vortices merge into a larger vortex and convect downstream in a stable manner. Namely, the leapfrogging effect remains localized, and the merged vortex resembles a 'Kelvin cat's eyes' pattern. This suggests that in the absence of external perturbations, one observes no breakdown of the tip vortex helix within the domain, shielding the wake as described by Medici (2005).

Figure 5.2 plots the mean velocity contour under turbulent conditions. It can be observed that not only does the wake boundary expand, but the shear layer also grows as moving

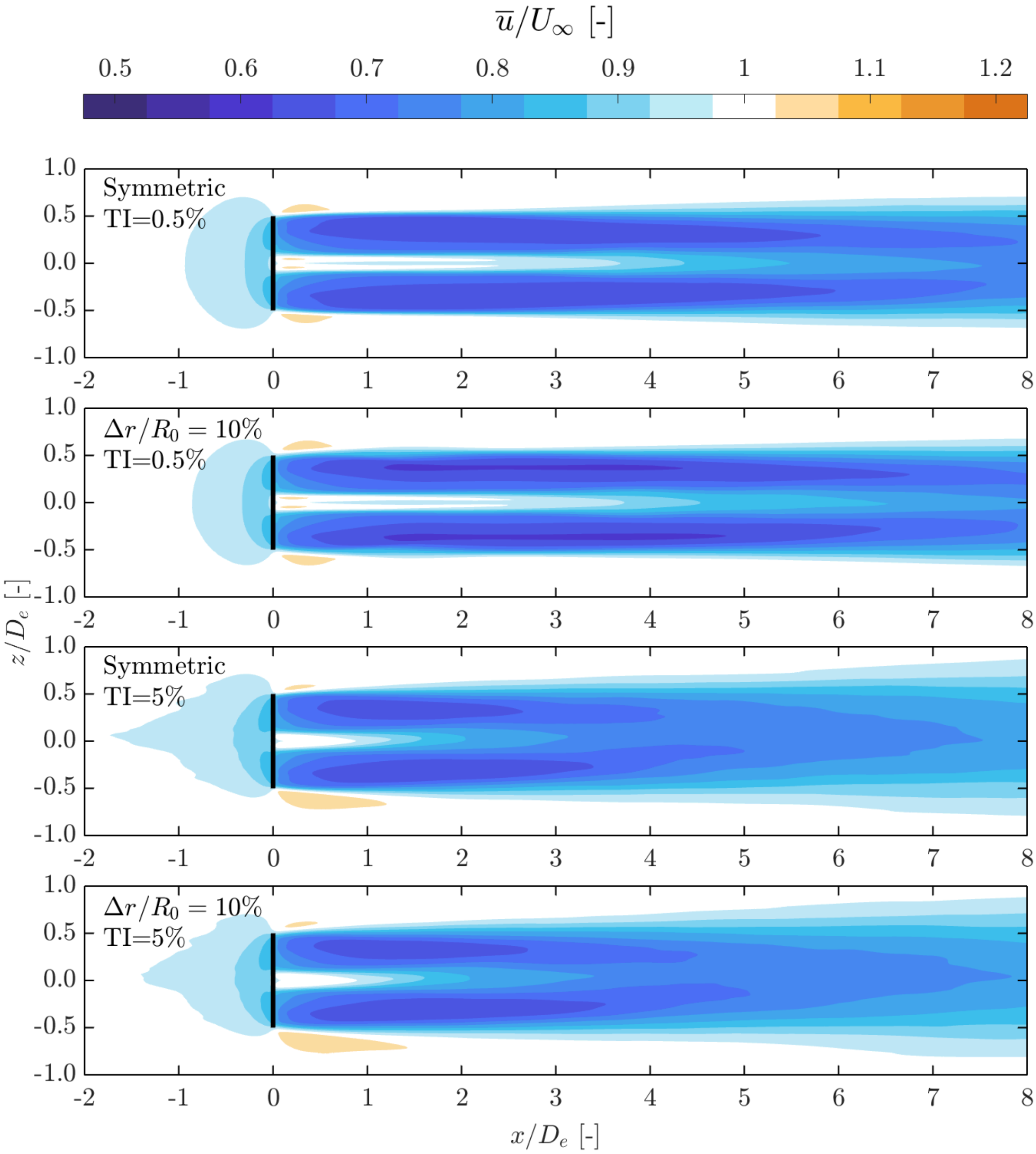

Figure 5.2: Mean velocity field with different $\Delta r/R_0$ under turbulent inflow conditions

downstream. This gives a sign of wake recovery, suggesting that the extent of expansion is more dependent on TI than on blade length differences. To further investigate them, Subsection 5.1.2 and Subsection 5.1.3 present the quantification of wake velocity and expansion.

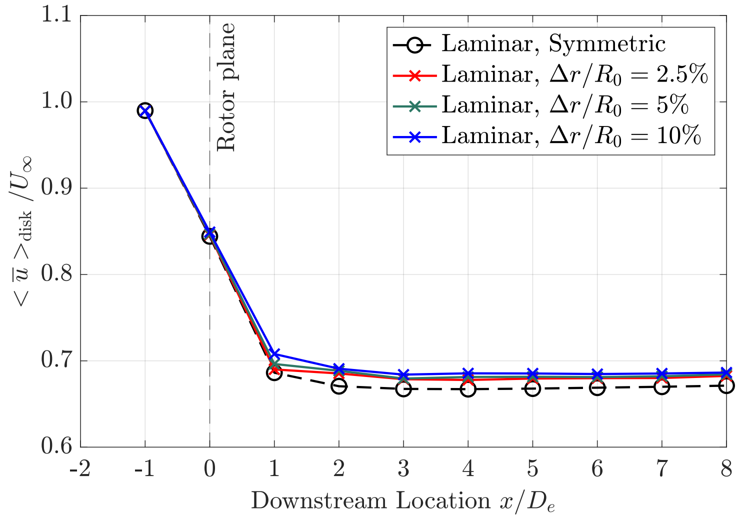

Figure 5.3: Disk-averaged streamwise velocity at downstream locations under laminar inflow

5.1.2. Disk-averaged velocity and radial velocity profiles

In this study, the disk-averaged streamwise velocity $< \overline{u} >_{\text{disk}}$ serves as a metric for evaluating wake recovery. This metric is calculated by averaging the time-averaged streamwise velocity $\overline{u}$ over a circular disk with a diameter of D_e. Such an approach provides insight into overall streamwise velocity, estimating the wind resource available to the downstream turbine. Namely, more pronounced wake recovery is indicated by a more rapid increase in $< \overline{u} >_{\text{disk}}$ along the streamwise direction.

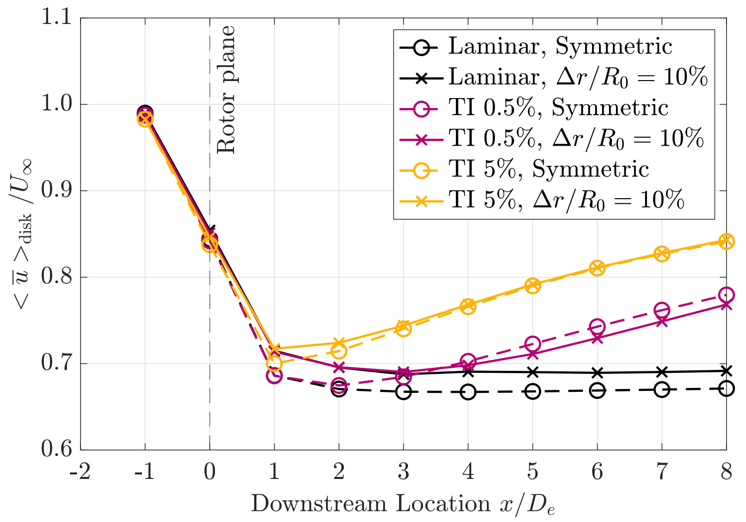

Figure 5.4: Disk-averaged streamwise velocity at downstream locations with different turbulent inflow conditions

Figure 5.3 plots $< \overline{u} >_{\text{disk}}$ against downstream location x/D_e with different $\Delta r/R_0$ under laminar inflow condition. Prior to reaching $x/D_e = 2$, $< \overline{u} >_{\text{disk}}$ decreases from the freestream velocity, which is attributed to rotor induction and wake expansion. The magnitude of this reduction varies between cases, reflecting slight differences in induction.

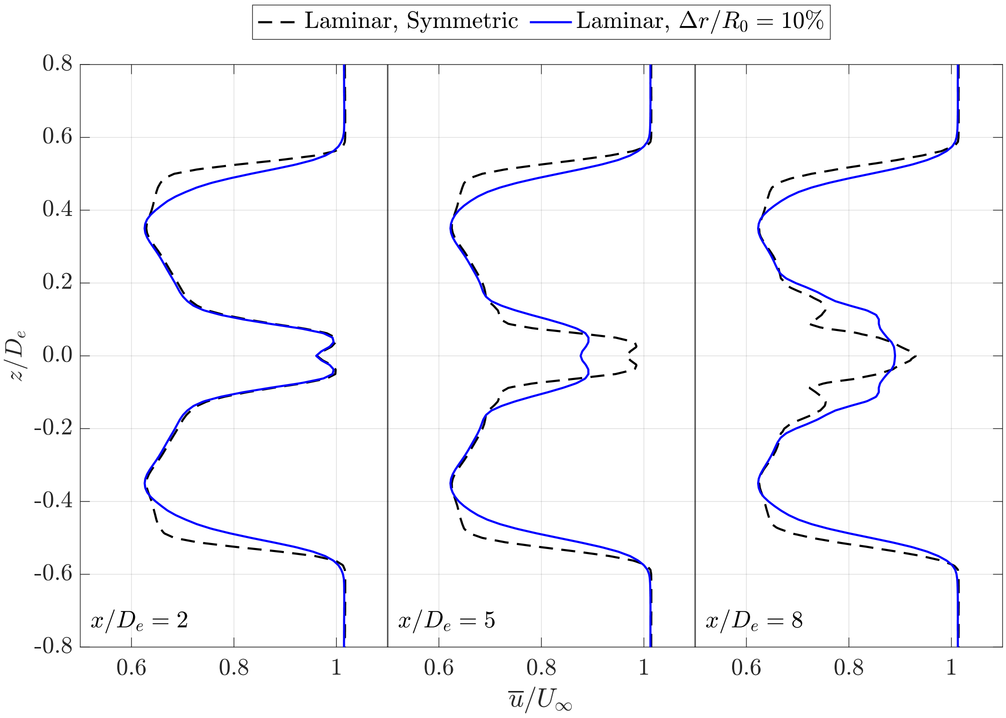

(a) under laminar inflow condition

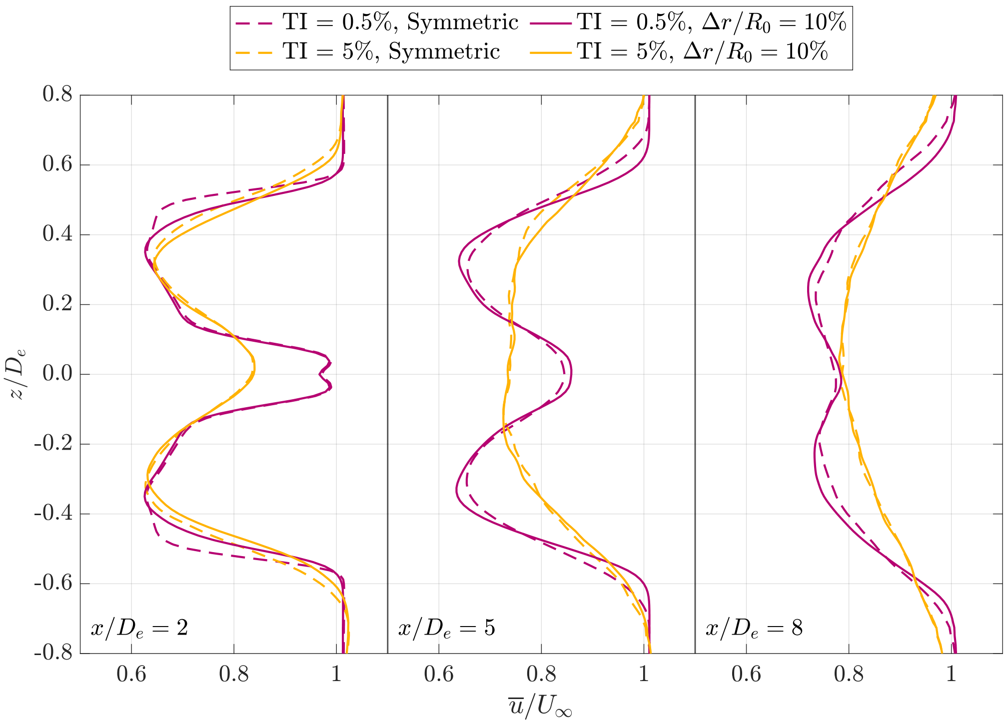

(b) with turbulence inflow conditions

Figure 5.5: Radial velocity profiles at 2, 5, and $8D_e$

Beyond $x/D_e = 2$, $< \overline{u} >_{\text{disk}}$ from each case remains approximately constant, indicating minimal or no wake recovery regardless of rotor configuration. The rate of increase in $< \overline{u} >_{\text{disk}}$ is approximately 0.15% per D_e for the symmetric rotor case, compared to 0.03% per D_e for the case with $\Delta r/R_0 = 10$.

Figure 5.5a shows more detail on this pattern by velocity profile. First, the gentle gradient of mean velocity due to rotor asymmetry results in a higher $< \overline{u} >_{\text{disk}}$, which is calculated inside $|z/D_e| < 0.5$. Besides, no evident variation is spotted at the tip region along streamwise direction, while the boundary layer at the hub region appears to develop.

On the other hand, Figure 5.4 shows the $< \overline{u} >_{\text{disk}}$ under different turbulent inflow conditions. A more evident difference can be observed. The trend in $< \overline{u} >_{\text{disk}}$ seems to be influenced more by TI than by rotor asymmetry. With increasing TI, the velocity recovers more rapidly, suggesting more effective wake recovery. Combining this and observations from Figure 4.1 and Figure 4.3, one might relate the stability of tip vortex to the wake recovery capability as stated by (Lignarolo et al., 2015). Additionally, higher TI appears to mitigate the effects of rotor asymmetry, leading to more similar recovery curves.

Figure 5.5b shows the radial velocity under turbulent inflow. With 0.5% TI, the profiles at $x/D_e = 2$ resemble those under laminar inflow. However, as the wake moves downstream, the boundary layer grows, and the wake behind the symmetric rotor recovers slightly faster. For cases with 5% TI, the wake development is more pronounced, and by $x/D_e = 5$, the double concavity appears to flatten.

These two sets of plots agree with each other, and three statements can be concluded from them. First, by solely blade length difference, the wake recovery does not help the wake to recover in terms of velocity. Second, the inflow TI seems to dominate the wake recovery process. Third, the rotor asymmetry slightly delays the wake recovery with a low level of TI whereas the effect of blade length difference with an atmospheric boundary level of TI.

5.1.3. Expansion of wake boundary

Explained by the continuity equation, the wake is expected to expand in the radial direction depending on the ambient turbulence level and global loading (Porté-Agel et al., 2020). This subsection reports the wake expansion for cases with varying blade length differences and inflow TI. Figure 5.6 compares the wake expansion of different $\Delta r/R_0$ under a laminar inflow condition. Besides, Figure 5.7 explores the impact of varying TI levels on wake expansion both with or without blade length difference. Note that the wake boundary uses the widely accepted definition of being at $0.99U_\infty$.

With a laminar inflow condition, the wake boundaries from different rotor configurations converge toward values as they approach farther downstream positions. In the near wake, the boundary behind a symmetric rotor expands monotonically, reaching approximately $0.565D_e$, whereas the ones behind an asymmetric rotor experience overshoot and oscillation. The peak of the overshoot occurs near the leapfrogging distance and appears more upstream as the $\Delta r/R_0$ increases, suggesting a correlation with leapfrogging motion.

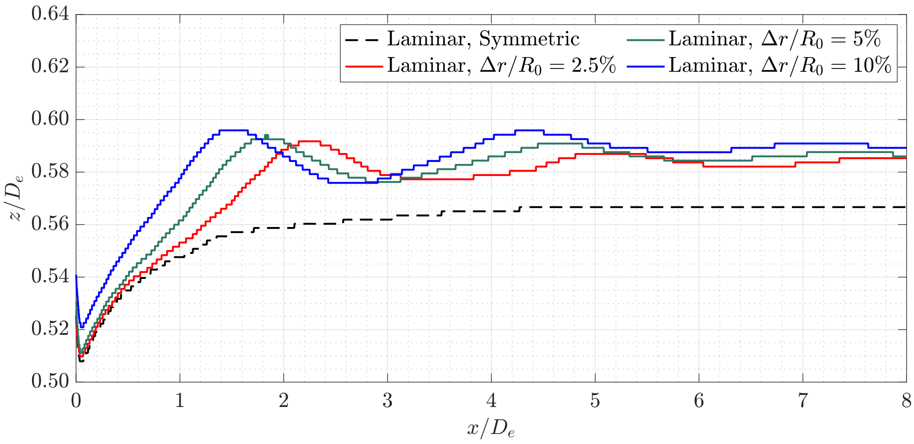

Figure 5.6: Wake boundaries under laminar inflow condition

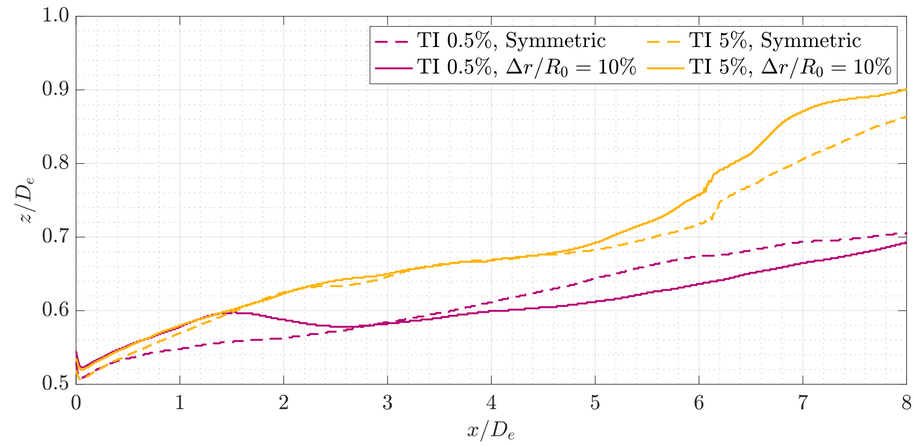

Figure 5.7: Wake boundaries with different turbulent inflow conditions

Besides, the wake boundaries converge to around $0.58D_e$, which is slightly larger than that observed with a symmetric rotor due to the definition of effective diameter.

Under turbulent inflow conditions, the wake boundary continues to expand within the current domain. With a laboratory-level TI of 0.5%, oscillatory behavior due to rotor asymmetry is also observed. However, compared to laminar inflow cases, the overall wake boundaries increase much more along the streamwise direction. At a TI of 5%, the wakes expand even further, and the influence of rotor asymmetry becomes less evident. Similar to $< \overline{u} >_{\text{disk}}$, wake expansion appears to be dominated by TI, with higher TI leading to greater expansion.

5.2. Mean-flow kinetic energy flux

In the previous section, the disk-averaged velocity profiles were presented, providing an overall understanding of wake recovery. However, to further investigate the influence of blade length differences and quantify kinetic energy entrainment, ϕ_{xz} is studied in this section. This property reflects the mean flow kinetic energy transport due to Reynolds stress, which the intended leapfrogging motion aims to increase. Subsection 5.2.1 displays the fields of ϕ_{xz} within the computational domain, while Subsection 5.2.2 shows the cumulative sum of ϕ_{xz} along the streamwise direction at the wake boundary.

5.2.1. Mean-flow kinetic energy flux fields

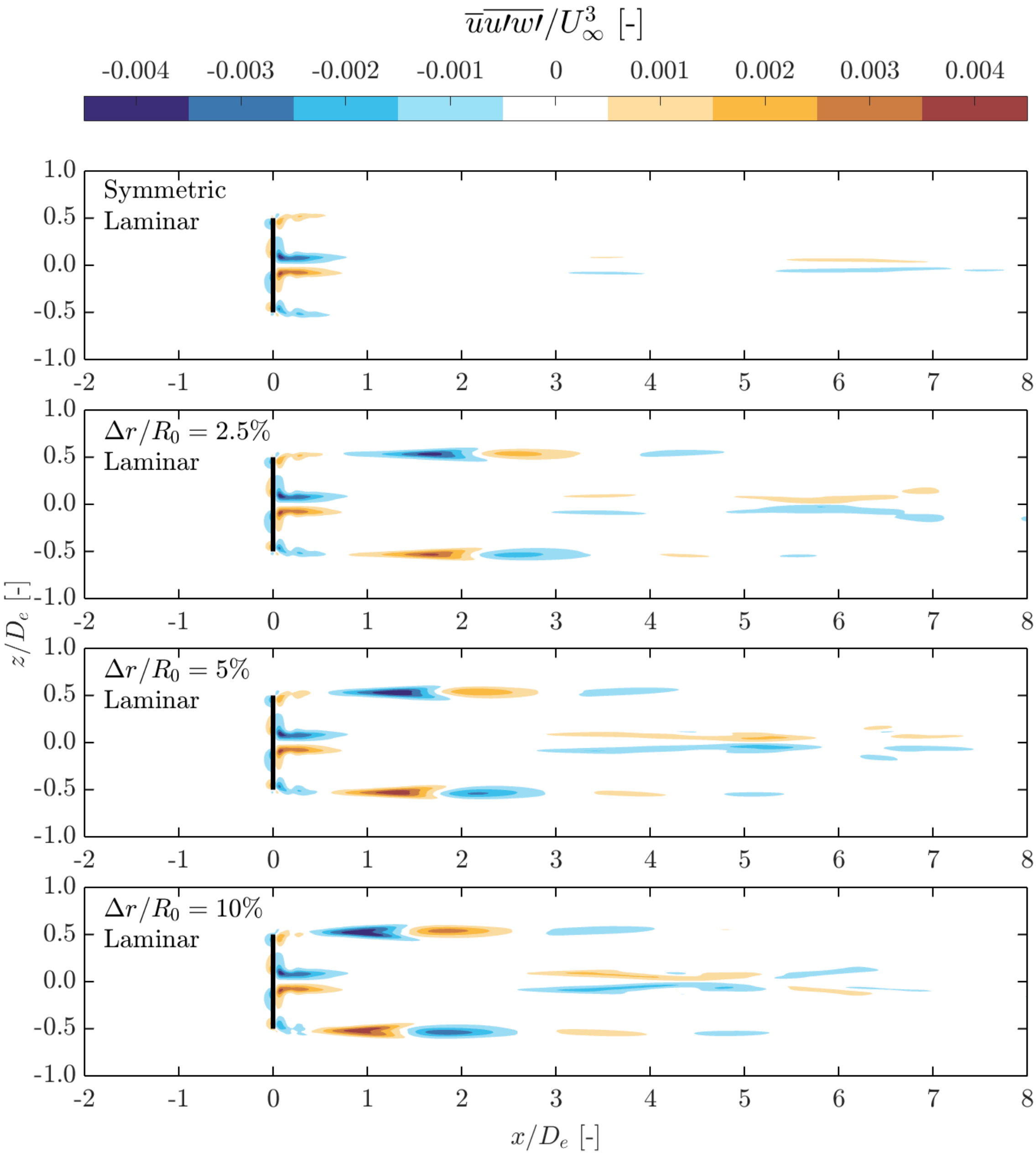

Figure 5.8: Mean-flow kinetic-energy flux with different $\Delta r/R_0$ under laminar inflow condition

This section shows the spatial distribution of mean-flow kinetic energy flux within the computational domain. As introduced in Section 2.7, $\phi_{xz} = \overline{u u' w'}$ represents the flux of mean flow kinetic energy due to Reynolds stress. Figure 5.8 and Figure 5.9 shows

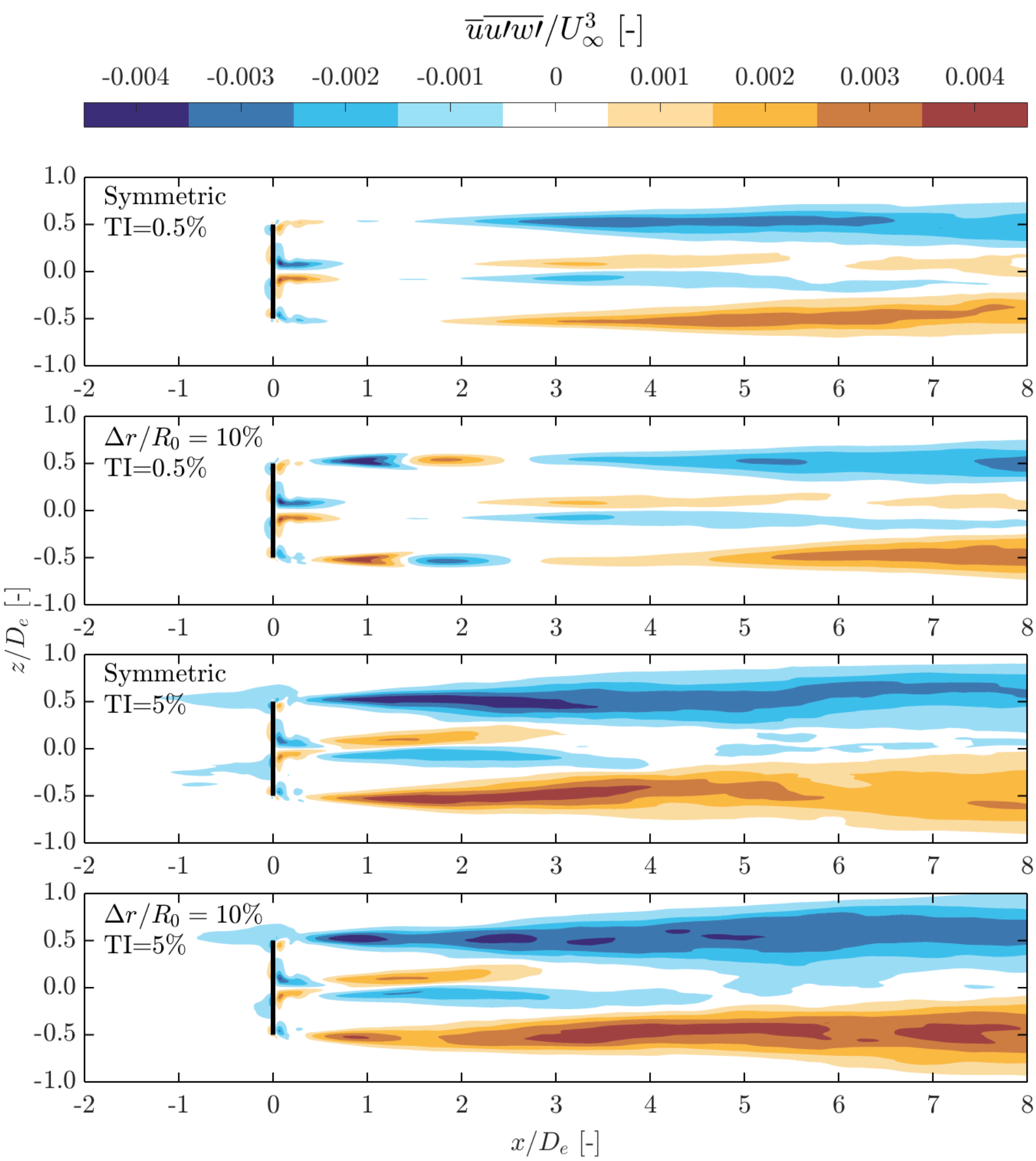

Figure 5.9: Mean-flow kinetic-energy flux with different $\Delta r/R_0$ under turbulent inflow conditions

the fields of normalized ϕ_{xz} with different level of rotor asymmetry and inflow condition.

In every case, ϕ_{xz} is more pronounced at the wake boundaries where the velocity shear is high and vortex pairing events occur. Besides, the symmetry of the contour shape along the wake centerline indicates the convergence of the simulations. However, the values have opposite signs, which is attributed to the opposite Reynolds stress components resulting from symmetric velocity shear directions. Considering the normal vector in

Equation 2.39, which is defined as pointing toward the wake centerline, the negative value of ϕ_{xz} at the wake boundary where $z > 0$ suggests that the kinetic energy flux is directed into the wake, and vice versa for $z < 0$.

Under laminar inflow conditions, the distribution of ϕ_{xz} appears to depend on the blade length difference. With a symmetric rotor, fluxes are only observable at $x/D_e < 1$, where the wake expands the most. No fluxes are found in the subsequent tip region under the current colormap arrangement. However, with a blade length difference, ϕ_{xz} becomes more apparent. The kinetic energy is transported into the wake, reaching local maxima before decreasing and becoming inward again. This alternate pattern appears to follow the leapfrogging distances corresponding to different levels $\Delta r/R_0$, suggesting a correlation with the leapfrogging motion. Combined with observation in Figure 4.1, ϕ_{xz} cannot be specifically identified when the vortex pair merge and form a new independent vortex convecting downstream.

With a 0.5% inflow TI, ϕ_{xz} is more evident throughout the domain compared to laminar inflow conditions. Fluxes are observed from $x/D_e = 2$ onwards, and the layer continues to grow along the streamwise direction, with the outermost boundary resembling the wake expansion. This provides evidence that the mixing due to Reynolds stress continues to increase. With a 10% $\Delta r/R_0$, the fluxes have an alternate pattern similar to the laminar case. After one period, a similar but later growth in the ϕ_{xz} layer is observed as seen with a symmetric rotor. In other words, the rotor asymmetry appears to delay the start of the mixing process under a 0.5% inflow TI.

Under 5% inflow TI, the development of ϕ_{xz} begins immediately behind the rotor and grows significantly. This suggests a more pronounced mixing process, regardless of the presence of rotor asymmetry. At this level of TI, the influence of rotor asymmetry is relatively difficult to identify. Similar to the findings from the vorticity field and mean velocity field, ϕ_{xz} appears to be dominated by the inflow TI than the rotor asymmetry.

5.2.2. Cumulative mean-flow kinetic energy flux

To evaluate the net transport of kinetic energy across the wake, ϕ_{xz} is integrated along the wake boundary. This indefinite integration focuses on ϕ_{xz}, which represents radial transport, and is performed along the streamwise boundaries determined by the converged wake boundaries specified in Subsection 5.1.3. As a result, the integration along these boundaries yields the cumulative sum of fluxes, denoted as $\mathrm{CSF}(x)$ and shown in Equation 5.1. Specifically, $z/D_e = \pm 0.56$ is used for the baseline case and $z/D_e = \pm 0.58$ for the asymmetric rotor case under laminar inflow. Under turbulent inflow conditions, where the wake boundary does not converge, an integrated boundary of $z/D_e = \pm 0.58$ is imposed.

$$\mathrm{CSF}(x) = \int_0^x \phi_{xz} \cdot \mathbf{n}_z dx \tag{5.1}$$

Figure 5.10 shows the normalized CSF under laminar inflow conditions. With a symmetric rotor, observable changes in CSF occur only at $x/D_e < 2$, attributed to wake

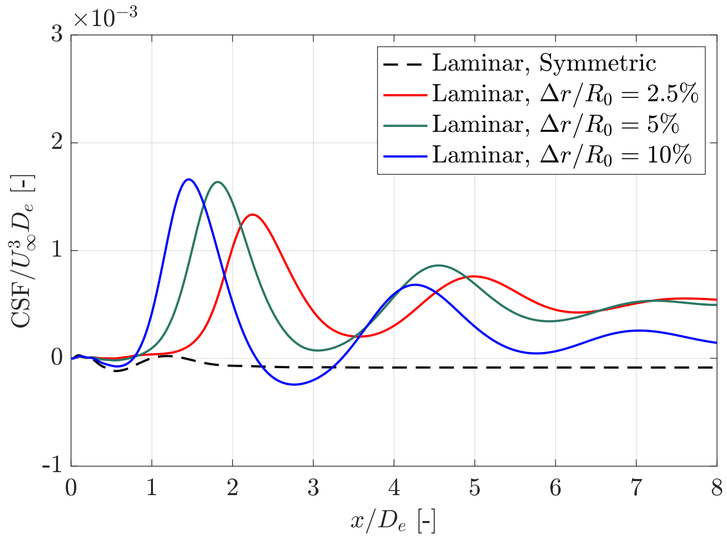

Figure 5.10: Mean-flow kinetic-energy flux with different $\Delta r/R_0$ under laminar inflow conditions

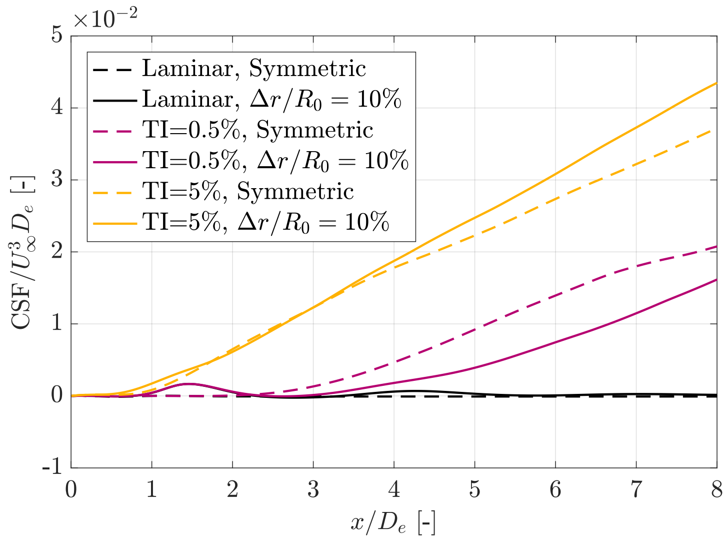

Figure 5.11: Mean-flow kinetic-energy flux with different $\Delta r/R_0$ under turbulent inflow conditions

expansion due to minimal interaction of the tip vortex array. In contrast, an asymmetric rotor exhibits oscillatory behavior in CSF. This oscillation corresponds to the periodic patterns observed in Figure 5.8 and appears to shift more upstream with blade length differences, correlating with leapfrogging distances. Furthermore, the amplitude of these oscillations decays in the streamwise direction, with peaks occurring just after the x_{LF}. This suggests that the leapfrogging instability triggered by blade length differences leads to the mean-flow kinetic energy flowing in and out. Then, as the merged vortex array stabilizes, the oscillations diminish.

Figure 5.11 compares the influence of blade length differences and inflow TI. Firstly, it is evident that the CSF is at least one order lower under laminar inflow conditions compared to that with a low (0.5%) inflow TI. This suggests that turbulent mixing cannot be effectively enhanced by rotor asymmetry alone, as it is insufficient to break down the tip vortex array. Secondly, with a 0.5% TI, the oscillatory motion observed in the case with rotor asymmetry appears to delay the transport, as seen in Figure 5.9. Thirdly, CSF increases more under a 5% TI, and the effect of rotor asymmetry is less pronounced in the near wake. However, further downstream, the asymmetric rotor seems to enhance the transport. CSF with the symmetric rotor (yellow-dashed line) and the asymmetric rotor (yellow-solid line) deviate around $x/D_e = 4$, coinciding with the development of their wake boundaries. Nonetheless, this enhanced transport at $0.6D_e$ is not captured by $< \overline{u} >_{\text{disk}}$, which averages over a disk with a radius of $0.5D_e$. Therefore, the benefit of wake recovery is not reflected in Figure 5.4.

6

Conclusion and recommendation

This chapter concludes the thesis and provides recommendations for future research directions.

6.1. Conclusion

This research explores the impact of blade length differences on tip vortex behavior and wake recovery for a two-bladed rotor using numerical methods. The large eddy simulation with the actuator line model is applied to a modified NREL 5MW turbine, investigating blade length differences of up to $30\%R_0$ under both laminar and two different turbulent inflow conditions. In addition, a novel approach, based on a 2D vortex model, is developed and applied to LES-ALM to analyze the growth rate of leapfrogging instability. Lastly, wake recovery is studied through disk-averaged velocity and mean-flow kinetic energy flux. On these findings, the research questions are answered as follows:

How does rotor asymmetry in terms of blade length difference affect tip vortex behavior?

In Chapter 4, it is found that the blade length difference triggers the leapfrogging instability by both mutual induction and the difference in convective velocity. Besides, under the laminar inflow condition, the vortex pairing is followed by their merger convecting downstream stably. Namely, 1. Both inviscid and viscous effects are non-negligible to describe resulting tip vortex behavior; and 2. Perturbation solely by blade length difference is not capable of breaking down the wake helical structure.

What correlation exists between the degree of blade length difference and its impact on leapfrogging instability?

In Chapter 4, it is found that the leapfrogging distance decreases with the degree of blade length difference. In other words, the leapfrogging event occurs more upstream with a larger rotor asymmetry shown in Figure 4.13. In addition, the instability growth rate decreases with blade length difference observed from both LES-ALM results and the 2D vortex model. Lastly, LES-ALM results and the wind tunnel experiment agree with each other on the normalized leapfrogging time, showing the independence of the global Reynolds number.

In what way does rotor asymmetry, induced by blade length difference, influence wake recovery?

Based on the $<\overline{u}>_{\text{disk}}$ profile, the leapfrogging motion triggered by solely blade length differences does not effectively enhance the rate of wake recovery, due to the lack of helix breakdown. The ϕ_{xz} plot reveals that kinetic energy alternately flows in and out of the wake boundary at a similar amount, with the amplitude of this oscillation decreasing in the streamwise direction. Considering the correlation of phase shift and tip vortex pair behavior, this oscillation is attributed to the leapfrogging motion, and it diminishes as the vortex pair merges. As a result, the overall gain in kinetic energy entrainment is found to be trivial.

Does the influence of rotor asymmetry on wake recovery alter with the inflow turbulence level?

Inflow turbulence plays a more dominant role in the wake recovery process than rotor asymmetry, as indicated by the $<\overline{u}>_{\text{disk}}$ profile, where $<\overline{u}>_{\text{disk}}$ increases more rapidly along the streamwise direction with higher turbulence intensity. At a laboratory-level turbulence intensity (0.5%), the oscillatory behavior of ϕ_{xz} delays the overall cumulative sum of kinetic energy flux. At an atmospheric boundary layer level of turbulence intensity (5%), the impact of rotor asymmetry diminishes within the streamtube of the turbine's diameter, while it does promote the wake expansion after $5D_e$ downstream.

6.2. Future recommendation

Beyond the scope of this thesis, several directions for further research can be explored:

On tip vortex dynamics

In this study, it was found that both convection and vortex induction significantly influence vortex dynamics, including growth rate and leapfrogging distance. The difference in convection between vortex pairs arises from the presence of the rotor and can be identified through velocity profiles. However, relying solely on velocity profiles is not sufficient to isolate the contributions from these two factors. In other words, any agreement between the vortex model and experiments or rotor simulations likely results from the interplay of compensating factors. Therefore, a key recommendation for future research on tip vortex dynamics would be to isolate the contributions of convection and vortex-inducing velocity more effectively.

Additionally, the ratio of subgrid-scale viscosity to physical viscosity ν_{sgs}/ν poses a challenge in large eddy simulations. This ratio can be estimated both locally, through Reynolds stress measurements, and globally, by examining the growth rate of the vortex core. In this study, ν_{sgs}/ν was found to be around 10^3 in the local tip vortex region, indicating that the mesh resolution in this area could be improved. However, refining the mesh reduces ν_{sgs}/ν increases the computational cost, as ν_{sgs} depends on the square of the mesh size. This makes it challenging to achieve a ν_{sgs}/ν of $O(10^1)$ Therefore, additional experimental data could be valuable in determining the optimal mesh quality, thereby increasing confidence in studies of tip vortex dynamics.

On wake recovery

From this study, it was observed that rotor asymmetry has a limited influence on the wake recovery process within the streamtube under both laminar and turbulent inflow conditions. The introduction of zero-wave number perturbations alone does not appear sufficient to disrupt the vortex helix, as the perturbation remains confined within the tip vortex region. Consequently, the tip vortex pair continues to shield the wake region.

Based on these findings, future research could explore modifications to rotor configurations to enhance wake recovery capabilities. Given that the merged vortex remains stable after leapfrogging, it may be possible to trigger a secondary leapfrogging event between merged vortex pairs. This could be achieved using a three or four-bladed rotor, with only one blade having a different length. Such a configuration is expected to produce a larger second merged tip vortex. With a larger tip vortex, increased interaction between the tip vortex and the hub vortex can be anticipated, introducing new dynamics involving counter-rotating vortices, which is also a potential topic for future work to break down the wake.

Furthermore, this study neglected real-world conditions, such as the influence of ground effects and atmospheric stability to isolate the asymmetry of the rotor itself within the computational domain. However, these factors alter wake characteristics due to wind shear (Abkar and Porté-Agel, 2015; Xie and Archer, 2015). In the context of enhancing the mixing process, these factors are expected to mitigate the impact of rotor configuration as influenced by turbulence intensity. Therefore, including these factors in future studies could help validate the potential benefits of such rotor configurations.

References

Abkar, M., & Porté-Agel, F. (2015). Influence of atmospheric stability on wind-turbine wakes: A large-eddy simulation study. *Physics of Fluids*, *27*(3), 035104. https://doi.org/10.1063/1.4913695

Abraham, A., Castillo-Castellanos, A., & Leweke, T. (2023). Simplified model for helical vortex dynamics in the wake of an asymmetric rotor. *Flow*, *3*. https://doi.org/10.1017/flo.2022.33

Abraham, A., & Leweke, T. (2023). Experimental investigation of blade tip vortex behavior in the wake of asymmetric rotors. *Experiments in Fluids*, *64*(6). https://doi.org/10.1007/s00348-023-03646-3

Abraham, A., Ramos-García, N., Sørensen, J., & Leweke, T. (2023). Numerical investigation of rotor asymmetry to promote wake recovery. *Journal of Physics: Conference Series*, *2505*. https://doi.org/10.1088/1742-6596/2505/1/012032

Ainslie, J. F. (1988). Calculating the flowfield in the wake of wind turbines. *Journal of Wind Engineering and Industrial Aerodynamics*, *27*(1), 213–224. https://doi.org/10.1016/0167-6105(88)90037-2

Amiri, M., Shadman, M., & Estefen, S. (2024). A review of physical and numerical modeling techniques for horizontal-axis wind turbine wakes. *Renewable and Sustainable Energy Reviews*, *193*. https://doi.org/10.1016/j.rser.2024.114279

Antonini, E., Romero, D., & Amon, C. (2020). Optimal design of wind farms in complex terrains using computational fluid dynamics and adjoint methods. *Applied Energy*, *261*. https://doi.org/10.1016/j.apenergy.2019.114426

Arabgolarcheh, A., Jannesarahmadi, S., & Benini, E. (2022). Modeling of near wake characteristics in floating offshore wind turbines using an actuator line method. *Renewable Energy*, *185*, 871–887. https://doi.org/10.1016/j.renene.2021.12.099

Aref, H. (1995). On the equilibrium and stability of a row of point vortices. *Journal of Fluid Mechanics*, *290*, 167–181. https://doi.org/10.1017/S002211209500245X

Bachant, P., Goude, A., daa-mec, & Wosnik, M. (2019, November). turbinesFoam/turbinesFoam: V0.1.1. https://doi.org/10.5281/zenodo.3542301

Bai, C.-J., & Wang, W.-C. (2016). Review of computational and experimental approaches to analysis of aerodynamic performance in horizontal-axis wind turbines (HAWTs). *Renewable and Sustainable Energy Reviews*, *63*, 506–519. https://doi.org/10.1016/j.rser.2016.05.078

Benard, P., Viré, A., Moureau, V., Lartigue, G., Beaudet, L., Deglaire, P., & Bricteux, L. (2018). Large-Eddy Simulation of wind turbines wakes including geometrical effects. *Computers & Fluids*, *173*, 133–139. https://doi.org/10.1016/j.compfluid.2018.03.015

Betz, A. (1919). Schraubenpropeller mit geringstem energieverlust. mit einem zusatz von l. prandtl. *Nachrichten von der Gesellschaft der Wissenschaften zu Göttingen, Mathematisch-Physikalische Klasse*, *1919*, 193–217. http://eudml.org/doc/59049

Bhagwat, M., & Leishman, J. (2002). Generalized viscous vortex model for application to free-vortex wake and aeroacoustic calculations. *58th Annual Forum and Technology Display of the American Helicopter Society International*.

Biswas, N., & Buxton, O. R. H. (2024). Effect of tip speed ratio on coherent dynamics in the near wake of a model wind turbine. *Journal of Fluid Mechanics*, *979*, A34. https://doi.org/10.1017/jfm.2023.1095

Bolnot, H. (2012). *Instabilités des tourbillons hélicoïdaux: Application au sillage des rotors* [Thèse de doctorat]. Institut de Recherche sur les Phénomènes Hors Équilibre.

Brown, K., Houck, D., Maniaci, D., Westergaard, C., & Kelley, C. (2022). Accelerated Wind-Turbine Wake Recovery Through Actuation of the Tip-Vortex Instability. *AIAA Journal*, *60*, 1–13. https://doi.org/10.2514/1.J060772

Burton, T. 1., Jenkins, N. 1., Sharpe, D., Bossanyi, E., & Graham, M. (2021). Wind energy handbook. John Wiley & Sons, Inc.

Castellani, F., Eltayesh, A., Becchetti, M., & Segalini, A. (2021). Aerodynamic analysis of a wind-turbine rotor affected by pitch unbalance. *Energies*, *14*(3). https://doi.org/10.3390/en14030745

Cerretelli, C., & Williamson, C. H. K. (2003). The physical mechanism for vortex merging. *Journal of Fluid Mechanics*, *475*, 41–77. https://doi.org/10.1017/S0022112002002847

Churchfield, M. J., Lee, S., Michalakes, J., & Moriarty, P. J. (2012). A numerical study of the effects of atmospheric and wake turbulence on wind turbine dynamics. *Journal of Turbulence*, *13*, N14. https://doi.org/10.1080/14685248.2012.668191

Dai, L., Zhou, Q., Zhang, Y., Yao, S., Kang, S., & Wang, X. (2017). Analysis of wind turbine blades aeroelastic performance under yaw conditions. *Journal of Wind Engineering and Industrial Aerodynamics*, *171*, 273–287. https://doi.org/10.1016/j.jweia.2017.09.011

Deardorff, J. W. (1980). Stratocumulus-capped mixed layers derived from a three-dimensional model. *Boundary-Layer Meteorology*, *18*(4), 495–527. https://doi.org/10.1007/BF00119502

DHPC, D. H. P. C. C. (2022). *DelftBlue Supercomputer (Phase 1)* [https://www-tudelft-nl.tudelft.idm.oclc.org/dhpc/ark:/44463/DelftBluePhase1].

Felli, M., Camussi, R., & Felice, F. D. (2011). Mechanisms of evolution of the propeller wake in the transition and far fields. *Journal of Fluid Mechanics*, *682*, 5–53. https://doi.org/10.1017/jfm.2011.150

Frederik, J. A., Doekemeijer, B. M., Mulders, S. P., & van Wingerden, J.-W. (2020). The helix approach: Using dynamic individual pitch control to enhance wake mixing in wind farms. *Wind Energy*, *23*(8), 1739–1751. https://doi.org/10.1002/we.2513

Germano, M. (1992). Turbulence the filtering approach. *Journal of Fluid Mechanics*, *238*(325), 325–336. https://doi.org/10.1017/S0022112092001733

Glauert, H. (1935). Airplane propellers. In *Aerodynamic theory: A general review of progress under a grant of the guggenheim fund for the promotion of aeronautics* (pp. 169–360). Springer Berlin Heidelberg. https://doi.org/10.1007/978-3-642-91487-4_3

Gupta, B. P., & Loewy, R. G. (1974). Theoretical Analysis of the Aerodynamic Stability of Multiple, Interdigitated Helical Vortices. *AIAA Journal*, *12*(10), 1381–1387. https://doi.org/10.2514/3.49493

Hand, M. M., Simms, D. A., Fingersh, L. J., Jager, D. W., Cotrell, J. R., Schreck, S., & Larwood, S. M. (2001, December). *Unsteady Aerodynamics Experiment Phase VI: Wind Tunnel Test Configurations and Available Data Campaigns* (tech. rep. No. NREL/TP-500-29955, 15000240). https://doi.org/10.2172/15000240

Hanjalic, K. (2005). Will RANS Survive LES? A View of Perspectives. *Journal of Fluids Engineering*, *127*(5), 831–839. https://doi.org/10.1115/1.2037084

Hansen, K. S., Barthelmie, R. J., Jensen, L. E., & Sommer, A. (2012). The impact of turbulence intensity and atmospheric stability on power deficits due to wind turbine wakes at Horns Rev wind farm. *Wind Energy*, *15*(1), 183–196. https://doi.org/10.1002/we.512

Hopfinger, E. J., & van Heijst, G. J. F. (1993). Vortices in Rotating Fluids. *Annual Review of Fluid Mechanics*, *25*(1), 241–289. https://doi.org/10.1146/annurev.fl.25.010193.001325

Huang, X., Alavi Moghadam, S. M., Meysonnat, P. S., Meinke, M., & Schröder, W. (2019). Numerical analysis of the effect of flaps on the tip vortex of a wind turbine blade. *International Journal of Heat and Fluid Flow*, *77*, 336–351. https://doi.org/10.1016/j.ijheatfluidflow.2019.05.004

Ivanell, S. (2005). *Numerical computations of wind turbine wakes* [Doctoral dissertation]. KTH.

Ivanell, S., Mikkelsen, R., Sørensen, J. N., & Henningson, D. (2010). Stability analysis of the tip vortices of a wind turbine. *Wind Energy*, *13*(8), 705–715. https://doi.org/10.1002/we.391

Jha, P. K., Churchfield, M. J., Moriarty, P. J., & Schmitz, S. (2014). Guidelines for Volume Force Distributions Within Actuator Line Modeling of Wind Turbines on Large-Eddy Simulation-Type Grids. *Journal of Solar Energy Engineering*, *136*(031003). https://doi.org/10.1115/1.4026252

Jimenez, A., Crespo, A., Migoya, E., & Garcia, J. (2007). Advances in large-eddy simulation of a wind turbine wake. *Journal of Physics: Conference Series*, *75*(1), 012041. https://doi.org/10.1088/1742-6596/75/1/012041

Jimenez, A., Crespo, A., & Migoya, E. (2009). Application of a LES technique to characterize the wake deflection of a wind turbine in yaw. *Wind Energy*, *13*, 559–572. https://doi.org/10.1002/we.380

Jonkman, J., Butterfield, S., Musial, W., & Scott, G. (2009, February). *Definition of a 5-MW Reference Wind Turbine for Offshore System Development* (tech. rep. No. NREL/TP-500-38060, 947422). https://doi.org/10.2172/947422

Kang, S., Yang, X., & Sotiropoulos, F. (2014). On the onset of wake meandering for an axial flow turbine in a turbulent open channel flow. *Journal of Fluid Mechanics*, *744*, 376–403. https://doi.org/10.1017/jfm.2014.82

King, R. N., Dykes, K., Graf, P., & Hamlington, P. E. (2017). Optimization of wind plant layouts using an adjoint approach. *Wind Energy Science*, *2*(1), 115–131. https://doi.org/10.5194/wes-2-115-2017

Lee, H., Sengupta, B., Araghizadeh, M. S., & Myong, R. S. (2022). Review of vortex methods for rotor aerodynamics and wake dynamics. *Advances in Aerodynamics*, *4*(1), 20. https://doi.org/10.1186/s42774-022-00111-3

Lee, H., & Lee, D.-J. (2019). Numerical investigation of the aerodynamics and wake structures of horizontal axis wind turbines by using nonlinear vortex lattice method. *Renewable Energy*, *132*, 1121–1133. https://doi.org/10.1016/j.renene.2018.08.087

Leishman, J., Bhagwat, M., & Bagai, A. (2002). Free-vortex filament methods for the analysis of helicopter rotor wakes. *Journal of Aircraft*, *39*(5), 759–775. https://doi.org/10.2514/2.3022

Leweke, T., Le Dizès, S., & Williamson, C. H. (2016). Dynamics and Instabilities of Vortex Pairs. *Annual Review of Fluid Mechanics*, *48*(1), 507–541. https://doi.org/10.1146/annurev-fluid-122414-034558

Li, Y.-T. (2023). *Numerical investigation of floating wind turbine wake interactions using les-al technique*.

Lignarolo, L. E. M. (2016). *On the Turbulent Mixing in Horizontal Axis Wind Turbine Wakes* [Doctoral dissertation].

Lignarolo, L. E. M., Ragni, D., Scarano, F., Ferreira, C. J. S., & van Bussel, G. J. W. (2015). Tip-vortex instability and turbulent mixing in wind-turbine wakes. *Journal of Fluid Mechanics*, *781*, 467–493. https://doi.org/10.1017/jfm.2015.470

Lilly, D. K. (1967). The representation of small-scale turbulence in numerical simulation experiments [IBM]. *Proceedings of the IBM Scientific Computing Symposium on Environmental Sciences*.

Lin, Y.-H., Chen, H.-K., & Wu, K.-Y. (2023). Prediction of aerodynamic performance of NREL offshore 5-MW baseline wind turbine considering power loss at varying wind speeds. *Wind Energy*, *26*(5), 493–515. https://doi.org/10.1002/we.2812

Lundquist, J., Schreck, S., Shaw, W., Petty, R., Williamson, A., Baldwin, S., Burge, S., & Green, B. (2008). U.S. Department of Energy Workshop Report: Research Needs for Wind Resource Characterization. *Renewable Energy*.

Maizi, M., Mohamed, M., Dizene, R., & Mihoubi, M. (2018). Noise reduction of a horizontal wind turbine using different blade shapes. *Renewable Energy*, *117*, 242–256. https://doi.org/10.1016/j.renene.2017.10.058

Malecha, Z., & Dsouza, G. (2023). Modeling of Wind Turbine Interactions and Wind Farm Losses Using the Velocity-Dependent Actuator Disc Model. *Computation*, *11*(11). https://doi.org/10.3390/computation11110213

Martínez-Tossas, L., Churchfield, M., & Leonardi, S. (2015). Large eddy simulations of the flow past wind turbines: Actuator line and disk modeling. *Wind Energy*, *18*(6), 1047–1060. https://doi.org/10.1002/we.1747

Martínez-Tossas, L., Churchfield, M., Yilmaz, A., Sarlak, H., Johnson, P., Sørensen, J., Meyers, J., & Meneveau, C. (2018). Comparison of four large-eddy simulation research codes and effects of model coefficient and inflow turbulence in actuator-line-based wind turbine modeling. *Journal of Renewable and Sustainable Energy*, *10*(3). https://doi.org/10.1063/1.5004710

Mascioli, A. (2024). *An experimental research of energy recovery in the wake of non-symmetrical rotors* [Master's Thesis]. Università Roma Tre.

Medici, D. (2005). Experimental studies of wind turbine wakes – power optimisation and meandering.

Mehta, D., van Zuijlen, A., Koren, B., Holierhoek, J., & Bijl, H. (2014). Large Eddy Simulation of wind farm aerodynamics: A review. *Journal of Wind Engineering and Industrial Aerodynamics*, *133*, 1–17. https://doi.org/10.1016/j.jweia.2014.07.002

Melander, M. V., Zabusky, N. J., & Mcwilliams, J. C. (1988). Symmetric vortex merger in two dimensions: Causes and conditions. *Journal of Fluid Mechanics*, *195*, 303–340. https://doi.org/10.1017/S0022112088002435

Mendoza, V., Chaudhari, A., & Goude, A. (2019). Performance and wake comparison of horizontal and vertical axis wind turbines under varying surface roughness conditions. *Wind Energy*, *22*(4), 458–472. https://doi.org/10.1002/we.2299

Meunier, P., & Leweke, T. (2001). Three-dimensional instability during vortex merging. *Physics of Fluids*, *13, n° 10*, p. 2747–2750. https://doi.org/10.1063/1.1399033

Moeng, C.-H. (1984). A Large-Eddy-Simulation Model for the Study of Planetary Boundary-Layer Turbulence. *Journal of the Atmospheric Sciences*, *41*(13), 2052–2062. https://doi.org/10.1175/1520-0469(1984)041<2052:ALESMF>2.0.CO;2

Nathan, J., Forsting, A. R. M., Troldborg, N., & Masson, C. (2017). Comparison of OpenFOAM and EllipSys3D actuator line methods with (NEW) MEXICO results. *Journal of Physics: Conference Series*, *854*(1), 012033. https://doi.org/10.1088/1742-6596/854/1/012033

Odemark, Y., & Fransson, J. H. M. (2013). The stability and development of tip and root vortices behind a model wind turbine. *Experiments in Fluids*, *54*(9), 1591. https://doi.org/10.1007/s00348-013-1591-6

Okulov, V. L., Naumov, I. V., Mikkelsen, R. F., Kabardin, I. K., & Sørensen, J. N. (2014). A regular Strouhal number for large-scale instability in the far wake of a rotor. *Journal of Fluid Mechanics*, *747*, 369–380. https://doi.org/10.1017/jfm.2014.174

Onel, H. C., & Tuncer, I. H. (2021). Investigation of wind turbine wakes and wake recovery in a tandem configuration using actuator line model with LES. *Computers & Fluids*, *220*, 104872. https://doi.org/10.1016/j.compfluid.2021.104872

OpenFOAM Foundation. (2021). *Openfoam user guide: Version 2106*. OpenFOAM Foundation. https://openfoam.org/release/2106/

Plaza, B., Bardera, R., & Visiedo, S. (2015). Comparison of BEM and CFD results for MEXICO rotor aerodynamics. *Journal of Wind Engineering and Industrial Aerodynamics*, *145*, 115–122. https://doi.org/10.1016/j.jweia.2015.05.005

Poletto, R., Craft, T., & Revell, A. (2013). A New Divergence Free Synthetic Eddy Method for the Reproduction of Inlet Flow Conditions for LES. *Flow, Turbulence and Combustion*, *91*(3), 519–539. https://doi.org/10.1007/s10494-013-9488-2

Pope, S. B. (2000). *Turbulent flows*. Cambridge University Press.

Pope, S. B. (2004). Ten questions concerning the large-eddy simulation of turbulent flows. *New Journal of Physics*, *6*(1), 35. https://doi.org/10.1088/1367-2630/6/1/035

Porté-Agel, F., Bastankhah, M., & Shamsoddin, S. (2020). Wind-Turbine and Wind-Farm Flows: A Review. *Boundary-Layer Meteorology*, *174*(1), 1–59. https://doi.org/10.1007/s10546-019-00473-0

Quaranta, H. U., Bolnot, H., & Leweke, T. (2015). Long-wave instability of a helical vortex. *Journal of Fluid Mechanics*, *780*, 687–716. https://doi.org/10.1017/jfm.2015.479

Quaranta, H. U., Brynjell-Rahkola, M., Leweke, T., & Henningson, D. (2019). Local and global pairing instabilities of two interlaced helical vortices. *Journal of Fluid Mechanics*, *863*, 927–955. https://doi.org/10.1017/jfm.2018.904

Ramos-García, N., Sørensen, J. N., & Shen, W. Z. (2016). Three-dimensional viscous-inviscid coupling method for wind turbine computations. *Wind Energy*, *19*(1), 67–93. https://doi.org/10.1002/we.1821

Ramos-García, N., Abraham, A., Leweke, T., & Sørensen, J. N. (2023). Multi-fidelity vortex simulations of rotor flows: Validation against detailed wake measurements. *Computers & Fluids*, *255*, 105790. https://doi.org/10.1016/j.compfluid.2023.105790

Rezaeiha, A., & Micallef, D. (2021). Wake interactions of two tandem floating offshore wind turbines: CFD analysis using actuator disc model. *Renewable Energy*, *179*, 859–876. https://doi.org/10.1016/j.renene.2021.07.087

Sanderse, B. (2009). Aerodynamics of wind turbine wakes Literature review.

Sarlak, H., Meneveau, C., & Sørensen, J. N. (2015). Role of subgrid-scale modeling in large eddy simulation of wind turbine wake interactions. *Renewable Energy*, *77*, 386–399. https://doi.org/10.1016/j.renene.2014.12.036

Sarlak, H., Nishino, T., Martínez-Tossas, L., Meneveau, C., & Sørensen, J. (2016). Assessment of blockage effects on the wake characteristics and power of wind turbines. *Renewable Energy*, *93*, 340–352. https://doi.org/10.1016/j.renene.2016.01.101

Sarmast, S., Dadfar, R., Mikkelsen, R. F., Schlatter, P., Ivanell, S., Sørensen, J. N., & Henningson, D. S. (2014). Mutual inductance instability of the tip vortices behind a wind turbine. *Journal of Fluid Mechanics*, *755*, 705–731. https://doi.org/10.1017/jfm.2014.326

Schröder, D., Aguilar-Cabello, J., Leweke, T., Hörnschemeyer, R., & Stumpf, E. (2022). Experimental investigation of a rotor blade tip vortex pair. *CEAS Aeronautical Journal*, *13*(1), 97–112. https://doi.org/10.1007/s13272-021-00555-1

Selçuk, S. C. (2016, May). *Numerical study of helical vortices and their instabilities* [Doctoral dissertation, Université Pierre et Marie Curie - Paris VI].

Shen, W. Z., Mikkelsen, R., Sørensen, J. N., & Bak, C. (2005). Tip loss corrections for wind turbine computations. *Wind Energy*, *8*(4), 457–475. https://doi.org/10.1002/we.153

Sherry, M., Nemes, A., Lo Jacono, D., Blackburn, H. M., & Sheridan, J. (2013). The interaction of helical tip and root vortices in a wind turbine wake. *Physics of Fluids*, *25*(11), 117102. https://doi.org/10.1063/1.4824734

Smagorinsky, J. (1963). General Circulation Experiments with the Primitive Equations: I. The basic experiement. *Monthly Weather Review*, *91*(3), 99–164. https://doi.org/10.1175/1520-0493(1963)091<0099:GCEWTP>2.3.CO;2

Sørensen, J. N. (2011a). Instability of helical tip vortices in rotor wakes. *Journal of Fluid Mechanics*, *682*, 1–4. https://doi.org/10.1017/jfm.2011.277

Sørensen, J. N., Shen, W. Z., & Munduate, X. (1998). Analysis of wake states by a full-field actuator disc model. *Wind Energy*, *1*(2), 73–88. https://doi.org/10.1002/(SICI)1099-1824(199812)1:2<73::AID-WE12>3.0.CO;2-L

Sørensen, J., Mikkelsen, R., Henningson, D., Ivanell, S., Sarmast, S., & Andersen, S. (2015). Simulation of wind turbine wakes using the actuator line technique. *Philo-*

sophical transactions. Series A, Mathematical, physical, and engineering sciences, *373*. https://doi.org/10.1098/rsta.2014.0071

Sørensen, J. N., Dag, K. O., & Ramos-García, N. (2016). A refined tip correction based on decambering. *Wind Energy*, *19*(5), 787–802. https://doi.org/10.1002/we.1865

Sørensen, J. N. (2011b). Aerodynamic Aspects of Wind Energy Conversion. *Annual Review of Fluid Mechanics*, *43*(1), 427–448. https://doi.org/10.1146/annurev-fluid-122109-160801

Sørensen, J. N., & Kock, C. W. (1995). A model for unsteady rotor aerodynamics. *Journal of Wind Engineering and Industrial Aerodynamics*, *58*(3), 259–275. https://doi.org/10.1016/0167-6105(95)00027-5

Sørensen, J. N., & Shen, W. Z. (2002). Numerical Modeling of Wind Turbine Wakes. *Journal of Fluids Engineering*, *124*(2), 393–399. https://doi.org/10.1115/1.1471361

Stevens, R. J., & Meneveau, C. (2017). Flow Structure and Turbulence in Wind Farms. *Annual Review of Fluid Mechanics*, *49*(1), 311–339. https://doi.org/10.1146/annurev-fluid-010816-060206

Stovall, T., Pawlas, G., & Moriarty, P. (2010). Wind Farm Wake Simulations in OpenFOAM. In *48th AIAA Aerospace Sciences Meeting Including the New Horizons Forum and Aerospace Exposition*. American Institute of Aeronautics and Astronautics. https://doi.org/10.2514/6.2010-825

Tang, R., & Cao, R. (2023). Numerical investigation on wake characteristics of floating offshore wind turbine under pitch motion. *IET Renewable Power Generation*, *17*(11), 2765–2778. https://doi.org/10.1049/rpg2.12741

Troldborg, N. (2009, January). *Actuator line modeling of wind turbine wakes* [Doctoral dissertation].

Troldborg, N., Larsen, G. C., Madsen, H. A., Hansen, K. S., Sørensen, J. N., & Mikkelsen, R. (2011). Numerical simulations of wake interaction between two wind turbines at various inflow conditions. *Wind Energy*, *14*(7), 859–876. https://doi.org/10.1002/we.433

Van Driest, E. R. (1956). On turbulent flow near a wall. *Journal of the Aeronautical Sciences*, *23*(11), 1007–1011.

Vermeer, L. J., Sørensen, J. N., & Crespo, A. (2003). Wind turbine wake aerodynamics. *Progress in Aerospace Sciences*, *39*(6), 467–510. https://doi.org/10.1016/S0376-0421(03)00078-2

Walther, J. H., Guénot, M., Machefaux, E., Rasmussen, J. T., Chatelain, P., Okulov, V. L., Sørensen, J. N., Bergdorf, M., & Koumoutsakos, P. (2007). A numerical study of the stabilitiy of helical vortices using vortex methods. *Journal of Physics: Conference Series*, *75*(1), 012034. https://doi.org/10.1088/1742-6596/75/1/012034

Westerweel, J., Boersma, B. J. 1., & Nieuwstadt, F. T. M. (T. M., 1946-. (2016). *Turbulence : Introduction to theory and applications of turbulent flows*. Springer. https://doi.org/10.1007/978-3-319-31599-7

Widnall, S. E. (1972). The stability of a helical vortex filament. *Journal of Fluid Mechanics*, *54*(4), 641–663. https://doi.org/10.1017/S0022112072000928

Wilson, R. E. (1986). Wind Turbine Flow Field Model. *Journal of Solar Energy Engineering*, *108*(4), 344–345. https://doi.org/10.1115/1.3268118

Wu, Y.-T., & Porté-Agel, F. (2011). Large-Eddy Simulation of Wind-Turbine Wakes: Evaluation of Turbine Parametrisations. *Boundary-Layer Meteorology*, *138*(3), 345–366. https://doi.org/10.1007/s10546-010-9569-x

Xie, S., & Archer, C. (2015). Self-similarity and turbulence characteristics of wind turbine wakes via large-eddy simulation. *Wind Energy*, *18*(10), 1815–1838. https://doi.org/10.1002/we.1792

Xu, S., Zhuang, T., Zhao, W., & Wan, D. (2023). Numerical investigation of aerodynamic responses and wake characteristics of a floating offshore wind turbine under atmospheric boundary layer inflows. *Ocean Engineering*, *279*, 114527. https://doi.org/10.1016/j.oceaneng.2023.114527

Xue, F., Duan, H., Xu, C., Han, X., Shangguan, Y., Li, T., & Fen, Z. (2022). Research on the Power Capture and Wake Characteristics of a Wind Turbine Based on a Modified Actuator Line Model. *Energies*, *15*(1), 282. https://doi.org/10.3390/en15010282

Zhang, Y., Deng, S., & Wang, X. (2019). RANS and DDES simulations of a horizontal-axis wind turbine under stalled flow condition using OpenFOAM. *Energy*, *167*, 1155–1163. https://doi.org/10.1016/j.energy.2018.11.014

Zhang, Y., van Zuijlen, A., & van Bussel, G. (2015). Massively separated turbulent flow simulation around non-rotating MEXICO blade by means of RANS and DDES approaches in OpenFOAM. In *33rd AIAA Applied Aerodynamics Conference*. American Institute of Aeronautics and Astronautics. https://doi.org/10.2514/6.2015-2716